

Syracuse University

SURFACE

Physics - Dissertations

College of Arts and Sciences

6-2012

Development of Spect and Ct Tomographic Image Reconstruction

Levon Orion Vogelsang
Syracuse University

Follow this and additional works at: https://surface.syr.edu/phy_etd



Part of the [Physics Commons](#)

Recommended Citation

Vogelsang, Levon Orion, "Development of Spect and Ct Tomographic Image Reconstruction" (2012).
Physics - Dissertations. 124.
https://surface.syr.edu/phy_etd/124

This Dissertation is brought to you for free and open access by the College of Arts and Sciences at SURFACE. It has been accepted for inclusion in Physics - Dissertations by an authorized administrator of SURFACE. For more information, please contact surface@syr.edu.

Abstract

The purpose of this study was to contribute to the advancement of statistically-based iterative reconstruction algorithms and protocols for both SPECT and micro CT data. Major contributions of this work to SPECT reconstruction include formulation and implementation of fully three-dimensional voxel-based system matrix in parallel-beam, fan-beam, and cone-beam collimator geometries while modeling the process of attenuation, system resolution and sensitivity. This is achieved by casting rays through a volume of voxels and using ray-voxel intersection lengths to determine approximate volume contributions. Qualitative and quantitative analysis of reconstructed Monte Carlo data sets show that this is a very effective and efficient method. Using this method, three SPECT studies were conducted.

First, the reconstruction performance was studied for a triple-head cone-beam SPECT system using a helical orbit acquisition. We looked at various subset groupings for the ordered-subsets expectation maximization (OSEM) algorithm. We also examined how rotational and translational sampling affects reconstructed image quality when constrained by total injected dose and scan time. We conclude the following: When reconstructing noiseless datasets, varying the rotational sampling from 90 views to 360 views over 360 degrees does not affect the reconstructed activity regardless of the object size in terms of both convergence and accuracy. When using ordered subsets, the subset group arrangement is important in terms of both image quality and accuracy. The smaller the object is that is being reconstructed, the rate of convergence decreases, the spatial resolution decreases, and accuracy decreases.

Second, we examined a system composed of three, possibly different, converging collimators using a circular orbit. We conclude the following: When reconstructing noiseless datasets, using a triple-cone beam system resulted in distortion artifacts along the axial direction

and diminished resolution along the transaxial direction. Using a triple-fan beam system resulted in the best reconstructed image quality in terms of bias, noise, and contrast. When noisy datasets were reconstructed, a cone-cone-fan beam system resulted in best reconstructed image quality in terms of mean-to-actual ratio for small lesions and a triple-fan beam system for large lesions.

Finally, a two-dimensional mesh-based system matrix for parallel-beam collimation with attenuation and resolution modeling was designed, implemented, and studied. We conclude that no more than two divisions per detector bin width are needed for satisfactory reconstruction.

Also, using more than two divisions per detector bin does not significantly improve reconstructed images. A chapter on iterative micro-CT reconstruction is also included. Our contribution to micro-CT reconstruction is the formulation and implementation of a cone-beam system matrix that reduces ring artifacts associated with sampling of the reconstruction space. This new approach reduces the common 3-D ray-tracing technique into 2-D, making it very efficient. The images obtained using our approach are compared to images reconstructed by means of analytical techniques. We observe significant improvement in image quality for the images reconstructed using our iterative method.

**DEVELOPMENT OF SPECT AND CT TOMOGRAPHIC IMAGE
RECONSTRUCTION**

By

Levon Vogelsang

B.Sc. Syracuse University, 2005

DISSERTATION

Submitted in partial fulfillment of the requirements for the degree of Doctor of Philosophy in
Physics in the Graduate School of Syracuse University

June 2012

Copyright 2012 Levon Vogelsang

All Rights Reserved

Acknowledgements

I would like to extend my sincere gratitude to my research advisors, Professor Andrzej Krol and Professor Ed Lipson. Professor Krol has worked with me on a daily basis over the years and his experience, knowledge and creativity has greatly contributed to this dissertation. I would also like to thank Professor Ed Lipson for his detailed reviews and intelligent suggestions.

I would like to thank the members of the defense committee for lending their valuable time and energy. Committee members include; Professor Tomasz Skwarnicki, Professor Jim Fawcett, Professor Pramond Varshney, and Professor Liviu Movileanu.

Thank you to my friends and colleagues who have inspired thoughtful discussions throughout the years: Dr. Hongwei Ye for his outstanding work on, and introduction to, SPECT reconstruction; Dr. Russell Kinkaid for his knowledge regarding micro CT and Image J plugins; Dr. Yao Lu for his mathematical insight regarding mesh-based reconstruction; Dr. Xiaofei Hu for her contributions towards mesh-based attenuation compensation; Dr. Alphonso Magri for his image processing knowledge and Image J plugins; Sreevatsa Lakshmanan for his assistance with programming; and Susan Hemingway for micro CT data acquisition.

Most importantly, I would like to express my love and appreciation to my wife, Dr. Kimberly Vogelsang, who has always supported me. I thank you for your optimism, beautiful heart, and pure soul. And to our daughter, Kaylee, who is such a source of joy and wonder in our lives, we love you.

Table of Contents

Chapter 1. Introduction.....	1
1.1 Single Photon Emission Computed Tomography (SPECT).....	1
1.1.1 Imaging System.....	4
1.1.2 Object Representation	7
1.1.3 Imaging Equation and Statistical Model	8
1.1.4 System Physical Modeling.....	10
1.1.5 Attenuation.....	11
1.1.6 System Resolution and Sensitivity.....	14
1.2 SPECT Image Reconstruction	15
1.2.1 Analytical Reconstruction Methods	16
1.2.2 Iterative Reconstruction Methods	17
1.2.3 OSEM-MAP	19
1.2.4 Cost Functions and regularization.....	20
1.3 SIMIND SPECT Data Monte Carlo Simulation.....	21
1.4 Image Quality Assessment	21
1.5 Aim and Structure of Dissertation	24
Chapter 2. System Matrix in Voxel Domain.....	25
2.1 Introduction	25
2.2 Definitions and Framework.....	26
2.2.1 Normalized Sensitivity Patterns versus Number of Rays	28
2.3 Parallel-Beam Collimator.....	29
2.3.1 Parallel-Beam Collimator Geometry.....	29
2.3.2 Parallel-Beam NSP Results.....	30
2.4 Fan Beam Collimator.....	33
2.4.1 Fan-Beam Collimator Geometry.....	33
2.4.2 Fan-Beam NSP Results	34
2.5 Cone Beam Collimator	37
2.5.1 Cone-Beam Collimator Geometry	37
2.5.2 Cone-Beam NSP Results	38
2.6 Conclusions	42

Chapter 3. Cone-Beam Collimator with Helical Orbit.....	43
3.1 Objective.....	43
3.2 Introduction	43
3.3 Methods	44
3.4 Results	47
3.5 Conclusions	54
Chapter 4. Converging Collimators with Circular Orbit.....	55
4.1 Objective.....	55
4.2 Introduction	55
4.3 Methods	55
4.4 Results	57
4.5 Conclusions	61
Chapter 5. System Matrix in Mesh Domain	62
5.1 Objective.....	62
5.2 Introduction	62
5.3 Methods	63
5.3.1 Mesh.....	63
5.3.2 System Matrix	64
5.3.3 Projection Set	67
5.3.4 Reconstructions.....	67
5.3.5 Evaluation	68
5.4 Results	68
5.5 Conclusions	72
Chapter 6. Volumetric Micro-CT Iterative Reconstruction	74
6.1 Objective.....	74
6.2 Introduction	74
6.3 Methods	75
6.3.1 Micro-CT Scanner.....	75
6.3.2 Transmission Imaging Equation	76
6.3.3 Reconstruction Method	78
6.3.4 Slab Formulism of System Matrix	79
6.4 Results	82
6.5 Conclusions	84

Appendix.....	86
A.1 Detector and Collimator Parameters.....	86
A.2 Resolution and Sensitivity Parameters for Simulated Parallel-Beam.....	87
A.3 Resolution and Sensitivity Parameters for Simulated Fan-Beam SPECT.....	88
A.4 Resolution and Sensitivity Parameters for Simulated Cone-Beam	89
Bibliography.....	91

List of Tables

Table 3.1. MAR within reconstructed cylindrical rods for noisy datasets at iteration 20 when angular views ranged from 90 to 360.	52
Table 3.2. Standard deviation within reconstructed cylindrical rods for noisy datasets at iteration 20 when angular views ranged from 90 to 360.	52
Table 3.3. Uniformity within reconstructed cylindrical rods for noisy datasets at iteration 20 when angular views ranged from 90 to 360.	52
Table 4.1. MAR, SD, and uniformity for a 4cm diameter ROI within a uniform region of water. Reconstructions are of the cylinder phantom that was imaged over 120 views using various combinations of converging collimators. Datasets were noiseless.	59
Table A.1. Parameters of detectors and collimators used in the Division of Nuclear Medicine at SUNY Upstate Medical University.	86
Table A.2. Parameters of the simulated gamma ray detection systems used for this study.	86
Table A.3. Parameters when line-profiles through the parallel-beam collimator projected point-sources shown in fig. 8.1 are fit to an amplitude-Gaussian function Eq. (1.15).	87
Table A.4. Coefficients for the Gaussian spread w (Eq. (1.17)) of the resolution function for parallel-beam collimator.	87
Table A.5. Coefficients for the amplitude A (Eq. (1.16)) of the resolution function for parallel-beam collimator.	88
Table A.6. Parameters when line-profiles through the fan-beam collimator projected point-sources shown in fig. 8.2 are fit to an amplitude-Gaussian function Eq. (1.15).	88
Table A.7. Coefficients for the Gaussian spread functions along the horizontal w_u and vertical w_v (Eq. (1.17)) of the resolution function for fan-beam collimator.	89

Table A.8. Coefficients for the amplitude A (Eq. (1.16)) of the resolution function for fan-beam collimator.	89
Table A.9. Parameters when line-profiles through the cone-beam collimator projected point-sources shown in fig. 8.3 are fit to an amplitude-Gaussian function Eq. (1.15).	90
Table A.10. Coefficients for the Gaussian spread w (Eq. (1.17)) of the resolution function for cone-beam collimator.	90
Table A.11. Coefficients for the amplitude A (Eq. (1.16)) of the resolution function for cone-beam collimator.	90

List of Figures

Figure 1.1. TRIAD XLT triple-head gamma camera (Trionix Research Laboratory, Inc., Twinsburg, OH) in use at SUNY Upstate Medical University (courtesy of SUNY Upstate Medical University)..... 4

Figure 1.2. A basic SPECT gamma camera (Anger camera) system..... 7

Figure 1.3. Mass attenuation coefficient as a function of photon energy for photoelectric absorption τ_m , incoherent scatter σ_m , and coherent scatter ν_m and their sum μ_m [7] for (a) water and (b) bone..... 12

Figure 2.1. Approximate volumes-of-intersection for parallel-beam collimator. This example shows four rays per detector bin. Only the transaxial plane is displayed for clarity. 27

Figure 2.2. Approximate volume contributions for parallel-beam geometry. The voxel is not displayed. 30

Figure 2.3. Sensitivity patterns versus number of rays per bin for a parallel-beam collimator. Rays per bin: (a) 1, (b) 2, (c) 3, (d) 5, (e) 7, (f) 10, (g) 15, and (h) 22..... 31

Figure 2.4. Statistics of NSP for parallel-beam versus number of rays per detector bin. The mean NSP was very close to 1 and independent of the number of rays per bin. Shown are (a) maximum and (b) minimum of the NSP across reconstruction space and (c) standard deviation of NSP..... 32

Figure 2.5. Approximate volume contributions for fan-beam geometry. The voxel is not displayed. 34

Figure 2.6. Sensitivity patterns versus number of rays per bin for fan-beam collimator when detector size equals 2 times reconstruction size. Rays per bin: (a) 1, (b) 2, (c) 3, (d) 5, (e) 7, (f) 10, (g) 15, and (h) 22.35

Figure 2.7. Statistics of NSP for fan-beam versus number of rays per detector bin. The mean NSP was very close to 1 and independent of the number of rays per bin. Shown are (a) maximum and (b) minimum of the NSP across reconstruction space and (c) standard deviation of NSP. 36

Figure 2.8. Approximate volume contributions for cone-beam geometry. The voxel is not displayed. ... 38

Figure 2.9. Statistics for cone-beam normalized sensitivity patterns NSP within the central slice versus number of rays per detector bin. Shown are (a) maximum and (b) minimum of the NSP across the reconstruction space and (c) standard deviation of NSP..... 39

Figure 2.10. Statistics for cone-beam normalized sensitivity patterns NSP within a slice between the central slice and the slice furthest from the central versus number of rays per detector bin. Shown are (a) maximum and (b) minimum of the NSP across the reconstruction space and (c) standard deviation of NSP..... 40

Figure 2.11. Statistics for cone-beam normalized sensitivity patterns NSP within the slice furthest from the central slice versus number of rays per detector bin. Shown are (a) maximum and (b) minimum of the NSP across the reconstruction space and (c) standard deviation of NSP..... 41

Figure 3.1. Digital phantom used for cone-beam collimator with helical orbit SPECT study. Five cylindrical rods are shown embedded in a large cylinder. The ratio of activity between the small cylinder and background is 3:1. 45

Figure 3.2. Illustration of helical cone-beam noisy datasets created using SIMIND. Shown are line profiles through the noisy datasets superimposed over line profiles through the noiseless dataset. Underneath each plot is a sample of the corresponding dataset. Datasets were created using various numbers of views per projection: (a) 90, (b) 120, (c) 180, and (d) 360. Notice that as the number of views per projection increases, the noise per projection increases as well as the rotational and translational sampling..... 46

Figure 3.3. MAR vs. iteration within various sized cylinders using two OS grouping methods. Cylinder diameters are; (a) 0.44 cm, (b) 0.88 cm, (c) 1.32 cm, (d) 1.76 cm, (e) 2.20 cm, and (f) is the background (Figure 3.2 continued) which the smaller cylinders are imbedded. Datasets were noiseless. Each graph displays two curves. The curve using blue squares is an ordered-subset which consists of projections in which the focal points for the three detector heads are located within the same plane along the transaxial direction (in-plane OS) and the red triangles represent a group where the focal points are out of plane (staggered OS). 48

Figure 3.4. (a) Line profile within center slice across hot cylinder along the transaxial direction. (b) Line profile through the uniform background along the axial direction. Staggered subset is represented by squares and in-plane subsets by triangles. Datasets were noiseless..... 49

Figure 3.5. The top row shows slices through the uniform region reconstructed using (a) In-plane subset grouping and (b) staggered subset grouping. The bottom row shows slices through the five hot cylinders reconstructed using (c) In-plane subset grouping and (d) staggered subset grouping. The images in (a) and (c) contain fewer reconstruction artifacts than (b) and (d)..... 50

Figure 3.6. MAR vs. iteration within various sized cylinders. Cylinder diameters are; (a) 0.44 cm, (b) 0.88 cm, (c) 1.32 cm, and (d) 1.76 cm. Datasets contained Poisson noise. Each graph displays four curves corresponding to reconstructions of projections containing 90, 120, 180, and 360 views with total scan time and administered dose fixed..... 53

Figure 4.1. Digital phantoms that were used for converging collimator with circular orbit SPECT study. Five cylindrical rods embedded in a large cylinder. The ratio of activity between the small cylinder and background is 3:1..... 57

Figure 4.2. Reconstructed images of cylinder phantom using various combinations of converging collimators. Top row corresponds to noiseless datasets, and bottom to noisy datasets. (a) and (e) CCC. (b) and (f) CCF. (c) and (g) CFF. (d) and (h) FFF..... 58

Figure 4.3. Line-profile through a 4 cm diameter ROI along the axial direction. Reconstructions are of the cylinder phantom that was imaged over 120 views using various combinations of converging collimators. Datasets were noiseless. (a) Line-profile across a uniform region of the main cylinder. (b) Resolution between main cylinder and air..... 59

Figure 4.4. MAR within small cylinders versus cylinder volume. Reconstructions are of the cylinder phantom that was imaged over 120 views using various combinations of converging collimators. Datasets contained Poisson noise. (a) CCC, (b) CCF, (c) CFF, and (d) FFF. 60

Figure 5.1. (a) NCAT activity map. (b) NCAT attenuation map. (c) Mesh consisting of 7060 nodes and 14,086 triangles. For clarity only center region of mesh is shown (80×80 pixels out of 128×128 pixels).	64
Figure 5.2. Intersection of mesh element and detector bin using 4 divisions per bin.	66
Figure 5.3. Data sets and reconstructed images. First row corresponds to low noise dataset and second row to high noise dataset. (a) Sinograms with varying levels of noise of the NCAT chest phantom generated using SIMIND SPECT simulation software. (b) Mesh-based reconstruction using 1 division per bin. (c) Mesh-based reconstruction using 2 divisions per bin. (d) Mesh-based reconstruction using 3 divisions per bin. (e) Mesh-based reconstruction using 10 divisions per bin. (f) Voxel-based reconstruction using 10 divisions per bin.	68
Figure 5.4. Analysis of reconstructed data sets. First, row corresponds to low noise dataset and second row to high noise data sets. Normalized mean square error (NMSE) vs. iteration within the entire chest phantom for high noise dataset (a) and low noise dataset (c). NMSE vs. iteration within the heart for high noise dataset (b) and low noise dataset (c).	70
Figure 5.5. Analysis of reconstructed data sets. First, row corresponds to low noise dataset and second row to high noise data sets. Signal-to-noise ratio (SNR) vs. iteration within the right lung for low noise dataset (a) and high noise dataset (c). SNR vs. iteration within the heart for low noise dataset (b) and high noise dataset (c).	71
Figure 5.6. Line profiles through the reconstructed (a) heart and (b) left lung at iteration 20.	72
Figure 6.1. (a) MicroCAT II scanner (Siemens) in use at SUNY Upstate Medical University (courtesy of SUNY Upstate Medical University). (b) Detector and object coordinate systems.	76
Figure 6.2. Geometry of cone-beam CT. (a) Slab with a grid size δ that is equal to the de-magnified detector bin grid size P at a distance d from the detector face to the center of the slab. (b) View of a voxel-slab-intersection along the transaxial direction. The intersection points between the center of the slab and the voxel grid are shown.	81

Figure 6.3. Detector plane view of the voxel-slab-intersection. The shaded region shows the area-of-intersection between a slab-bin and a voxel..... 82

Figure 6.4. Reconstructions of micro CT data set consisting of projections of the head of a rat. (a) reconstruction using commercial FBP-based software, Cobra (Exxim Computing Corporation), without any post smoothing applied. (b) Iterative reconstruction using slab formulism. 83

Figure 6.5. Coronal view of the paws. (a) Reconstructed using FBP. (b) Iterative reconstruction using slab formulism. (c) Close-up of (a). (d) and (e) Close-ups of (b). (d) Result after applying a post 3×3 neighborhood averaging filter to (b). 84

Figure A.1. SIMIND simulation of point sources imaged with parallel-beam collimator. Distance of point source from collimator face; (a) 4.4 cm, (b) 8.8 cm, (c) 13.2 cm, (d) 17.6 cm, (e) 22.0 cm, and (f) 26.4 cm..... 87

Figure A.2. SIMIND simulation of point sources imaged with fan-beam collimator. Distance of point source from collimator face; (a) 4.4 cm, (b) 8.8 cm, (c) 13.2 cm, (d) 17.6 cm, (e) 22.0 cm, and (f) 26.4 cm. 88

Figure A.3. SIMIND simulation of point sources imaged with cone-beam collimator. Distance of point source from collimator face; (a) 4.4 cm, (b) 8.8 cm, (c) 13.2 cm, (d) 17.6 cm, (e) 22.0 cm, and (f) 26.4 cm. 89

List of Acronyms

2-D	<i>two dimensional</i>
3-D	<i>three dimensional</i>
CBC	<i>cone-beam collimator</i>
CT	<i>computed tomography</i>
DRF	<i>detector response function</i>
FBC	<i>fan-beam collimator</i>
FBP	<i>filtered back-projection</i>
FWHM	<i>full width at half maximum</i>
LEHR	<i>low energy high resolution</i>
LEUR	<i>low energy ultra-high resolution</i>
MAP-EM	<i>maximum a posteriori expectation maximization</i>
MAR	<i>mean-to-actual ratio</i>
MLEM	<i>maximum likelihood expectation maximization</i>
NMSE	<i>normalized mean square error</i>
NSP	<i>normalized sensitivity pattern</i>
PBC	<i>parallel-beam collimator</i>
PET	<i>positron emission tomography</i>
PMMA	<i>polymethyl methacrylate</i>
PMT	<i>photomultiplier tube</i>
PS-PMT	<i>position sensitive photomultiplier tube</i>
ROI	<i>region of interest</i>

ROR	<i>radius of rotation</i>
SD	<i>standard deviation</i>
SNR	<i>signal-to-noise ratio</i>
SPECT	<i>single photon emission computed tomography</i>
TCT	<i>transmission computed tomography</i>
TEW	<i>triple energy window</i>
TOR	<i>tube of response</i>
TV	<i>total variation regularization</i>
VOI	<i>volume of interest</i>

Chapter 1. Introduction

Tomography is a non-invasive imaging technique allowing for the visualization of the internal structure of an object. The early deterministic framework for tomographic imaging was formulated by the Austrian mathematician, Johann Radon in 1917 [1]. The method is used in many fields such as radiology, archeology, biology, geophysics, oceanography, materials science, astrophysics, and many other sciences [2]. We focus on its application to radiology, in particular to *Single Photon Emission Computed Tomography* (SPECT) and *Computed Tomography* (CT).

1.1 Single Photon Emission Computed Tomography (SPECT)

Emission Tomography (ET) uses radioactive tracers to image various aspects of physiology and is categorized as a functional imaging modality as opposed to CT, which if used without imaging contrast agents yields anatomical information. SPECT and *Positron Emission Tomography* (PET) are the two main techniques within this branch of medical imaging. Both PET and SPECT are fundamentally based on the tracer principle [2]. This principle was introduced in the early 1900's by George de Hevesy (Noble Prize in Chemistry in 1943) and is based on the fact that radioactive compounds are indistinguishable from nonradioactive in terms of their participation in physiological processes. The emission of gamma rays from radioactive materials can be detected, thus allowing a means to track the flow and distribution of targeted substances in the body. Due to radiation safety concerns, the amount of radiopharmaceutical that can be administered to the patient is limited. Gamma-ray emission rates are relatively low and are typically $\sim 10^4$ emissions $\text{s}^{-1} \text{ml}^{-1}$ of tissue. Data acquisition usually takes 15-20 minutes.

Application of radioactive materials as markers, or tracers, is the foundation of modern day SPECT. *Radiopharmaceuticals* or *radiotracers* are imaging agents that can be engineered for a variety of substances that naturally participate in biological functions.

Every SPECT study requires radiopharmaceutical specifically designed for imaging a particular disease. The image quality increases with the amount of the radiotracer delivered to the patient. After the radiopharmaceutical has been administered, the data acquisition process begins. This entails the collection and counting of the photons emitted from the patient's body at all acquisition angles. A typical triple-head SPECT imaging system is shown in Fig. 1.1. Only photons within a predefined energy window corresponding to a specific isotope photopeak are recorded. The collected photon counts data are stored in discrete detector bins (each with known spatial location) and are organized into projections. Once the projection data have been collected, through tomographic image reconstruction, the distribution of the activity within the patient can be estimated. The final step is the reconstructed image analysis that consists of visual inspection complemented by computerized analysis.

The most common uses of SPECT in clinical practice include regional cerebral blood flow brain studies, bone scan, and myocardial perfusion imaging. The following is a general summary of each of these.

For brain imaging, SPECT can look directly at cerebral blood flow and indirectly at metabolic activity [2]. Two of the most common radiopharmaceuticals used in brain perfusion are ^{99m}Tc -HMPAO (hexamethylpropylene amine oxime) and ^{99m}Tc -ECD (ethylcysteinate dimer). These agents can cross the blood-brain barrier and distribute in the brain in proportion to blood flow. Typical reasons that warrant a SPECT brain study include cerebrovascular disease, dementia, or seizure. The possibility of disease would be indicated by hypoperfusion in

conjunction with information that led to the request of the study. The process begins with injection of approximately 1100 MBq of the radiopharmaceutical that is transported by the blood stream and is utilized by receptor sites within the brain. Imaging begins 1 hour after injection; the gamma detector slowly rotates around the patient's head and acquires projection images called "views" in a step-and-shoot fashion. Typically, 120 to 128 total views (3° per step) are acquired within a total acquisition time of 20 minutes. These projections are then reconstructed into 3-D images of the brain activity distribution resulting in a map of regional cerebral blood flow. It is through these reconstructions that physicians are able to identify certain brain activity patterns that correlate with psychiatric and neurological disease.

The typical agents used for a bone SPECT are ^{99m}Tc -MDP (methylene diphosphonate) or a similar compound [2]. The bone SPECT study is done in conjunction with and immediately follows a planar whole-body bone study. The goal is to better locate and assess possible abnormalities that were detected in the planar study. Probable disease is indicated by foci of increased uptake that are either above or below normal. Typical dose ranges from 740-1110 MBq. The imaging commences 2-5 hours after injection. Like brain SPECT, 120 total views (3° per step) are acquired within a total acquisition time of 20 minutes.

The most common of all SPECT studies is myocardial perfusion rest/stress SPECT where a dual-isotope is used to examine the heart at rest and under stress [2]. Interpretation involves comparison of the reconstructed rest and stress images of the heart. Typical agents are ^{201}Tl -TlCl and ^{99m}Tc -sestambi. In dual-isotope protocol with the patient at rest, the study begins with injection of 148 MBq of ^{201}Tl -TlCl IV. After a 15-minute delay, imaging begins. The detector consists of a dual-head system with the heads separated by 90° . The total number of views is 60 or 64 over 180° . Total acquisition time during the rest test is approximately 15 minutes.

Following the completion of the rest test, the patient is put under stress. After approximately 10 minutes, injection of 925 MBq of ^{99m}Tc -sestamibi or tetrofosmin is administered. Imaging commences 30 minutes after injection. The total number of views is 60 or 64 over 180° . Total acquisition time during the rest test is approximately 11 minutes.



Figure 1.1. TRIAD XLT triple-head gamma camera (Trionix Research Laboratory, Inc., Twinsburg, OH) in use at SUNY Upstate Medical University (courtesy of SUNY Upstate Medical University).

1.1.1 Imaging System

During a SPECT scan, the detector moves along an orbit around a patient and acquires data via either a continuous or a stop-and-shoot technique. The mechanical axis of rotation must be fixed in space during the scan. The radius of rotation (ROR) can be fixed or variable. As a result, a series of planar images called projections is created. This projection set is reconstructed into the expected 3-D distribution of radiotracer or activity inside the patient.

The function of the gamma camera system is to capture the gamma or x-ray radiation that has been emitted from the patient and convert it into useful information that can be reconstructed into the activity distribution. The basic operation of this system is as follows: First, the gamma and/or x-ray radiation emitted from the patient is mechanically directed by means of an aperture or a collimator towards a scintillation crystal. This is achieved by absorbing radiation that is propagating in directions other than that specified by the collimator. There are tradeoffs between collimator resolution and sensitivity that depend on its geometry. From the selected photons that reach the scintillation crystal, only a very small fraction ($\sim 10^{-4}$) interacts with it and converts its energy into scintillations and consequently into electronic pulses. A basic SPECT gamma camera (Anger camera) system is shown in Fig. 1.2 and is composed of the following components [2]:

- *Collimator*: Gamma rays, unlike optical radiation, cannot be refracted and focused by conventional optical systems. Therefore, data sets generated by a SPECT system are formed by selective absorption. This is achieved by placing a collimator between the patient and the detector [2]. The collimator is a plate composed of lead or tungsten with a periodic lattice of holes conforming to a predefined geometry (parallel, converging, diverging, pinhole, etc.). This is necessary for gamma-ray and x-ray image formation. Gamma- or x-rays that interact with the collimator holes' walls, called septa, are mostly absorbed. Therefore, only the photons that are traveling sufficiently close to the direction parallel to the collimator hole axis contribute to the data sets (images). This is a very inefficient process. For a typical collimator, about one in ten thousand photons emitted from the patient reaches the detector. The collimator characteristics are the main

contributing factors for determining the system resolution and system sensitivity.

Selected data on collimators used in the Division of Nuclear Medicine at SUNY Upstate Medical University are collected in Table A.1. The parameters that were used for simulated data for this dissertation are listed in Table A.2. The following are the components of a SPECT imaging system.

- *Scintillation crystal* (NaI(Tl)): The scintillation crystal converts high energy gamma-rays and x-rays into visible light photons (38,000 photons/MeV).
- *Position sensitive photomultiplier tubes* (PS-PMT's): Position sensitive photomultiplier tubes consists of phototransducers that convert visible light pulses into a measurable current and provides information on the detected amount of current and its location.
- *Preamplifier*: The preamplifier converts current to voltage and matches the impedance of the PS-PMT and amplifier.
- *Amplifier*: Amplifies the voltage from preamplifier.
- *Pulse-height analyzer*: The pulse-height analyzer rejects pulses outside the allowed range (i.e. below the set lower limit and above the set upper limit).
- *Position logic unit*: The position logic unit computes the two-dimensional location of the scintillation events.
- *Recording device*: The location and number of scintillation events with energy within a preset energy window are recorded during the scan for each acquisition angle. The resulting noisy histograms represent the projections.
- *Data reconstruction and analysis system*: The raw projections are transformed into an estimate of the activity distribution by means of a reconstruction process. The image analysis system involves strategies for the extraction of qualitative and quantitative

information from the reconstructed images for the evaluation and decision-making process by physicians.

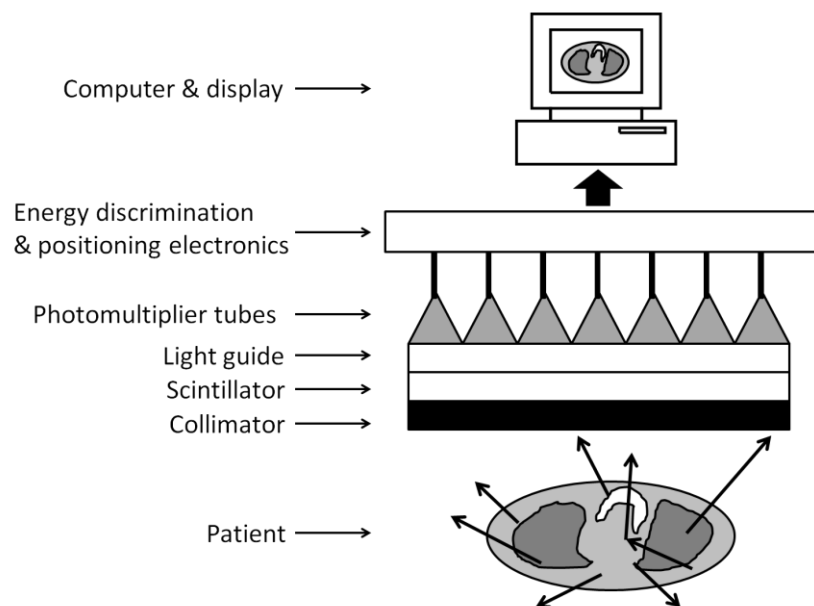


Figure 1.2. A basic SPECT gamma camera (Anger camera) system.

1.1.2 Object Representation

When using iterative algorithms for reconstruction, it is necessary to represent the activity distribution function $f(\mathbf{r})$, where \mathbf{r} is a position in 3-D space, in terms of some finite set of basis functions $b_n(\mathbf{r})$ [3]. An N element column vector can then represent the weights associated with these functions

$$\mathbf{f} = [f_1, f_2, \dots, f_n, \dots, f_N] \quad (1.1)$$

with the n^{th} element denoted as f_n . If we choose piecewise constant rect-functions as the basis functions, then f_n is the expected average number of gamma-ray photons per unit volume emitted per second within voxel element n . Rect-functions are the most widely used due to their

attractive symmetry properties and ease of computation. Chapters 2, 3 and 4 use this representation. If we choose piecewise linear mesh elements, then f_n is the expected average number of gamma-ray photons per unit volume emitted per second at node n . Chapter 5 explores this representation. In general, the expansion of $f(\mathbf{r})$ has the form

$$f(\mathbf{r}) \approx \sum_n^N f_n b_n(\mathbf{r}) \quad (1.2)$$

where

$$f_n \equiv f(\mathbf{r}_n). \quad (1.3)$$

Besides the two representations noted above, other basis functions have been studied. Some popular linear basis function choices include [4,5] Fourier series, wavelets, spherical harmonics, point masses, polar grids, and organ-based functions, and Kaiser-Bessel functions (blobs). Nonlinear basis functions include [4] spheres, ellipsoids, deformable templates, and polygons.

1.1.3 Imaging Equation and Statistical Model

We assume that the continuous distribution of radiopharmaceuticals $f(\mathbf{r})$ within the patient is square-integrable and supported within the region $\mathbf{\Omega}_f$ in three-dimensional space. The SPECT data vector \mathbf{g} , which is formed from the discrete projections revealed by the imaging system, is a finite set of M finite values with the m^{th} component denoted g_m . The index m specifies a particular detector element and projection angle combination.

When stochastic components are ignored, the deterministic transformation from the continuous distribution of radiotracer inside the patient's body to the discrete projections recorded by the detector can be given by the following linear integral equation:

$$\bar{g}_m = \int_{\Omega_f} h_m(\mathbf{r}) f(\mathbf{r}) d^3 r . \quad (1.4)$$

The function $h_m(\mathbf{r})$ is the point response function that relates the response of the m^{th} detector pixel to radiation originating from location \mathbf{r} within the reconstruction space. The physics, geometry and other components of the imaging system (e.g. electronics) can be described by the point response function.

The true projections g_m follows a Poisson statistical model where Eq. (1.4) describes the mean [4]. The assumptions that allow us to use such a model are as follows:

- The binomial distribution closely approaches the Poisson distribution.
- The spatial locations of individual radionuclei at any moment are independent random variables, which are all identically distributed according to a common probability function.
- The number of administered radionuclei has a Poisson distribution over any given volume of the object.
- The radionuclide decay process is a Poisson process [6].
- Each emitted gamma photon can only be recorded by at most one detector bin, and the location of where the photon is measured in the detector is independent of all other photons [6].
- Background radiation and crosstalk are independently distributed [6].

Under these assumptions, we can represent the Poisson model of the counted photons as:

$$g_m = \text{Poisson } \bar{g}_m + r_m , \quad (1.5)$$

where r_m is a vector that represents the noise such as background and cosmic radiation, which is not modeled by the imaging equation. For many practical purposes this noise vector can be set to zero.

1.1.4 System Physical Modeling

Using the parameterized object representation, the continuous-to-discrete transformation given in eq. (1.4) now becomes a discrete-to-discrete transformation and has the form

$$\bar{g}_m = \sum_n^N f_n \int_{\Omega_f} h_m(\mathbf{r}) b_n(\mathbf{r}) d^3r . \quad (1.6)$$

We can now define the discrete projection operation

$$\bar{g}_m = \sum_n^N a_{mn} f_n \quad (1.7)$$

with the system matrix, also called the projection operator, defined as

$$a_{mn} \equiv \int_{\Omega_f} h_m(\mathbf{r}) b_n(\mathbf{r}) d^3r . \quad (1.8)$$

An element of the system matrix a_{mn} is proportional to the probability that a radioactive decay event located within the volume defined by the n^{th} voxel is recorded by the m^{th} detector unit. The system matrix can describe all physical phenomena. Scan geometry, attenuation, detector response, detector efficiency, object scatter, and collimator scatter are some of the main contributors. Improvements in modeling the physical system through the system matrix can greatly improve reconstructed image quality. Other factors to consider when formulating the system matrix are computation time and storage requirements. The main focus of this dissertation is improvement of the system matrix represented in both the voxel and mesh domains in terms of physical modeling and computational efficiency.

1.1.5 Attenuation

Consider a monochromatic beam of photons in good geometry transported through a homogeneous slab of material. If $n(x)$ photons remain at a depth x within the material, then dn photons are removed or diverted from the beam after traveling a small distance dx [6]. This can be described by the differential equation

$$\frac{dn}{dx} = -\mu n(x). \quad (1.9)$$

Each photon is influenced neither by neighboring photons nor by its own history. The interaction between the photons and material in this manner follows a Poisson process. The factor μ in Eq. (1.9) is the *linear attenuation coefficient* of the material. It is a function of the material's density ρ and effective atomic number Z as well as the energy E of the photon beam, and so we denote it as $\mu(\rho, Z, E)$. The dependence of μ on ρ has been shown to be proportional within a reasonable range and can be written as

$$\mu(\rho, Z, E) = \left[\frac{\mu(Z, E)}{\rho} \right] \rho \quad (1.10)$$

where the term $\mu_m = [\mu(Z, E)/\rho]$ is called the mass attenuation coefficient.

The emitted gamma- and x-ray photons interact with matter on their way to the detector. This process of attenuation alters the photon flux and diminishes spatial resolution [6]. The interaction between photons and matter for the energy range of interest in nuclear medicine [20-600 keV] are mainly described by photoelectric absorption cross-section (τ), incoherent or Compton scattering cross-section (σ) and coherent scattering cross-section (ν). The partitioning of μ into the different types of interactions mentioned above can be formally expressed as [6]

$$\mu = \tau + \sigma + \nu, \quad (1.11)$$

and like μ , all cross-sections are linear in the density. As Figure 1.3 indicates, for the energy range used in SPECT [20- 400 keV], incoherent scattering dominates the photon-matter interactions in water. For such an energy range, tissue has radiological properties very similar to water.

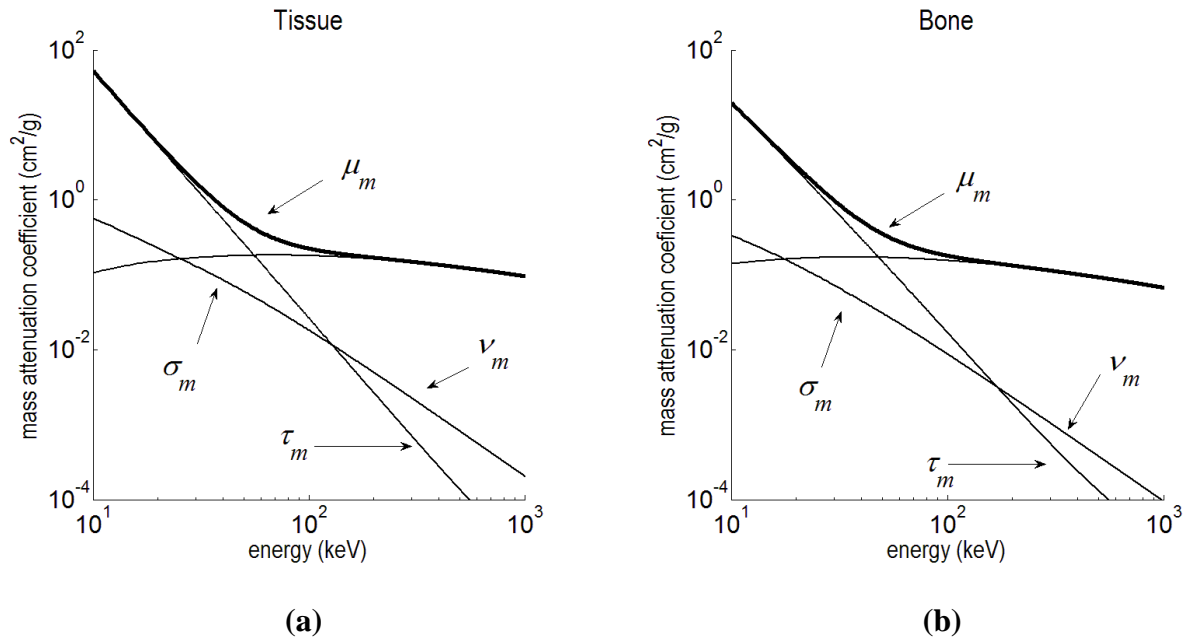


Figure 1.3. Mass attenuation coefficient as a function of photon energy for photoelectric absorption τ_m , incoherent scatter σ_m , and coherent scatter ν_m and their sum μ_m [7] for (a) water and (b) bone.

The dependence of μ on Z and E varies accordingly to the type of interaction being considered. Photoelectric absorption is the process where nearly all of the photon energy is transferred to the atomic electron. A small fraction of the energy goes into overcoming the electron's attachment to its nucleus and thereby freeing the electron. The rest is converted into kinetic energy of the free electron. For nearly all materials of radiological interest, experiments show that τ_m increases approximately with the third power of the effective atomic number. It is

also observed that τ_m decreases with the third power of photon energy. Putting these together yields

$$\tau_m(Z, E) \sim \frac{Z^3}{E^3}. \quad (1.12)$$

Incoherent scattering is the process where some of the photon's energy is given to the recoil electron with the rest of the energy creating the Compton scatter photon. At lower energies, the attenuation process is generally dominated by photoelectric absorption and at higher energies by incoherent scattering. Also, σ_m only slightly varies across the energy range being considered and can be approximated as constant for practical purposes. For a more detailed description as to how σ varies with energy, the well-known Klein-Nishina formula should be used [6]. The manner in which σ_m varies with Z can be explained as follows: The photon energy is relatively much higher than the binding energies of the electrons. Therefore, the electrons can be considered a gas of free independent particles. The probability for an interaction would depend on the electron density. Bring this all together, the manner in which the electron density is influenced by the effective atomic number determines how σ_m depends on Z . The electron density per Z stays fairly constant for most materials except hydrogen where the electron density is twice that of other materials. This can be summarized as [6]

$$\sigma_m(Z, E) \sim \begin{cases} 0.02cm^2/g & \text{(most materials, falls off at higher } Z) \\ 0.04cm^2/g & \text{(hydrogen)} \end{cases}. \quad (1.13)$$

Coherent scattering is the process in which almost no energy is lost in the photon-electron interaction. The photons are, however, collectively deflected into a new direction. It has been shown that the mass attenuation coefficient for coherent scatter increases slowly with the effective atomic number and falls off inversely with the square of the photon energy,

$$v_m(Z, E) \sim \frac{Z}{E^2}. \quad (1.14)$$

1.1.6 System Resolution and Sensitivity

Collimator efficiency or sensitivity can be defined as the fraction of γ rays passing through the collimator per γ ray emitted by the source [2]. System resolution can be defined as the full width at half-maximum (FWHM) of the count profile of a point source of radiation projected by the collimator onto the detector [8]. Both depend on the location of the source relative to the detector.

The system resolution R_s of the gamma camera is influenced by several factors, including intrinsic resolution R_i , collimator resolution R_c , scattered radiation, and septal penetration. However, R_c and R_i dominate. Intrinsic resolution is due to the uncertainty in position estimation in the gamma camera and decreases with increasing energy and detector crystal thickness [8,9]. The intrinsic resolution for a typical gamma camera is in the range of 2.9 to 4.5 mm FWHM for ^{99m}Tc [8]. The collimator performance is the primary limiting factor for the system resolution. It is a function of the collimator geometry and the source location [2,6,8].

The sensitivity is affected by several factors including geometric efficiency, intrinsic efficiency, energy binning, and attenuation [8]. The photopeak detection efficiency of a gamma camera is close to 100% for photon energies up to 100 keV and increases with increasing NaI(Tl) crystal thickness [6]. The sensitivity is of the order of 10^{-4} for a typical parallel-beam SPECT system.

In order to obtain accurate reconstructed images, the system resolution and sensitivity must be modeled and incorporated into the reconstruction algorithm. One way is to experimentally measure the *detector response function* (DRF) for a point source placed at various locations relative to the collimator [10]. Examples of this for simulated data are shown in

the Appendix. The DRF is then created by fitting the data to a function such as a Gaussian. The Gaussian's parameters then define the dependence of resolution and sensitivity on source location. This method is used throughout this dissertation. Using the amplitude version of the Gaussian peak function as a model, the DRF is

$$R(u, v; d) = A(u, v; d) e^{-\frac{1}{2} \left(\frac{u^2}{w_u^2(d)} + \frac{v^2}{w_v^2(d)} \right)}, \quad (1.15)$$

where the resolution is defined by the Gaussian spread w and the sensitivity is defined by the amplitude A . The detector variables u and v refer, respectively, to horizontal and vertical locations on the count image created by the detector. The object space variable d refers to the shortest distance from the point source to the collimator face. We used 3rd degree polynomials to model the amplitude and spread as a function of source-to-collimator distance

$$A(d) = a_0 + a_1 d + a_2 d^2 + a_3 d^3, \quad (1.16)$$

$$w(d) = b_0 + b_1 d + b_2 d^2 + b_3 d^3. \quad (1.17)$$

The coefficients, a_i and b_i ($i = 0, 1, 2, 3$), were obtained by curve fitting and are listed in the Appendix: Tables A.4 and A.5 for parallel-beam, Tables A.7 and A.8 for fan-beam, and Tables A.10 and A.11 for cone-beam collimation.

Besides the method of experimental fitting for determining the DRF, another method is to use an analytical formulation [11,12,13]. This method is especially useful when the DRF cannot be explicitly measured, such as the design or simulation of a new collimator [12].

1.2 SPECT Image Reconstruction

As mentioned above, a gamma camera system acquires two-dimensional projections from a finite set of angles g . Projection counts are Poisson distributed. The projections themselves

have little if any value to the physician. What one wishes to obtain from these is the three-dimensional distribution of radiopharmaceutical $f(\mathbf{r})$ that was administered to the patient. The estimation of $f(\mathbf{r})$ from g , or *tomographic reconstruction*, is achieved by solving the integral equation, Eq. (1.4). This is an ill-posed inverse problem and there are many reconstruction methods available for obtaining the solution for emission tomography. The two major classes of tomographic reconstruction are analytical and iterative [4].

1.2.1 Analytical Reconstruction Methods

Analytical methods typically neglect data noise and complicating physical factors. This is done in order to attempt to achieve direct inversion formulas. Most approaches to SPECT image reconstruction are based on Filtered Back Projection (FBP) methods, which belong to the class of analytical methods. They are attractive due to their excellent computational speed. This technique is based on a simplified model of the SPECT data acquisition process that neglects many significant features [2].

FBP usually handles the data noise by pre-smoothing the projection prior to reconstruction or by post smoothing the reconstructed image. The necessity of using a ramp filter to prevent the star artifact in FBP reconstruction results in amplification of high frequency noise component and needs to be remedied by an apodizing filter with the cutoff frequency matching the noise structure.

1.2.2 Iterative Reconstruction Methods

Iterative reconstruction methods approach the inverse problem by solving a system of simultaneous linear equations. They allow for easy modeling of pertinent physical phenomena (e.g. attenuation or detector resolution) in the reconstruction process. They could be classified as algebraic approaches (ART, MART, SMART) and statistical approaches that include weighted least squares (CG, CD, ISRA), maximum likelihood (OSEM-MAP, SAGE, CG) [4]. In general, the statistical methods tend to generate superior reconstructions in terms of image quality as compared to analytical methods [4]. The main disadvantage of these methods relative to analytical methods is their relatively large computational burden. However, as processing speeds of modern computers continue to increase and algorithms continue to be developed, this is becoming less of an issue.

Using the Bayesian framework, the *a posteriori* probability distribution of the unknown activity distribution vector λ is given by Bayes' theorem,

$$P(\lambda|g) = P(g|\lambda) \frac{P(\lambda)}{P(g)}. \quad (1.18)$$

Where $P(\lambda)$ defines any prior knowledge about λ and $P(g)$ defines the prior probability distribution of the measurements g , which are given by measurements [14]. The likelihood function, $P(g|\lambda)$, is the conditional probability of observing a fixed g for a variable vector λ . If we take the natural logarithm of Eq. (1.18), this relation becomes

$$l(\lambda;g) \equiv \ln P(\lambda|g) = \ln P(g|\lambda) + \ln P(\lambda) - \ln P(g). \quad (1.19)$$

Using a Poisson statistical model, the natural logarithm of the likelihood function is

$$\begin{aligned}
\ln P(g|\lambda) &= \ln [P(g_0) P(g_1) \dots P(g_{M-1})] \\
&= \sum_m^M \ln [P(g_m)] \\
&= \sum_m^M \ln \left[\frac{e^{-\bar{g}_m} \bar{g}_m^{g_m}}{g_m!} \right] \\
&= \sum_m^M [-\bar{g}_m + g_m \ln \bar{g}_m - \ln g_m!],
\end{aligned} \tag{1.20}$$

where \bar{g}_m is the projection operator acting on the vector λ

$$\bar{g}_m = \sum_n^N a_{mn} \lambda_n. \tag{1.21}$$

For SPECT reconstruction, a common Bayesian prior $P(\lambda)$ that allows for local smoothness is the Gibbs prior distribution [15]

$$\begin{aligned}
\ln P(\lambda) &= \ln [C e^{-\beta U(\lambda)}] \\
&= -\beta U(\lambda) + \ln C
\end{aligned} \tag{1.22}$$

where $U(\lambda)$ is the energy function and β controls the strength of the prior. The constant C is the normalizing factor. Inserting the above into Eq. (1.19) yields

$$l(\lambda) = \sum_m^M [-\bar{g}_m + g_m \ln \bar{g}_m] - \beta U(\lambda) + K, \tag{1.23}$$

where $K = \ln C - \ln P(g) - \sum \ln g_m!$ is a constant independent of λ . Using Newton's dot

notation to represent the derivatives with respect to λ_n , we have

$$\dot{l}(\lambda) = -\sum_m^M a_{mn} + \sum_m^M \frac{g_m}{\bar{g}_m} a_{mn} - \beta \dot{U}(\lambda). \tag{1.24}$$

Rearranging and multiplying both sides by λ_n leads to

$$\lambda_n = \lambda_n \frac{\sum_m^M \frac{g_m}{\bar{g}_m} a_{mn}}{\sum_m^M a_{mn} + \beta \dot{U}(\lambda_n)}. \tag{1.25}$$

Setting β to zero and using an iterative update scheme with k representing the k^{th} iteration, results in the one-step-late [16] MLEM algorithm laid out by Shepp and Vardi [17] and Lange and Carson [18]:

$$\lambda_n^{k+1} = \lambda_n^k \frac{\sum_m^M \frac{g_m}{\bar{g}_m^k} a_{mn}}{\sum_m^M a_{mn}} \quad (1.26)$$

where $\bar{g}_m^k = \sum_n^N a_{mn} \lambda_n^k$. This is the MLEM algorithm and it contains four primary operations: one projection, two back-projections, and an estimate update. Using these operations arranged in this special manner, the goal is to converge to a general solution of the best estimate of f (mean number of disintegrations per volume) with the hope that as $k \rightarrow \infty$, $\lambda \rightarrow f$.

1.2.3 OSEM-MAP

In order to accelerate the convergence of the MLEM algorithm, Hudson and Larkin [19] proposed a general procedure for processing emission data. With this method, Ordered-Subset Expectation Maximization (OS-EM), the projection data is grouped into ordered subsets where the OS level defines the number of these subsets. As mentioned above, the EM algorithm contains three primary operations, projection, back-projection, and estimate update. The OS-EM algorithm computes a subset of projections and back-projections. An estimate is then created based on these subsets. This estimate is then used to compute the next subset of projections and back-projections. The modified algorithm has the form

$$\lambda_n^{k+1} = \lambda_n^k \frac{\sum_{m \in S_i} \frac{g_m}{\bar{g}_m^k} a_{mn}}{\sum_{m \in S_i} a_{mn}} \quad (1.27)$$

where $S_t = \{S_1, S_2, \dots, S_T\}$ is the t^{th} subset out of a total of T .

The configuration of projection angles within a subset can take many different patterns. It has been shown that convergence speed and reconstructed image quality is optimal when each subset contains equally distributed projections [20].

1.2.4 Cost Functions and regularization

Both the MLEM and OSEM algorithms try to match the estimated projection with the true data. In reality, the measured data are riddled with Poisson noise. As convergence is approached, this noise propagates to the emission distribution estimate. Methods developed to deal with this noise propagation can be divided into two categories. The first is noise reduction techniques [4], which include pre-filtering the noisy dataset, halting the iteration process before convergence [21], filtering the reconstructed estimate during each iteration [22], and post-filtering the final reconstructed estimate [23].

The second category for dealing with noise propagation includes true regularization methods [4]. True regularization methods are known to possess superior attributes such as algorithm stability, fast convergence, and edge preservation. Incorporating regularization into the EM algorithm is achieved by including *a posteriori* information as was shown above and resulted in the following equation [24],

$$\lambda_n^{k+1} = \lambda_n^k \frac{\sum_m^M \frac{g_m}{g_m^k} a_{mn}}{\sum_m^M a_{mn} + \beta \dot{U}(\lambda_n^k)} . \quad (1.28)$$

1.3 SIMIND SPECT Data Monte Carlo Simulation

Simulated SPECT data sets were created using SIMIND simulation software. SIMIND uses Monte Carlo techniques to simulate almost any type of calculation or measurement encountered in SPECT imaging. It was developed by Professor Michael Ljungberg from Lund University, Sweden [25]. The code, written in FORTRAN 90, was implemented on a Windows x86 system. There are two primary programs named CHANGE and SIMIND that are required to set up and execute a simulation. The CHANGE program is used to define the imaging system, object parameters, and outputs. The SIMIND program reads the input files created by CHANGE, executes the Monte Carlo simulation, and outputs results to the screen and to data files. The output projection set is in units of counts (injected dose [MBq])/(scan time per view [s]). Once a projection set is created and scaled by an appropriate injected dose and scan time, Poisson noise can be added. The software also allows for a dataset to be separated into total photons and scattered photons where the user can define the scatter order and energy window.

1.4 Image Quality Assessment

Two factors will need to be considered when comparing the advantages and disadvantages among reconstruction methods. The first is the performance of the reconstruction algorithm. This is usually done by looking at properties such as convergence rate, calculation speed, complexity, simplicity, and memory requirements. In the context of the EM algorithm, convergence is usually measured by the behavior of the log-likelihood function versus iteration. More in-depth proofs of convergence for different EM algorithms have been studied [4,14,17,26] and will not be considered here.

The second measure or performance is the reconstructed image. Ultimately, this is what is diagnostically important. The quality assessment of the reconstructed images can be categorized as an *estimation task* or *detection task* [9,27]. An *estimation task* is defined as the measure of some value such as noise or bias. The goal of a *detection task* is to decide among several possible states of truth. This could be the presence or absence of a lesion. In this dissertation, we use estimation task for evaluating the reconstructed image.

We define an *image artifact* as an artificial image feature that persists for different noise realizations. Therefore, a distinction is made between *random noise* effects and image artifacts.

The image quality measures are as follows:

Mean activity distribution within region l

$$\bar{\lambda}_l = \frac{1}{N} \sum_{j \in R_l} \lambda_j, \quad (1.29)$$

where R_l is the subset of voxels associated with the l^{th} region-of-interest that contains N voxels.

Standard deviation of activity distribution, which is a measure of noise, within region l is defined as

$$\sigma_l = \sqrt{\frac{1}{N-1} \sum_{j \in R_l} \lambda_j - \bar{\lambda}_l^2}. \quad (1.30)$$

The *signal-to-noise ratio* is defined as

$$SNR = \frac{\bar{\lambda}_l}{\sigma_l}. \quad (1.31)$$

Uniformity is defined as

$$uniformity = \frac{f_{\max} - f_{\min}}{f_{\max} + f_{\min}} \quad (1.32)$$

where f_{\max} and f_{\min} are the maximum and minimum values, respectively, within a ROI.

Relative contrast is defined as the difference in mean activity distribution within a region l and the background region b , divided by the mean activity distribution within a region b ,

$$C = \left(\frac{\bar{\lambda}_l - \bar{\lambda}_b}{\bar{\lambda}_b} \right). \quad (1.33)$$

Lesion detectability takes into account both contrast and noise and is defined as the difference in mean activity distribution within a region l and the background region b , divided by the noise of the activity concentration in the background noise σ_b and is defined by the following equation:

$$D = \left(\frac{\bar{\lambda}_l - \bar{\lambda}_b}{\sigma_b} \right). \quad (1.34)$$

Mean to actual ratio (MAR) is ratio between the reconstructed mean activity distribution and the true mean activity distribution f_l reference within region l , and is defined as

$$MAR = \frac{\bar{\lambda}_l}{f_l}. \quad (1.35)$$

An MAR close to unity would mean that the reconstruction is very accurate.

In addition to the image analysis measures mentioned above, we also use the *normalized mean square error* which is defined as [28,29]

$$NMSE = \frac{\sum_{j \in R_l}^N \lambda_j - p_j^2}{\sum_{j \in R_l}^N p_j^2}, \quad (1.36)$$

where p_j is the value of the phantom within the j^{th} pixel.

1.5 Aim and Structure of Dissertation

The focus of this dissertation is the advancement of both emission and transmission tomographic iterative reconstruction, though slanted towards emission tomography. The first five chapters are focused on SPECT tomography, while the last chapter addresses transmission tomography. The dissertation is structured in the following manner. Chapter 1 (this chapter) introduces SPECT imaging and SPECT tomographic reconstruction. Chapter 2 explains the SPECT system matrix for various collimator geometries. Chapter 3 examines cone-beam helical acquisition, while Chapter 4 looks at combinations of converging collimators with circular acquisition. Chapter 5 examines the system matrix for parallel-beam, mesh-domain reconstruction. Chapter 6 is devoted to the development of system matrix for iterative transmission tomographic reconstruction.

Chapter 2. System Matrix in Voxel Domain

2.1 Introduction

A primary goal when using the MLEM algorithm, or any projector-based reconstruction algorithm, is to create a projector that is both physically realistic and computationally efficient. Physically realistic translates into effectively modeling the physics that describes the transformation from the activity distribution within the object to the digital output created by the detection system. This all should be achieved with a relatively basic algorithm that can be computed within a reasonable time frame. In, 1988, Lo [30] proposed a strip-area system model for a parallel-beam collimator. A *triangle subtraction technique* was used to calculate the intersected area between a voxel and detector bin tube-of-response. This method calculates the exact volume-of-intersection. Other analytical volumes-of-intersection methods for parallel-beam and converging collimator geometries have also been proposed [31]. Also, approximate volumes-of-intersection methods [30,32,33,34] have been studied. However, it can become cumbersome when one tries to incorporate the attenuation contribution into these algorithms. A common approach to include attenuation is to use ray-tracing techniques to determine the lengths-of-intersection and match up a given volume contribution with its nearest length-of-intersection [35]. To alleviate this problem, we have coupled the length-of-intersection directly with an associated approximate volume-of-intersection. The volumes-of-intersection are determined along a ray that is projected from a location on the detector face to the collimator's focal point. The length-of-intersection is then used to compute an approximate volume-of-intersection. The geometry of the elements used to create an approximate volume-of-intersection depends on the collimator geometry.

2.2 Definitions and Framework

In this chapter we describe our method for efficient and accurate calculation of a system matrix, defined by Eq. (1.8), that includes the effects of photoelectric attenuation, detector response and sensitivity, and collimator geometry. This is accomplished using preexisting ray-tracing techniques [36,37]. In order to achieve balance between system model accuracy and efficiency, we will make the following approximations: (1) only photon transit paths that lie within a detector bin's tube-of-response (TOR) are included. With this approximation, second order and higher scatter is not modeled directly. This method has been shown to reduce computing time dramatically with a negligible loss of reconstruction accuracy [38]. Also, the loss of resolution due to the collimator is not directly modeled through ray tracing. This operation is applied to the projector and back-projector iteratively. This means that first order scatter (photoelectric attenuation) is not properly modeled for photons that are not traveling exclusively within a TOR. (2) The integration over the detector response function multiplied by the basis functions is discretized. This means that the probability that a photon from the n^{th} voxel to be recorded by the m^{th} detector unit is approximated. Three collimator geometries are studied: parallel-beam, fan-beam, and cone-beam.

We define the r^{th} ray associated with the m^{th} detector bin as the rm^{th} ray. The total approximated volume contribution of the n^{th} voxel to the m^{th} detector bin is the sum sub-volumes-of-intersection and is given by

$$v_{mn} = \sum_r^{RS} v_{rnm}, \quad (2.1)$$

where RS is the total number of rays per detector bin. Figure 2.1 shows an example of volumes-of-intersection for parallel-beam collimator. We define the axial direction as the direction along the axis-of-rotation and transaxial direction as the direction that is perpendicular to the axial.

If the attenuation factor from each sub-volume to the detector face is included, the system matrix element becomes

$$a_{mn} = \sum_r^{RS} v_{rnm} \exp \left\{ -\frac{1}{2} \mu_n l_{rnm} - \sum_{k \neq n}^{S_{rnm}} \mu_k l_{rmk} \right\}, \quad (2.2)$$

where S_{rnm} is the set of voxels between the n^{th} voxel and m^{th} detector bin that the r^{th} ray passes through. The factor μ_n is the average attenuation coefficient within the n^{th} voxel and l_{rnm} is the intersection length of the rm^{th} ray passing through the n^{th} voxel. The determination of an accurate, patient specific, attenuation map is essential to incorporating attenuation compensation (AC) into the reconstruction algorithm [39]. Methods for obtaining accurate attenuation maps for this purpose include registration of an attenuation map from another modality, estimation of the transmission map using a SPECT/CT system, SPECT with radioisotope-based transmission system, and estimation of the attenuation map from solely the emission data [40]. Such anatomical information can be obtained from a transmission computed tomography (TCT) scan or MRI.

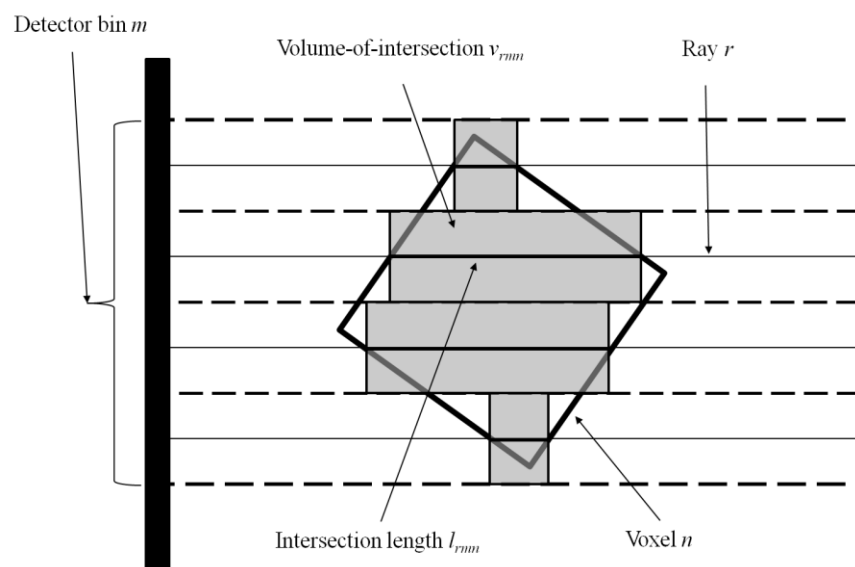


Figure 2.1. Approximate volumes-of-intersection for parallel-beam collimator. This example shows four rays per detector bin. Only the transaxial plane is displayed for clarity.

Regardless of the collimator geometry, the general algorithm for calculating the system matrix is given by the following pseudocode:

- Loop over projection angle θ
- Get coordinates of center of detector and focal point
- Loop over detector bins
- Get bin index
- Loop over rays per bin
- Get coordinates of point where ray intersects detector
- Input coordinates into ray-tracing algorithm
- For each voxel intersected by ray, generate intersection length, volume contribution, and shortest distance to detector face
- Loop over subset of voxels intersected by ray starting from voxel closest to detector
- Multiply volume element and attenuation
- If current voxel has a contribution then sum

2.2.1 Normalized Sensitivity Patterns versus Number of Rays

We use the normalized sensitivity pattern (NSP) for determining the optimal number of rays per detector bin for a given scan geometry and reconstruction resolution. The NSP can be viewed as an image with the same number of elements as the reconstruction grid and is defined as

$$s_n = \frac{1}{\eta\alpha} \sum_m^M v_{mn}, \quad (2.3)$$

where v_{mn} is the approximated intersected volume of the n^{th} voxel and the m^{th} convex polyhedron defined by the focal point at its apex and detector pixel at its base. The constant η is the volume of a voxel and α represent the total number of angular views. Notice that if all errors of any nature could be corrected, s_n would equal 1 for all n that are projected completely for all α . For a 128^3 grid, the average time required to cast a ray through the reconstruction space and calculate the approximate volume-of-intersections was found to be $8.3 \mu\text{s}$ per ray. Examples of NSP's along with the associated statistics for parallel-, fan-, and cone-beam geometries are given within the following sections.

2.3 Parallel-Beam Collimator

A parallel-beam collimator contains channels that are both parallel to one another and at right angles with respect to the collimator face. Parallel-beam collimation offers a good compromise between resolution and sensitivity. The reconstruction is relatively straightforward relative to that for converging collimators. For these reasons, parallel-beam is widely used clinically.

2.3.1 Parallel-Beam Collimator Geometry

The sub-volume-of-intersection used for the parallel-beam system matrix is defined as a rectangular cuboid with two faces parallel to the detector. The volume-of-intersection contribution associated with the rm^{th} ray passing through the n^{th} voxel for parallel-beam collimator is

$$v_{rmn} = \frac{PQ}{RS} l_{rmn} . \quad (2.4)$$

where l_{rmn} is the intersection length between the rm^{th} ray and the n^{th} voxel. The constants P and Q are the horizontal and vertical lengths of a detector bin respectively. The factor R is the number of rays per bin along the horizontal and S is the number of rays per bin along the vertical. The geometry for a parallel-beam volume-of-intersection is displayed in Fig. 2.2. The voxel that is being intersected is not displayed in the figure.

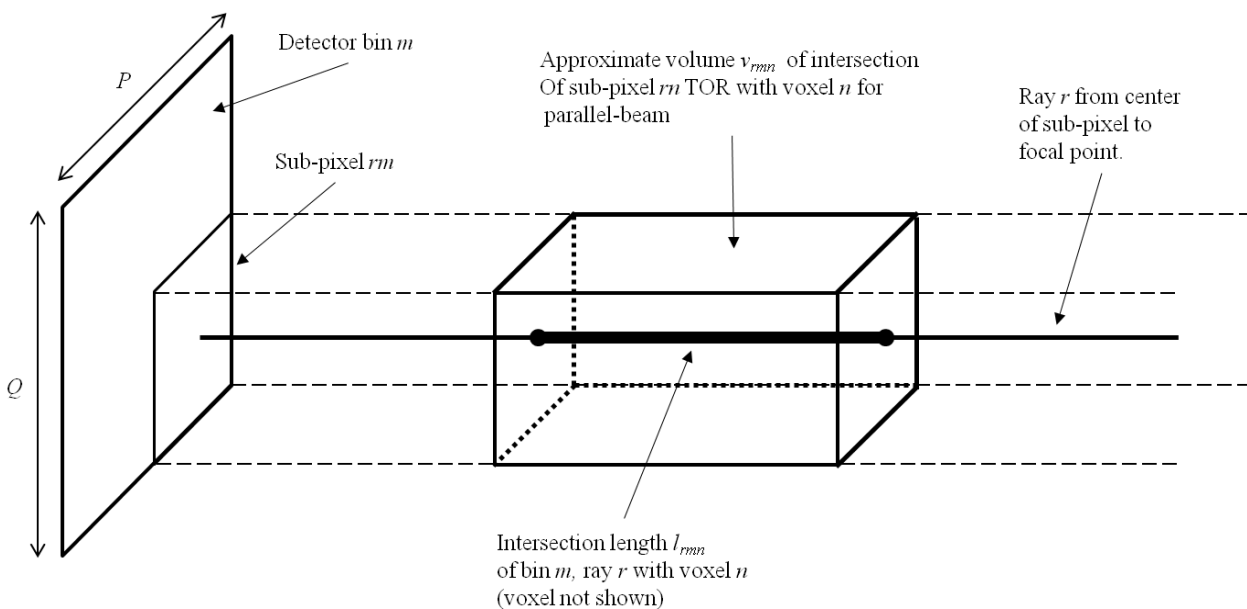


Figure 2.2. Approximate volume contributions for parallel-beam geometry. The voxel is not displayed.

2.3.2 Parallel-Beam NSP Results

The NSP for a parallel-beam collimator are displayed in Fig. 2.3. The rays were distributed uniformly and horizontally across the detector pixel and ranged from 1 to 22 rays per bin. The reconstruction space was 128^3 and the dimension of a detector bin was equal to that of a voxel which was 0.48 cm in this case. The plots shown in Fig. 2.4 show the statistics for the

NSP's depicted in Fig. 2.3. The statistics included the standard deviation of all the pixels within the NSP, and the maximum and minimum of the NSP.

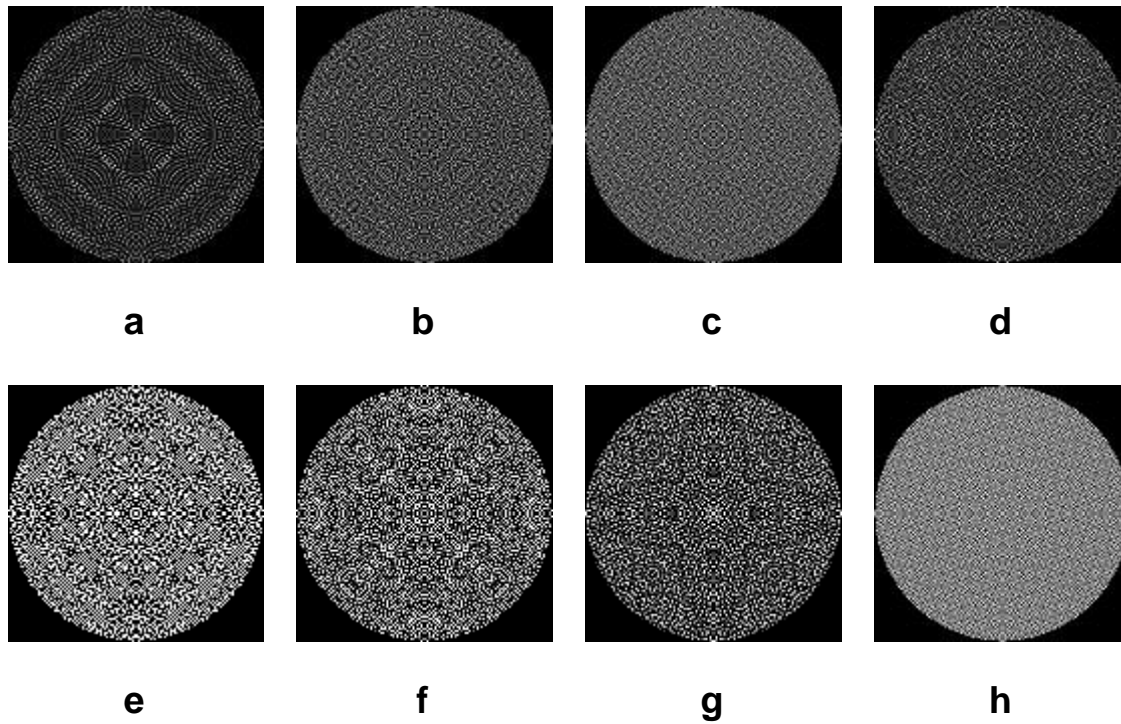


Figure 2.3. Sensitivity patterns versus number of rays per bin for a parallel-beam collimator. Rays per bin: (a) 1, (b) 2, (c) 3, (d) 5, (e) 7, (f) 10, (g) 15, and (h) 22.

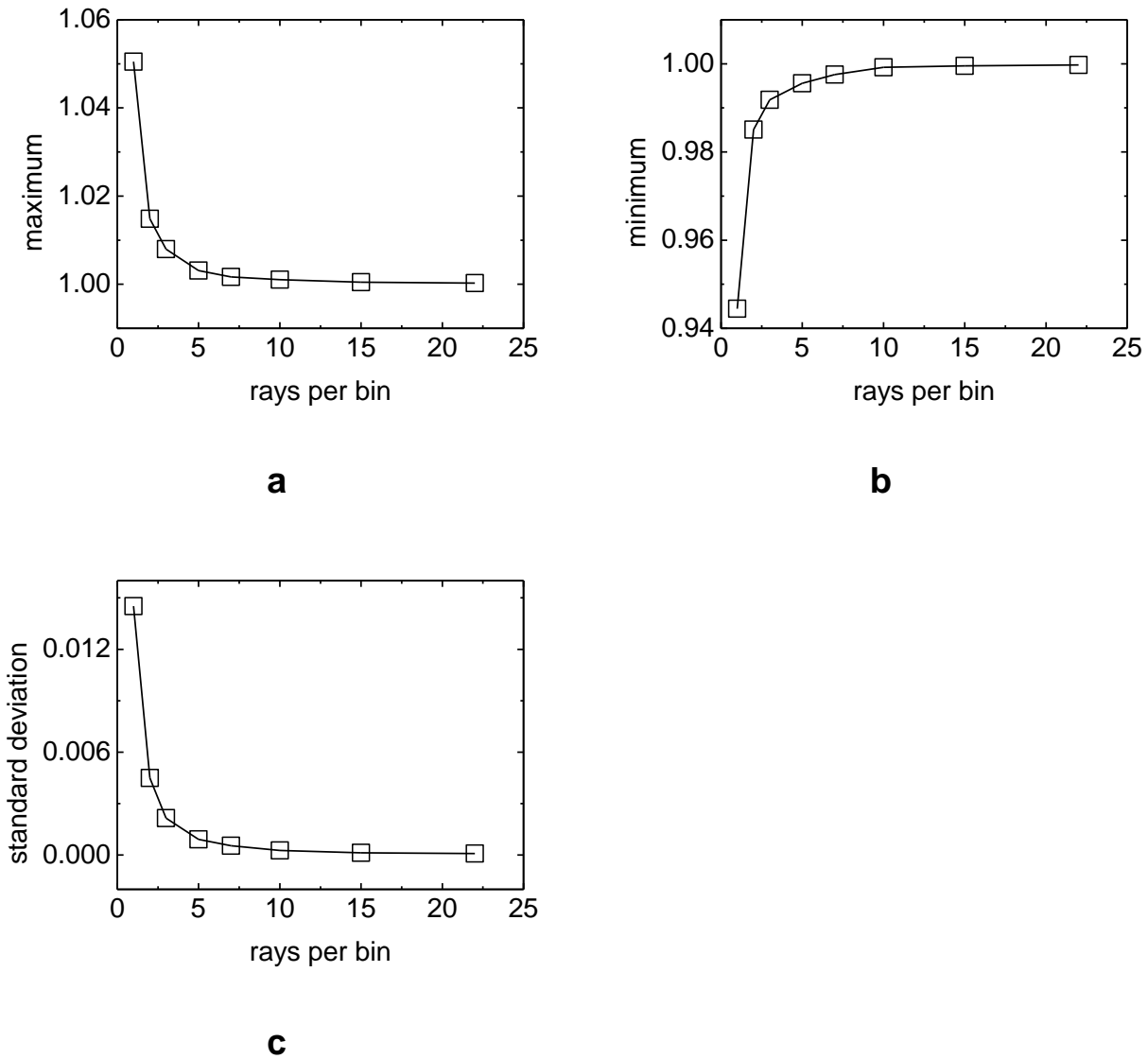


Figure 2.4. Statistics of NSP for parallel-beam versus number of rays per detector bin. The mean NSP was very close to 1 and independent of the number of rays per bin. Shown are (a) maximum and (b) minimum of the NSP across reconstruction space and (c) standard deviation of NSP.

For a parallel-beam collimator with the detector and reconstruction space parameters above, the mean NSP taken across the reconstruction space was very close to 1 when using at least one ray per bin. A standard deviation of the NSP less than 0.1 % was achieved when five or more rays per bin were required. To achieve a ± 0.5 % or less maximum/minimum fluctuation about the mean, five rays per bin were required.

2.4 Fan Beam Collimator

Fan-beam collimation is within the realm of focusing or converging collimators. Fan-beam offers a gain in sensitivity along the transaxial direction compared to parallel- beam. The trade-off with the gain in sensitivity is a loss in the field-of-view (FOV). Therefore, convergent collimators are useful when imaging smaller organs such as the brain or heart.

2.4.1 Fan-Beam Collimator Geometry

The holes in a fan-beam collimator focus along a focal line. The focal length is the distance from the patient side of the collimator to the focal line. This defines the focusing power of the collimator. The sub-volume-of-intersection used for the fan-beam system matrix is determined as follows: A wedge is formed by the sub-pixel on the detector as the base square and the focal line as the apex edge. The two triangles that define the wedge are parallel to one another. A ray is cast from the center of the sub-pixel to the focal line and is parallel to the triangles. The two intersection points of this ray with a voxel are determined as well as the volume of a wedge from each intersection-point to the focal line. The sub-volume-of-intersection is the difference in the volume of the polyhedron from each intersection-point. The volume-of-intersection contribution associated with the rm^{th} ray passing through the n^{th} voxel for a fan-beam collimator is

$$v_{rmn} = \frac{PQ}{RS} F + T \left(\frac{1}{2} \right) \left(\frac{l_{rmn}}{w_{rm}} \right) \left[2 - \frac{{}^1a_{rmn} + {}^2a_{rmn}}{w_{rm}} \right], \quad (2.5)$$

where F is the focal length and T the thickness of the collimator. The factor w_{rm} is the length of the rm^{th} ray that is cast from the focal line to the detector. The factors ${}^1a_{rmn}$ and ${}^2a_{rmn}$ are the

distances along w_{rm} from the detector to the first and second, respectively, intersection points with n^{th} voxel. The geometry for a fan-beam sub-volume-of-intersection is displayed in Fig. 2.5.

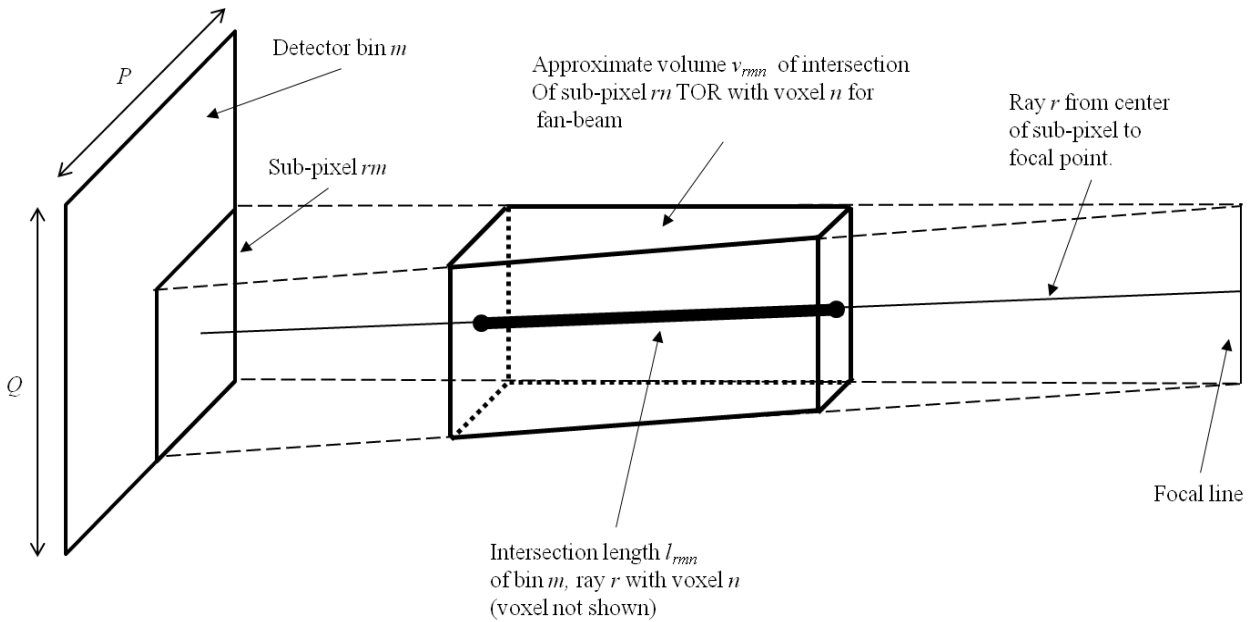


Figure 2.5. Approximate volume contributions for fan-beam geometry. The voxel is not displayed.

2.4.2 Fan-Beam NSP Results

Figure 2.6 displays an example of the sensitivity artifacts versus the number of rays per detector bin associated with fan-beam geometry. The rays were distributed uniformly horizontally across the detector pixel and ranged from 1 to 22 rays per bin. The reconstruction space grid was 128^3 and the reconstruction voxel size was half that of the detector pixel size. The plots shown in Fig. 2.7 show the statistics for the NSP's depicted in Fig. 2.6. The statistics included the standard deviation of all the pixels within the NSP, and the maximum and minimum of the NSP.

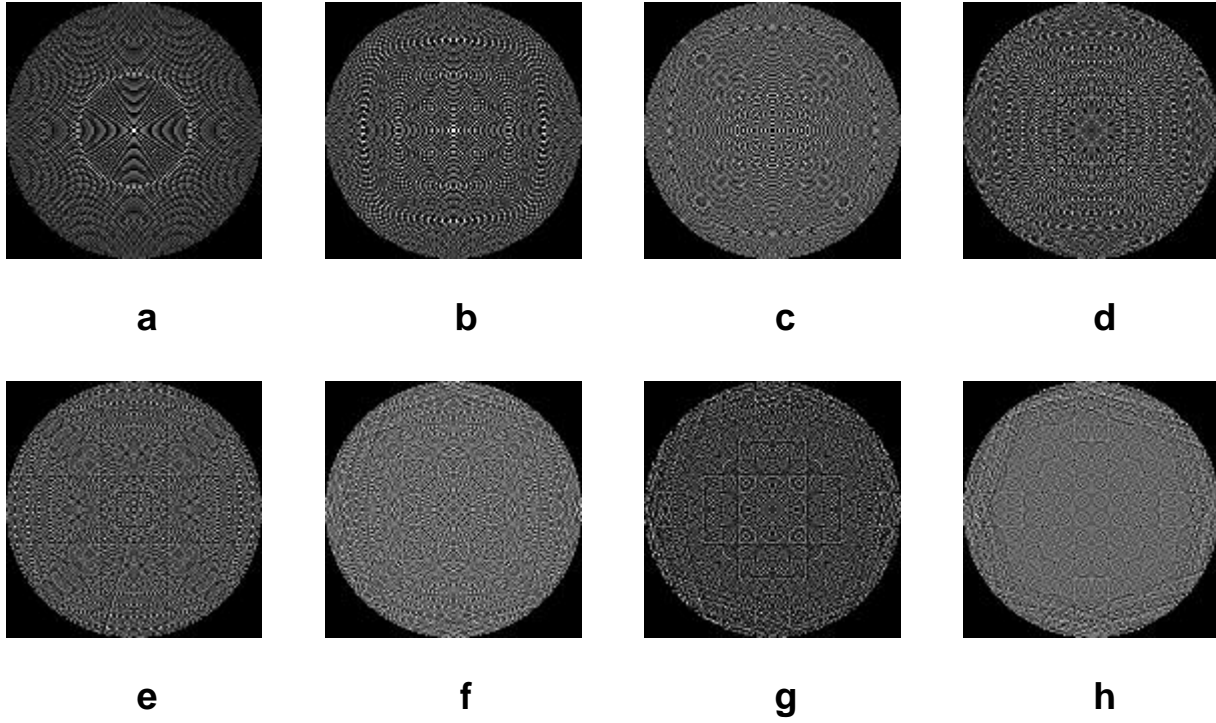


Figure 2.6. Sensitivity patterns versus number of rays per bin for fan-beam collimator when detector size equals 2 times reconstruction size. Rays per bin: (a) 1, (b) 2, (c) 3, (d) 5, (e) 7, (f) 10, (g) 15, and (h) 22.

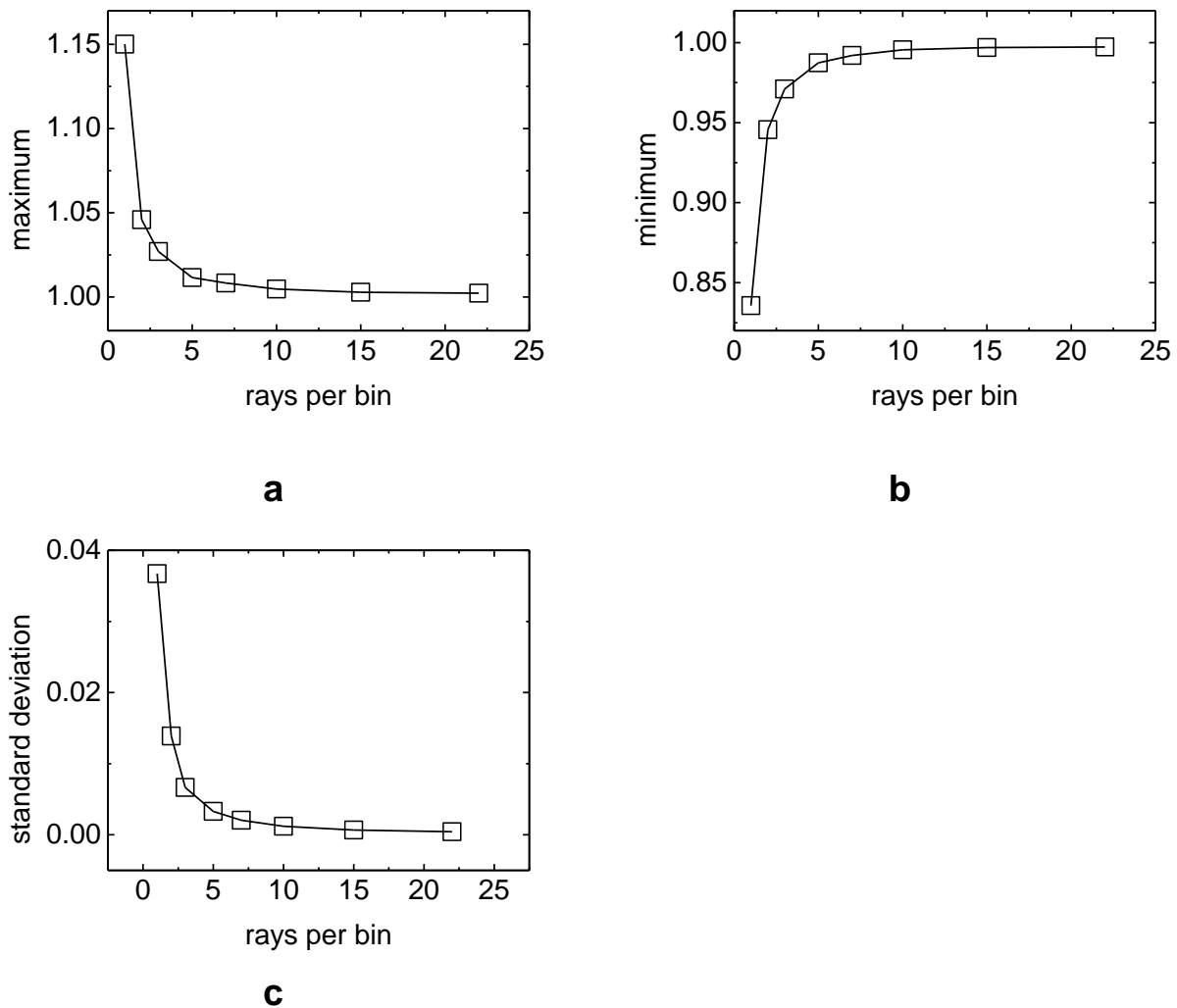


Figure 2.7. Statistics of NSP for fan-beam versus number of rays per detector bin. The mean NSP was very close to 1 and independent of the number of rays per bin. Shown are (a) maximum and (b) minimum of the NSP across reconstruction space and (c) standard deviation of NSP.

For a fan-beam collimator with the detector and reconstruction space parameters above, the mean NSP taken across the reconstruction space was very close to 1 when using at least one ray per bin. A standard deviation of the NSP less than 1 % was achieved when five or more rays per bin were required. To achieve a $\pm 2\%$ or less maximum/minimum fluctuation about the mean, five rays per bin were required.

2.5 Cone Beam Collimator

When compared to conventional collimator geometries, cone-beam collimation increases the number of detected photons [41]. This increased count density leads to improved overall diagnostic accuracy without loss in resolution. Like fan-beam, with this gain in sensitivity comes a loss in the FOV size. This improved sensitivity, or efficiency, is within both the transaxial and axial directions, whereas for fan-beam it is only along the transaxial. Li et. al. [42] demonstrated, through continuous receiver operating characteristic (CROC) curves, that cold lesions in the posterior portion of the thalamus are best detected using cone-beam collimation, compared to fan-beam and parallel-beam. However, the cone-beam collimator has not yet been put into use clinically. Major drawbacks are the artifacts caused by problems with sampling [43]. Researchers have tried various methods to fix this problem such as combined imaging with parallel-beam collimator, helical detector orbit, etc. We explore application of helical orbits in Chapter 3 and combinations of converging collimators in Chapter 4. Also, since the cone-beam reconstruction problem is truly 3-D, one should expect higher complexity, longer reconstruction times, and slower convergence.

2.5.1 Cone-Beam Collimator Geometry

The sub-volumes-of-intersection used for the cone-beam system matrix are determined as follows. A polyhedron is formed by the square detector sub-pixel as the base and the focal point as the apex. A ray is cast from the center of the sub-pixel to the focal point. The two intersection points of this ray with a voxel are determined. The volume of the polyhedron from each intersection-point to the focal point is determined. The sub-volume-of-intersection is the difference in the volume of the polyhedron from each intersection-point. The volume-of-

intersection contribution associated with the rm^{th} ray passing through the n^{th} voxel for a cone-beam collimator is

$$v_{rmn} = \frac{PQ}{RS} F + T \left(\frac{1}{3} \right) \left[\left(1 - \frac{{}^1a_{rmn}}{w_m} \right)^3 - \left(1 - \frac{{}^2a_{rmn}}{w_m} \right)^3 \right] \quad (2.6)$$

where all symbols are defined above. The geometry for a cone-beam sub-volume-of-intersection is displayed in Fig. 2.8.

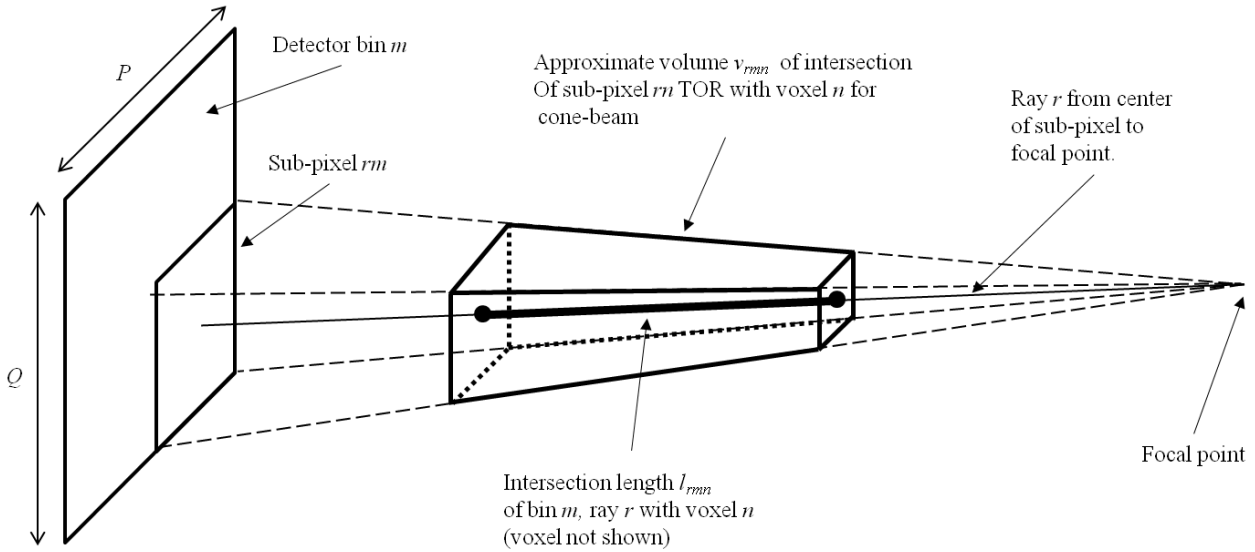


Figure 2.8. Approximate volume contributions for cone-beam geometry. The voxel is not displayed.

2.5.2 Cone-Beam NSP Results

The plots in Figs. 2.9, 2.10, and 2.11 show the statistics for the NSP's versus the number of rays per detector bin for cone-beam geometry. The rays were distributed uniformly throughout the detector pixel. The statistics included the standard deviation of all the pixels within the NSP, and the maximum and minimum of the NSP. The reconstruction space grid was 128^3 and the

reconstruction voxel size was half that of the detector pixel size. Five slices were chosen ranging from the furthest from center slice to the center slice.

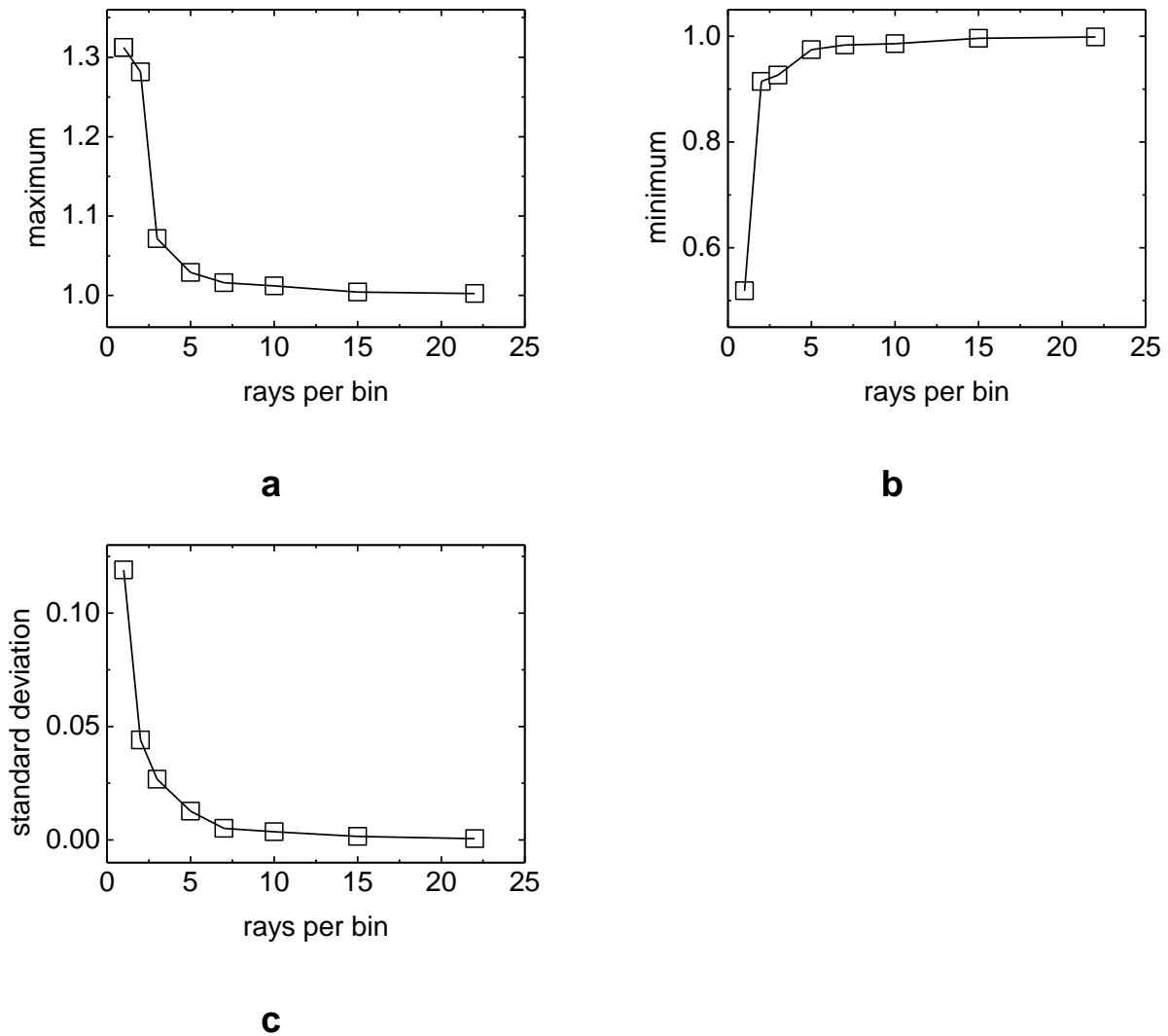


Figure 2.9. Statistics for cone-beam normalized sensitivity patterns NSP within the central slice versus number of rays per detector bin. Shown are (a) maximum and (b) minimum of the NSP across the reconstruction space and (c) standard deviation of NSP.

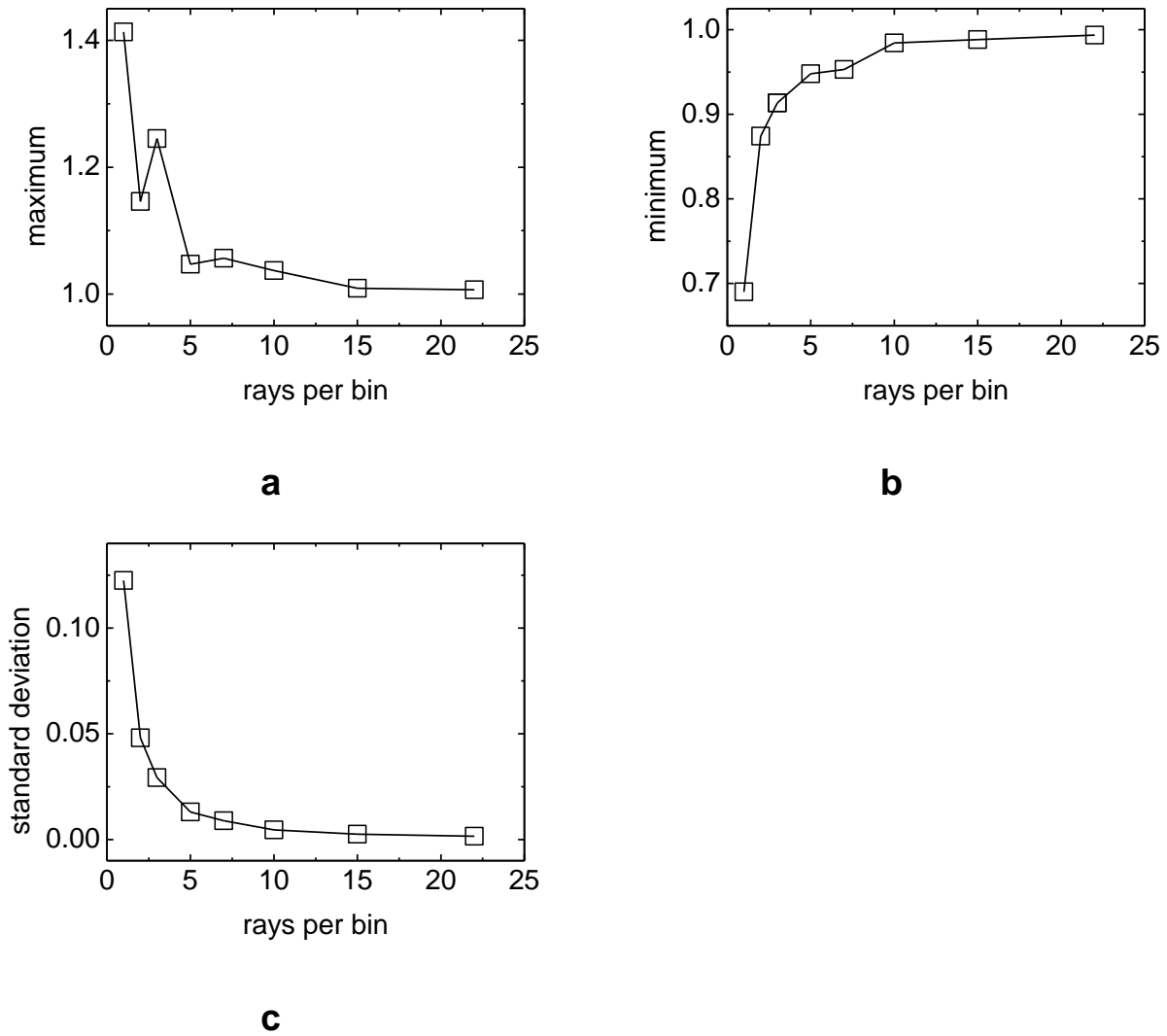


Figure 2.10. Statistics for cone-beam normalized sensitivity patterns NSP within a slice between the central slice and the slice furthest from the central versus number of rays per detector bin. Shown are (a) maximum and (b) minimum of the NSP across the reconstruction space and (c) standard deviation of NSP.

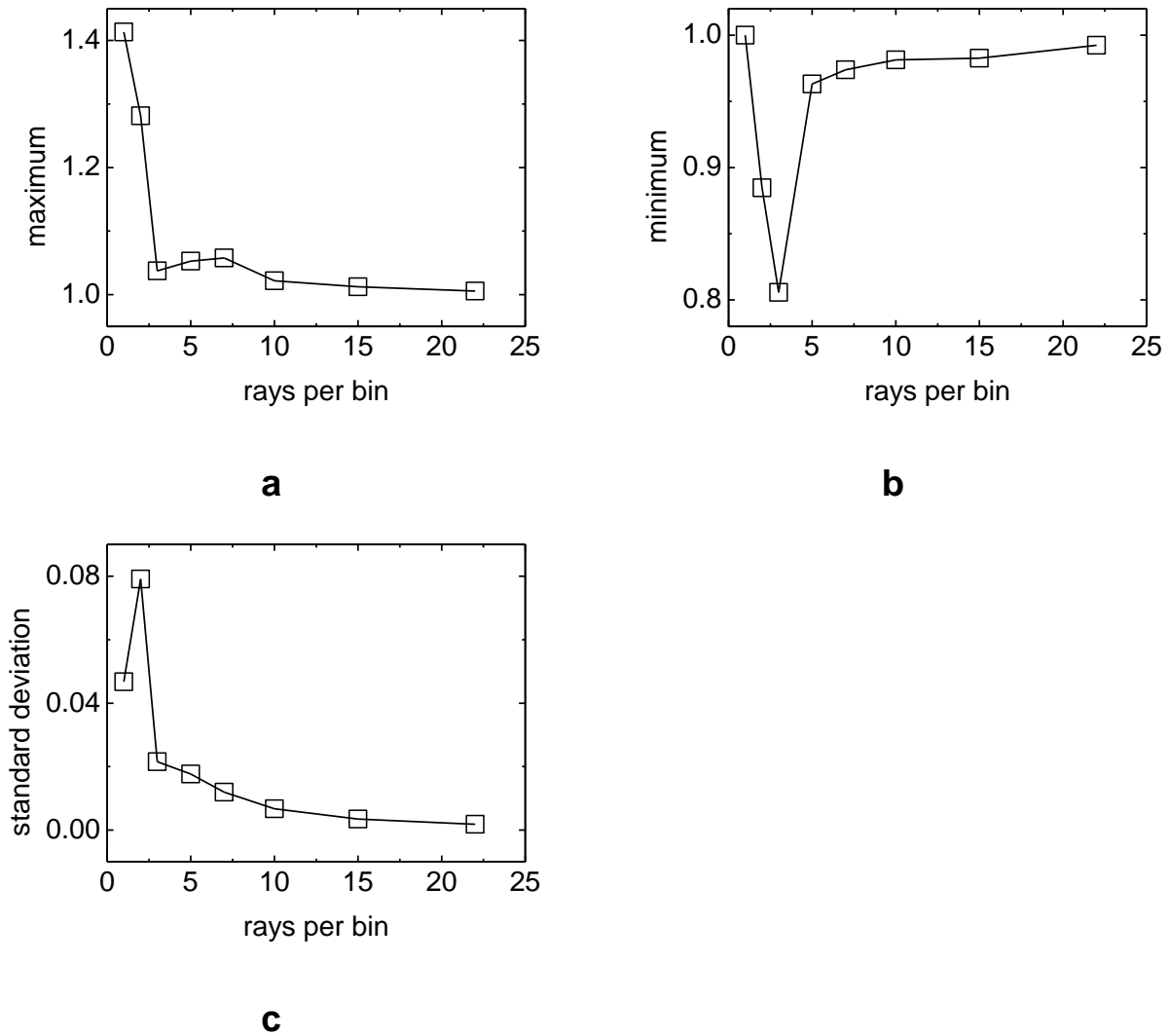


Figure 2.11. Statistics for cone-beam normalized sensitivity patterns NSP within the slice furthest from the central slice versus number of rays per detector bin. Shown are (a) maximum and (b) minimum of the NSP across the reconstruction space and (c) standard deviation of NSP.

For a cone-beam collimator with the detector and reconstruction space parameters above, 5×5 rays per bin are required to achieve a mean NSP very close to unity. A standard deviation of the NSP less than 1 % was obtained when 10×10 or more rays per bin were used. A maximum/minimum of $\pm 5\%$ was obtained when 10×10 or more rays per bin were used.

2.6 Conclusions

In this section, we have introduced the formulation of fully three-dimensional, voxel-based system matrix in parallel-beam, fan-beam, and cone-beam collimator geometries while modeling the process of attenuation, system resolution, and sensitivity. This was achieved by casting rays through a volume of voxels and using ray-voxel intersection lengths to determine approximate volume contributions. The NSP was used to determine the optimum number of rays to be used per detector bin for a given geometry and sampling.

Chapter 3. Cone-Beam Collimator with Helical Orbit

3.1 Objective

The objective of this study was to investigate reconstructed image quality for datasets that used helical orbits under the constraint of fixed total acquisition time and fixed radiopharmaceutical dose using a system matrix described in Chapter 2. Also, we investigated using either a staggered OS grouping or an in-plane grouping.

3.2 Introduction

It is well known that cone-beam collimators allow for higher sensitivity and resolution relative to fan-beam and parallel-beam collimators. However, when single-circular orbits are used, transaxial and axial distortion artifacts result due to insufficient sampling of the projection data. Tuy [44] and later Smith [45] formulated the required conditions for sufficiently sampling the datasets in the context of inversion-based reconstruction.

In this section, we consider a triple-head gamma camera and examine how sampling, using a helical orbit and constrained by total scan time and administered dose, affects image quality. Sampling is described by both rotation and translation. Since we are considering helical orbits with a fixed translational length and 360° rotation, rotational sampling and translational sampling are coupled. Under the constraint of fixed total acquisition time and fixed radiopharmaceutical dose, higher rotational sampling yields noisier projections due to less information being collected per projection. This allows for a tradeoff between sampling and the signal-to-noise ratio (SNR) for a projection.

3.3 Methods

The simulated object consists of five “hot” (radioactive) cylinders embedded within a large cold cylinder and is shown in Fig. 3.1. The small cylinders were simulated as polymethyl methacrylate (PMMA) and the large cylinder in which they are embedded as water. The diameters of the five small cylinders ranged from 2.2 cm to 0.44 cm. The activity concentration ratio between the small and large cylinders is 3:1. The total activity was fixed at 3000 MBq for this phantom and the total scan time was constrained to 1,800 s.

A triple-head SPECT detection system with cone-beam collimators was used. We investigated reconstruction performance based on various rotational and translational sampling and corresponding single-to-noise ratios (SNRs). The rotational sampling considered consisted of 90, 120, 180, and 360 views over 2π radians, which translates to 30, 40, 60, 120 views per detector head over $-\pi$ radians. Application of a triple-head detection system allows for sampling the reconstruction space from three angles separated by $-\pi$ radians per camera rotation versus a single-head system that allows for only one view per camera rotation. In this case, pitch is defined as the axial distance between locations of the focal point before and after a $-\pi$ rotation of a single detector head. The total translational distance covered was 6.6 cm.

Three low-energy ultrahigh-resolution (LEUR) cone-beam collimators were considered. The detector and collimator parameters are given in the Appendix, Table A.2. The radius-of-rotation (ROR) was 14.08 cm.

One noiseless and four noisy datasets were considered. The noiseless dataset was created using the same projector that was used for reconstruction. This allowed for analyzing reconstruction artifacts that might be masked or hidden otherwise. The noisy datasets were simulated using the Monte Carlo-based SIMIND software. This allows for analyzing how the

noise propagation from the data to the reconstructed image is handled. Examples of selected projections are shown in Fig. 3.2.

An ordered-subset version of the EM algorithm (OSEM) was used for reconstruction [19]. An OS number of 6 was used. We investigated using either a staggered OS grouping or an in-plane grouping. Ordered subsets, In-plane groupings are sets of projections in which the focal points for the three detectors are in the same plane and staggered groupings are ones in which the focal points are not in the same plane. The reconstructed voxel size was $(0.22 \text{ cm})^3$ and the space resolution was $128 \times 128 \times 64$. An exact attenuation map was used. Resolution and sensitivity compensation was implemented according to the method described in Chapter 1.1.6 and the parameters of which are listed in the Appendix. Neither post smoothing nor regularization were used. The system matrix was created using 16 rays per detector bin.

Cylinder	Diameter (cm)
1	2.20
2	1.76
3	1.32
4	0.88
5	0.44
water	17.6

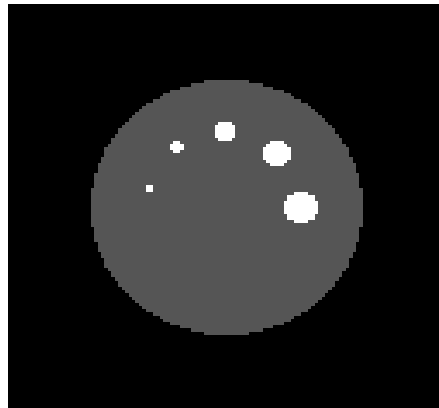


Figure 3.1. Digital phantom used for cone-beam collimator with helical orbit SPECT study. Five cylindrical rods are shown embedded in a large cylinder. The ratio of activity between the small cylinder and background is 3:1.

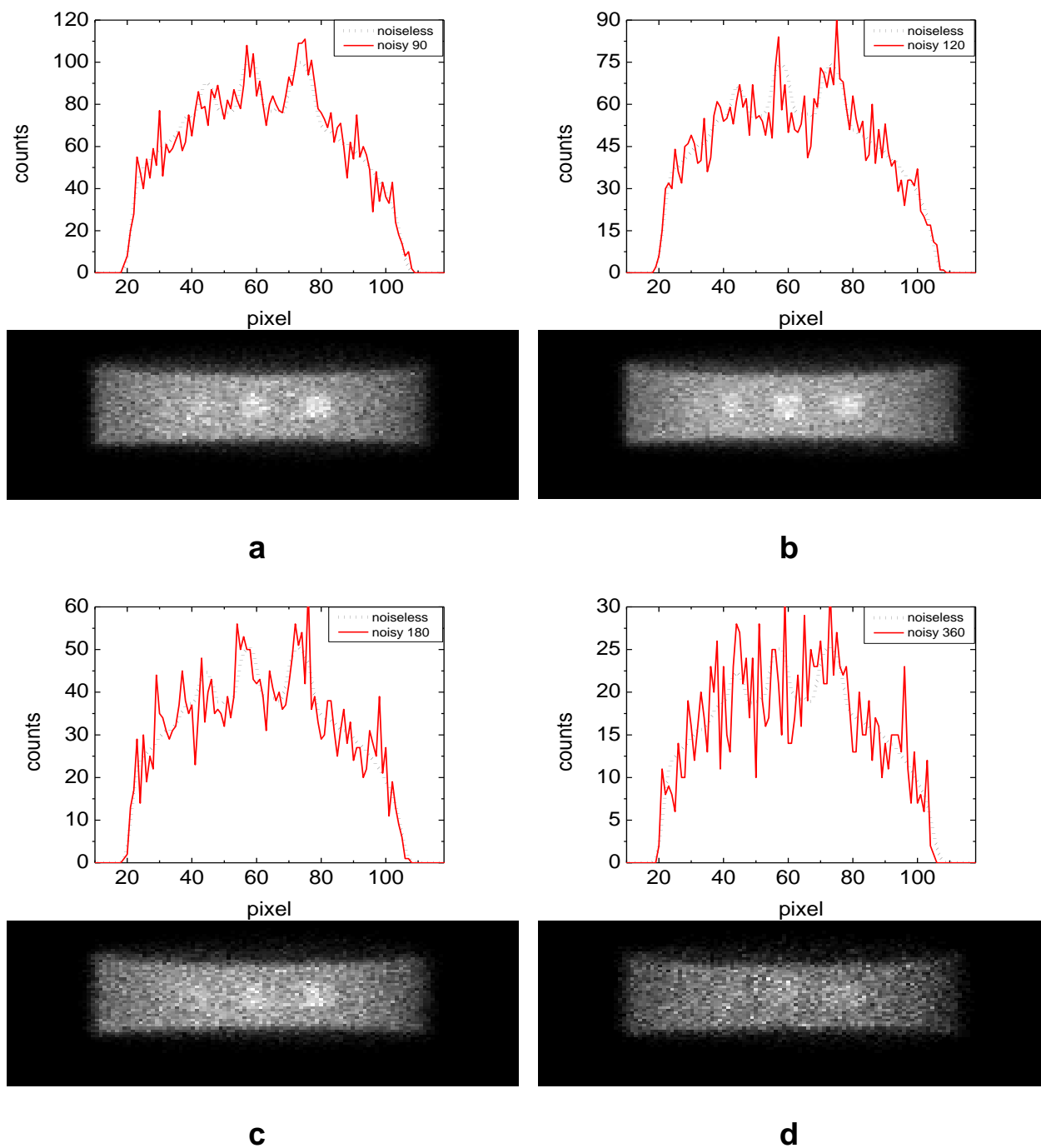


Figure 3.2. Illustration of helical cone-beam noisy datasets created using SIMIND. Shown are line profiles through the noisy datasets superimposed over line profiles through the noiseless dataset. Underneath each plot is a sample of the corresponding dataset. Datasets were created using various numbers of views per projection: (a) 90, (b) 120, (c) 180, and (d) 360. Notice that as the number of views per projection increases, the noise per projection increases as well as the rotational and translational sampling.

3.4 Results

Noiseless Dataset

The reconstructed image quality was assessed using the mean-to-actual ratio (MAR), defined in Chapter 1.4, within hot cylinders of various sizes. Also, line profiles across various regions were used to assess spatial resolution and accuracy. Figure 3.3 shows plots of the MAR within various sized cylinders versus iteration for staggered and in-plane OS-groupings. Datasets did not contain Poisson noise. From Fig. 3.2 we see that: 1) convergence is slower for smaller sized hot cylinders, 2) In-plane OS grouping outperforms staggered grouping for all sized cylinders, and that 3) the MAR approaches unity as the cylinder size increases.

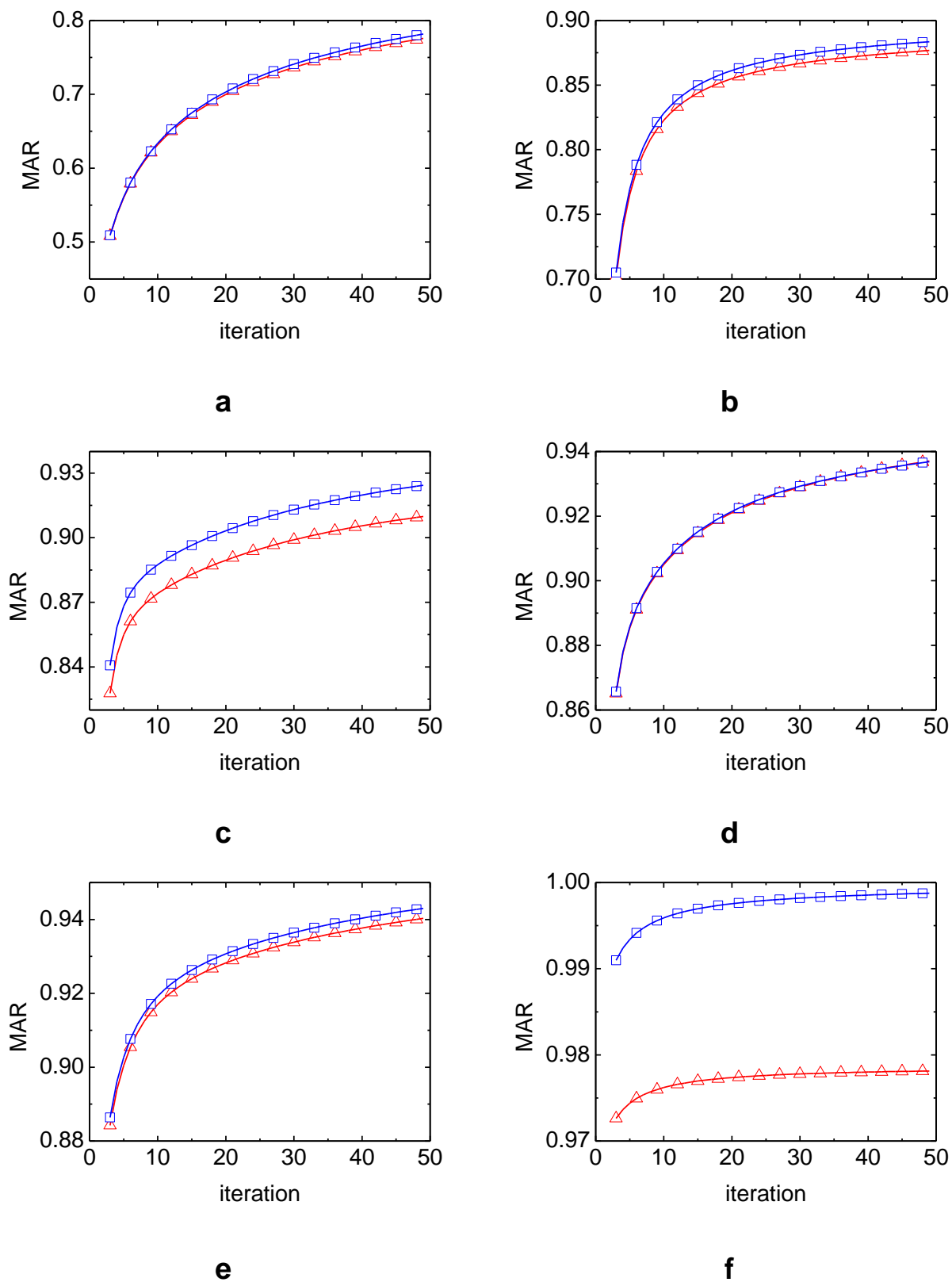


Figure 3.3. MAR vs. iteration within various sized cylinders using two OS grouping methods. Cylinder diameters are; (a) 0.44 cm, (b) 0.88 cm, (c) 1.32 cm, (d) 1.76 cm, (e) 2.20 cm, and (f) is the background

(Figure 3.2 continued) which the smaller cylinders are imbedded. Datasets were noiseless. Each graph displays two curves. The curve using blue squares is an ordered-subset which consists of projections in which the focal points for the three detector heads are located within the same plane along the transaxial direction (in-plane OS) and the red triangles represent a group where the focal points are out of plane (staggered OS).

Transaxial line profiles across the 2.2 cm diameter cylinder and a line profile through the uniform region along the axial direction are shown in Fig. 3.4. Datasets did not contain Poisson noise. By analyzing Fig. 3.4 we conclude that: 1) in-plane and staggered OS groupings were comparable in terms of resolution and noise for slices close to the central slice, and 2) in-plane OS outperformed staggered OS grouping in terms of resolution and noise for slices further from the central slice.

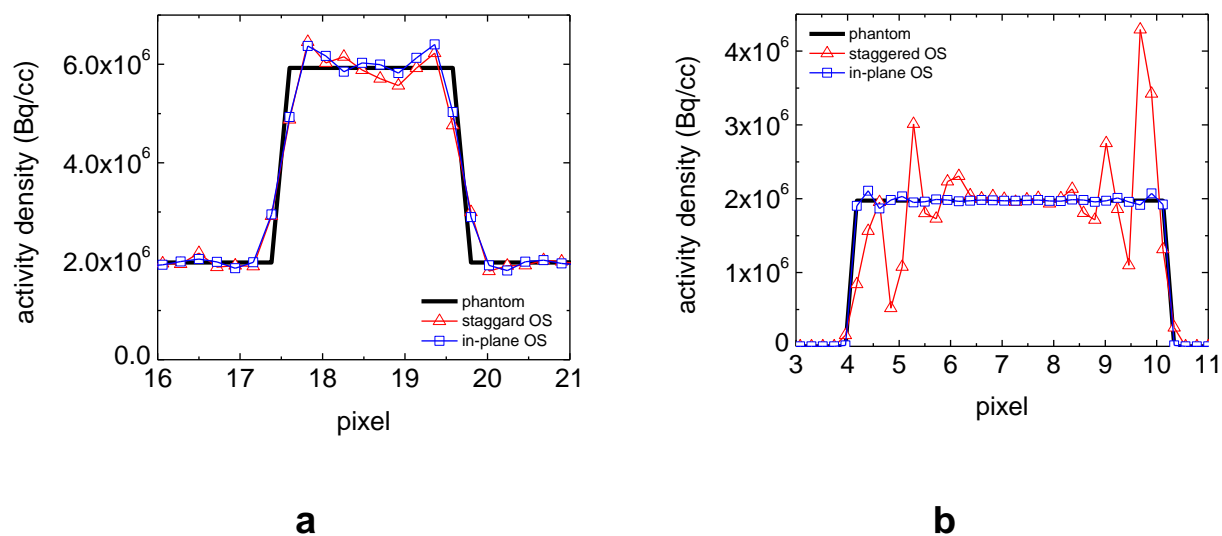


Figure 3.4. (a) Line profile within center slice across hot cylinder along the transaxial direction. (b) Line profile through the uniform background along the axial direction. Staggered subset is represented by squares and in-plane subsets by triangles. Datasets were noiseless.

We also visually examine the image artifacts of the reconstructed images when using different ordered-subsets groupings. Figure 3.5 shows central and off-center slices. With both OS

groupings, Gibbs ringing is evident in locations where there are sharp edges. These artifacts appear as “overshoots” when going from hot to cold region and “undershoots” from cold to hot. In slices further from the central slice, one can observe strong sampling artifacts when using a staggered grouping, versus an in-plane grouping.

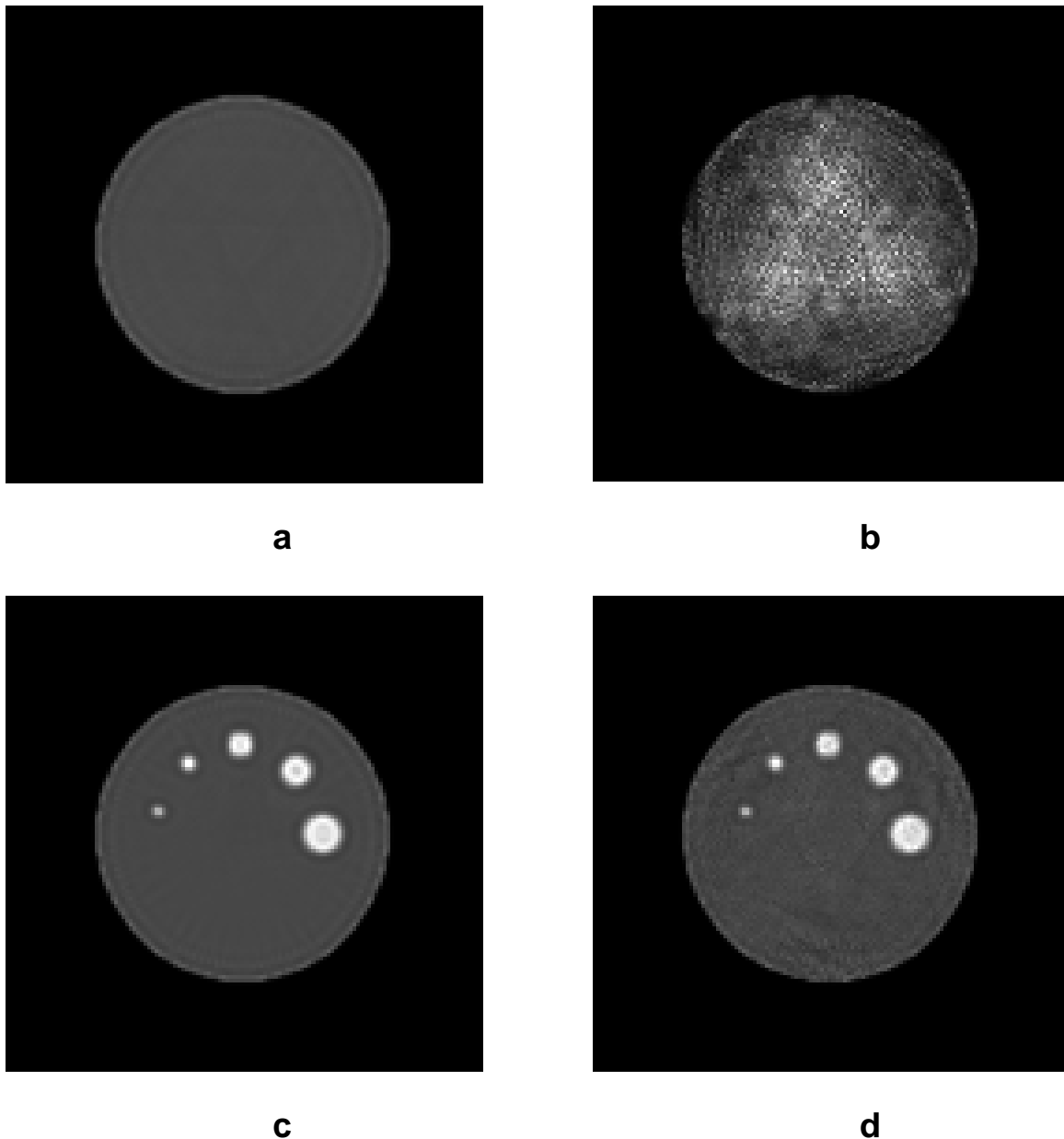


Figure 3.5. The top row shows slices through the uniform region reconstructed using (a) In-plane subset grouping and (b) staggered subset grouping. The bottom row shows slices through the five hot cylinders reconstructed using (c) In-plane subset grouping and (d) staggered subset grouping. The images in (a) and (c) contain fewer reconstruction artifacts than (b) and (d).

Noisy Datasets

Figure 3.6 shows plots of the MAR within various sized cylinders versus iteration for datasets acquired using 90, 120, 180, and 360 views with a fixed total dose and scan time. In-plane OS was used. Datasets contained Poisson noise and were acquired using 90, 120, 180, and 360 views with a fixed total dose and scan time. Therefore, there is a tradeoff between sampling and SNR. By analyzing these plots we conclude that: 1) Convergence increases with increasing object size regardless of sampling, 2) MAR converges to values closer to 1 for larger objects, 3) the MAR associated with noisy datasets is smaller than that of noiseless datasets and 4) there is no noticeable difference between the four different samplings.

Table 3.1. MAR within reconstructed cylindrical rods for noisy datasets at iteration 20 when angular views ranged from 90 to 360.

cylinder diameter (cm)	90 views	120 views	180 views	360 views
2.20	0.718	0.719	0.730	0.723
1.76	0.733	0.702	0.720	0.718
1.32	0.702	0.688	0.698	0.720
0.88	0.672	0.633	0.668	0.659
0.44	0.498	0.507	0.512	0.517

Table 3.2. Standard deviation within reconstructed cylindrical rods for noisy datasets at iteration 20 when angular views ranged from 90 to 360.

cylinder diameter (cm)	90 views	120 views	180 views	360 views
2.20	0.152	0.148	0.154	0.144
1.76	0.151	0.149	0.160	0.140
1.32	0.178	0.163	0.165	0.187
0.88	0.180	0.109	0.151	0.149
0.44	0.099	0.098	0.087	0.081

Table 3.3. Uniformity within reconstructed cylindrical rods for noisy datasets at iteration 20 when angular views ranged from 90 to 360.

cylinder diameter (cm)	90 views	120 views	180 views	360 views
2.20	0.527	0.548	0.576	0.554
1.76	0.537	0.524	0.594	0.503
1.32	0.574	0.568	0.502	0.562
0.88	0.508	0.339	0.453	0.485
0.44	0.335	0.401	0.333	0.372

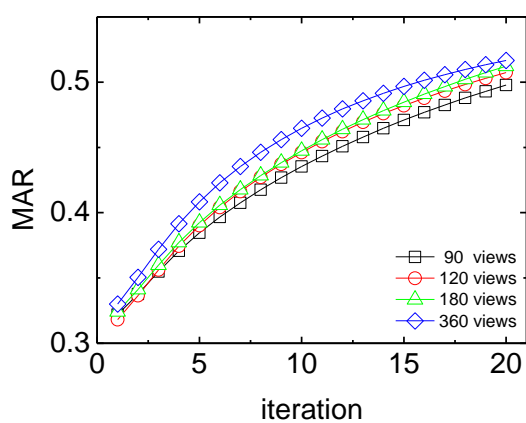
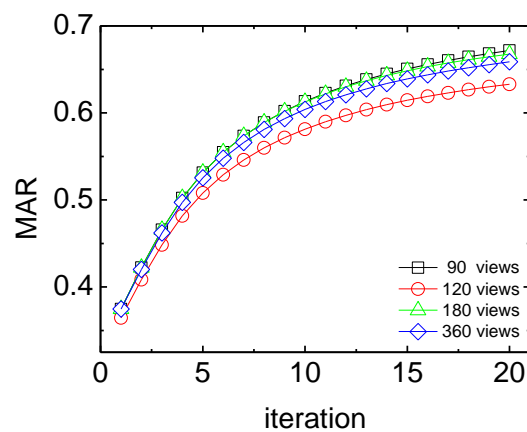
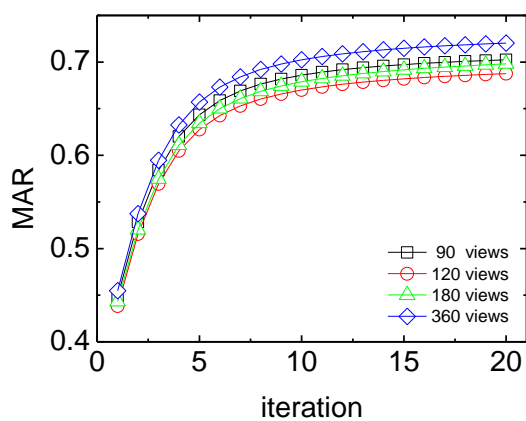
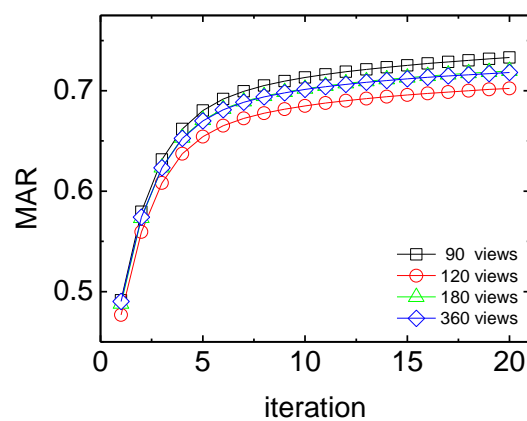
**a****b****c****d**

Figure 3.6. MAR vs. iteration within various sized cylinders. Cylinder diameters are; (a) 0.44 cm, (b) 0.88 cm, (c) 1.32 cm, and (d) 1.76 cm. Datasets contained Poisson noise. Each graph displays four curves corresponding reconstructions of projections containing 90, 120, 180, and 360 views with total scan time and administered dose fixed.

3.5 Conclusions

Here, the reconstruction performance was studied for a triple-head cone-beam SPECT system using a helical orbit acquisition. We looked at various subset groupings for the ordered-subsets expectation maximization (OSEM) algorithm. We also examined how rotational and translational sampling affects reconstructed image quality when constrained by total injected dose and scan time. We conclude the following. When reconstructing noiseless or noisy datasets, varying the rotational sampling from 90 views to 360 views over 360 degrees does not affect the reconstructed activity, regardless of the object size, in terms of both convergence and accuracy. When using ordered subsets, the subset group arrangement is important in terms of both image quality and accuracy. The rate of convergence is less when reconstructing small objects versus larger ones. Spatial resolution and accuracy are worse when reconstructing small objects versus larger ones.

Chapter 4. Converging Collimators with Circular Orbit

4.1 Objective

The objective of this study was to determine the reconstruction performance when using a triple-head system with various combinations of converging collimators with a circular orbit while varying the number of angular views using a system matrix described in Chapter 2. A cone-beam collimator was used to increase sensitivity in both the transaxial and axial directions. Fan-beam collimators were used to achieve sufficient sampling along the axis-of-rotation.

4.2 Introduction

Both cone-beam and fan-beam collimators offer increased sensitivity in comparison to parallel-beam ones. Cone-beam increases sensitivity along both the transaxial and axial directions while fan-beam offers an increase only along the transaxial. This increase in sensitivity is offset by insufficient sampling. Various combinations of collimators have been studied including parallel-beam and fan-beam [46], and parallel-beam and cone-beam [47,48]. In this section we further investigate using a combination of cone-beam and fan-beam collimators with a circular orbit acquisition employing a system matrix described in Chapter 2.

4.3 Methods

The object consisted of five hot cylinders imbedded within a large cold cylinder as shown in Fig. 4.1. The small cylinders were composed of PMMA and the large one was composed of water. The diameters of the five cylinders ranged from 0.44 to 2.2 cm. The concentration ratio

between the small and large cylinders was 3:1. The total activity was fixed at 3000 MBq for this phantom, and the total scan time was constrained to 1,800 s.

A triple-head SPECT detection system with combinations of low-energy ultra high resolution (LEUR) fan-beam collimators (FBC) and cone-beam collimators (CBC) were used. The detector and collimator parameters are given in the Appendix, Table A.2. The radius-of-rotation (ROR) was 14.08 cm. The angular sampling was 120 views over 2π radians, which translates to 40 views per detector head over $-\pi$ radians. Application of a triple-head detection system allows for sampling the reconstruction space from three angles separated by $-\pi$ radians per camera rotation versus a single-head system that allows for only one view per camera rotation. The combinations of collimators studied included; CBC-CBC-CBC (CCC), CBC-CBC-FBC (CCF), CBC-FBC-FBC (CFF), and FBC-FBC-FBC (FFF).

Both noiseless and noisy datasets were considered. The noiseless dataset was created using the same projector that was used for reconstruction. This allowed for analyzing reconstruction artifacts that might be masked or otherwise hidden. The noisy datasets were simulated using the Monte Carlo-based SIMIND software. This allows for analyzing how noise propagation from the data to the reconstructed image is handled.

An ordered-subset version of the EM algorithm (OSEM) was used for reconstruction [19]. An OS number of 9 was used with in-plane grouping. The reconstructed voxel size was $(0.22 \text{ cm})^3$ and the spatial resolution was $128 \times 128 \times 64$. An exact attenuation map was used. Resolution and sensitivity compensation was established according to Chapter 1.1.6 and the parameters of which are listed in the Appendix. Post smoothing and regularization were not used. The system matrix for the CBC was created using 16 rays per detector bin, and the FBC was created using 4 rays per bin.

Cylinder	Diameter (cm)
1	2.20
2	1.76
3	1.32
4	0.88
5	0.44
water	17.6

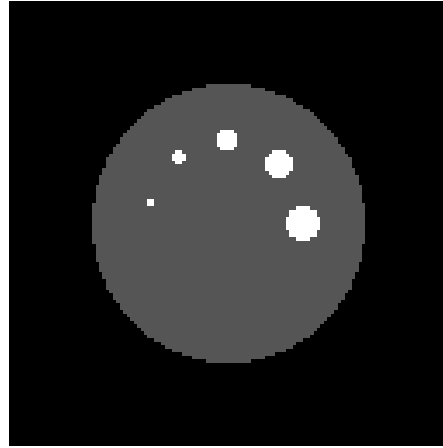


Figure 4.1. Digital phantoms that were used for converging collimator with circular orbit SPECT study. Five cylindrical rods embedded in a large cylinder. The ratio of activity between the small cylinder and background is 3:1.

4.4 Results

The reconstructed image quality was assessed using the mean-to-actual ratio (MAR) and standard deviation (SD) of activity distribution, both are defined in Chapter 1.4, within hot cylinders of various sizes. Also, line profiles across various regions were used to assess spatial resolution and accuracy. Figure 4.1 shows reconstructed images using various combinations of collimators. The top row corresponds to noiseless datasets and the bottom to noisy. By analyzing these images, it is evident that sampling artifacts are visible when using CCC and decrease going from CCC to CCF to CFF to FFF.

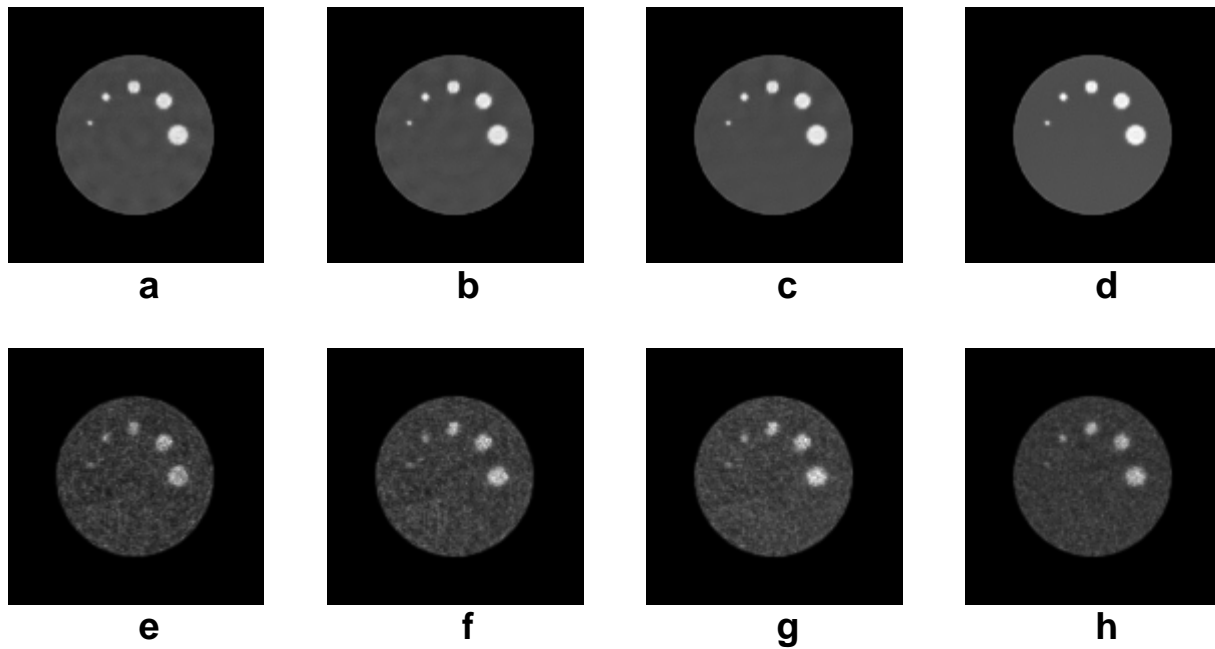


Figure 4.2. Reconstructed images of cylinder phantom using various combinations of converging collimators. Top row corresponds to noiseless datasets, and bottom to noisy datasets. (a) and (e) CCC. (b) and (f) CCF. (c) and (g) CFF. (d) and (h) FFF.

Figure 4.3 shows a line profile across an in-plane uniform region of water and through the water-air boundary along the axis-of rotation. By analyzing these plots we conclude: 1) there are strong transaxial and axial artifacts when using a CCC system, 2) these artifacts decrease as we go towards a FFF system and 3) resolution along both transaxial and axial directions is best when using a FFF system.

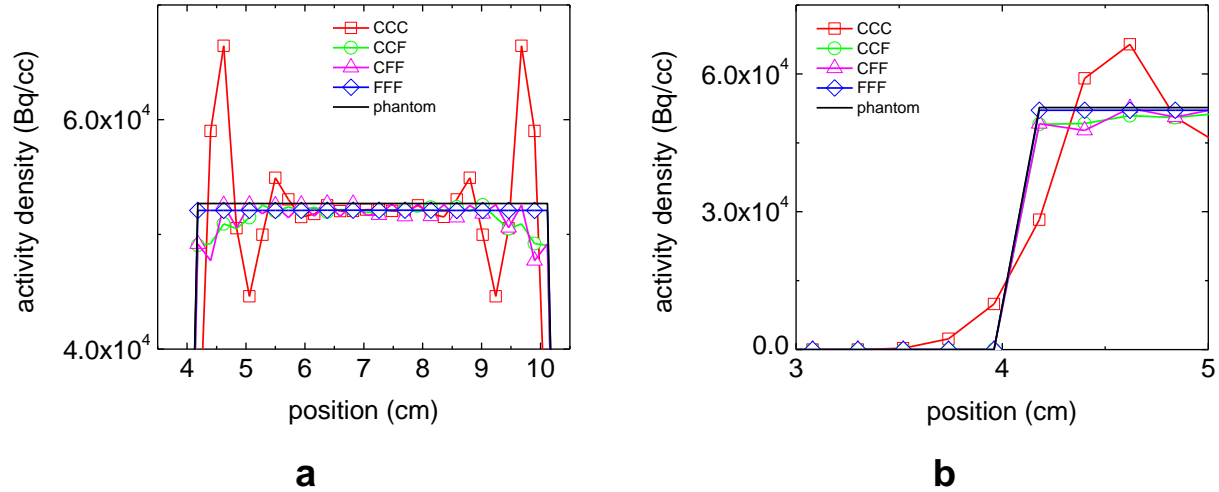


Figure 4.3. Line-profile through a 4 cm diameter ROI along the axial direction. Reconstructions are of the cylinder phantom that was imaged over 120 views using various combinations of converging collimators. Datasets were noiseless. (a) Line-profile across a uniform region of the main cylinder. (b) Resolution between main cylinder and air.

Table 4.1. MAR, SD, and uniformity for a 4cm diameter ROI within a uniform region of water. Reconstructions are of the cylinder phantom that was imaged over 120 views using various combinations of converging collimators. Datasets were noiseless.

Combination	MAR	SD	uniformity
CCC	0.987	0.035	0.105
CCF	0.990	0.030	0.090
CFF	0.979	0.023	0.069
FFF	0.989	0.012	0.040

Figure 4.4 shows plots of the MAR within various sized cylinders versus iteration. Datasets contained Poisson noise. By analyzing these plots we conclude that: 1) Convergence increases with increasing object size regardless of system of collimators, 2) MAR converges to values closer to unity for larger objects, and 4) there is no noticeable difference between the four systems of collimators.

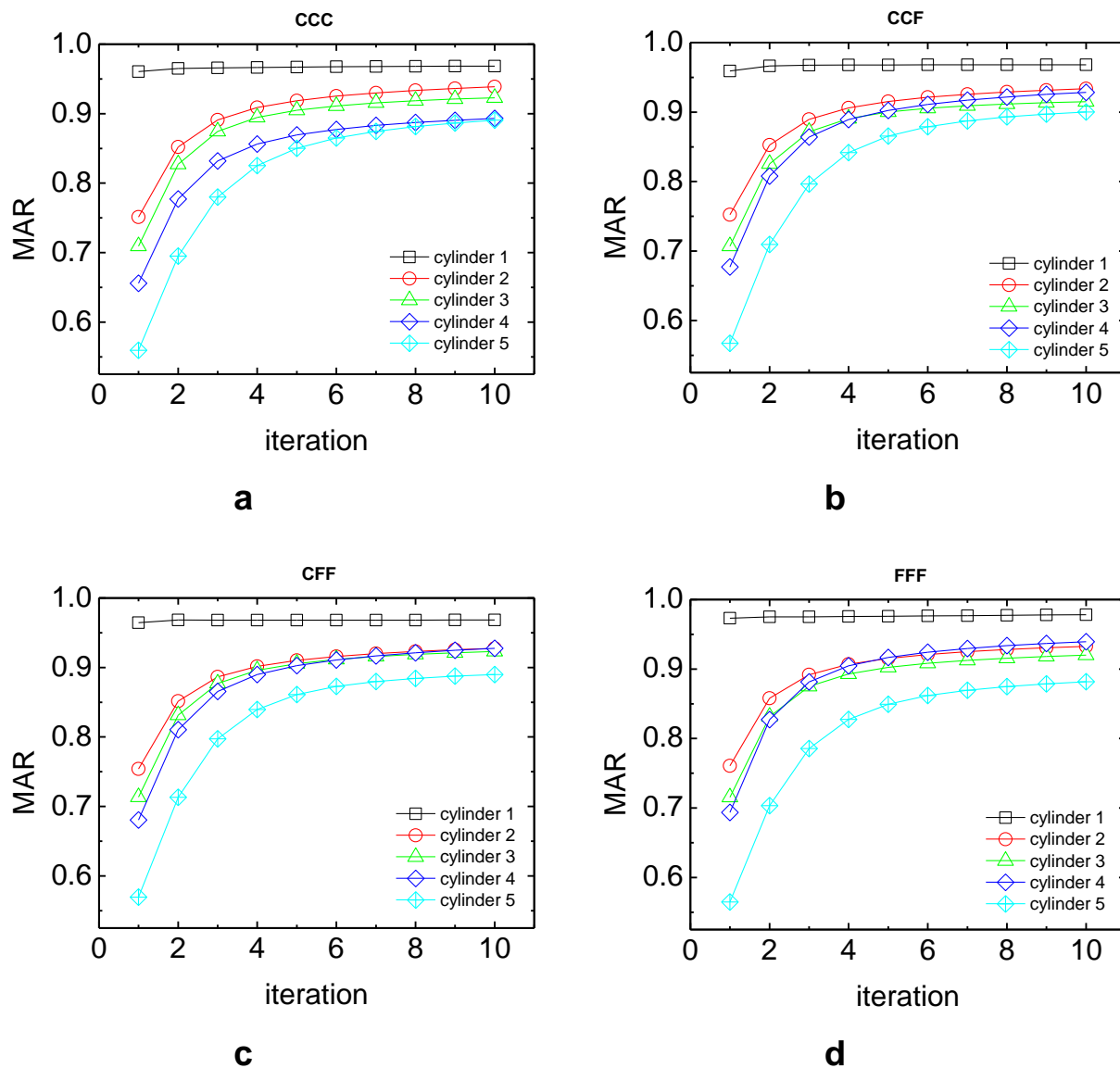


Figure 4.4. MAR within small cylinders versus cylinder volume. Reconstructions are of the cylinder phantom that was imaged over 120 views using various combinations of converging collimators. Datasets contained Poisson noise. (a) CCC, (b) CCF, (c) CFF, and (d) FFF.

4.5 Conclusions

We examined a system composed of three possibly different converging collimators using a circular orbit. We conclude the following: When reconstructing noiseless datasets, using a triple-cone beam system resulted in axial distortion artifacts and diminished resolution along the transaxial direction. Using a triple-fan beam system resulted in the best reconstructed image quality in terms of bias, noise, and contrast. When noisy datasets were reconstructed, a cone-fan beam system resulted in best reconstructed image quality in terms of mean-to-actual ratio for small lesions and a triple-fan beam system for large lesions.

Chapter 5. System Matrix in Mesh Domain

5.1 Objective

The purpose of this study was to develop and implement an accurate and computationally efficient method for determination of the mesh-domain system matrix including attenuation compensation for Ordered Subsets Expectation Maximization (OSEM) Single Photon Emission Computed Tomography (SPECT). The mesh-domain system matrix elements were estimated by first partitioning the object domain into strips parallel to the detector face and with width not exceeding the size of a detector unit. This was followed by approximating the integration over the strip/mesh-element union. This approximation is the product of: (i) strip width, (ii) intersection length of a ray central to strip with a mesh element, and (iii) the response and expansion function evaluated at midpoint of the intersection length. Reconstruction was performed using OSEM without regularization and with exact knowledge of the attenuation map. The method was evaluated using synthetic SPECT data generated using SIMIND Monte Carlo simulation software. Comparative quantitative and qualitative analysis included: bias, variance, standard deviation and line-profiles within three different regions of interest. We found that no more than two divisions per detector bin were needed for good quality reconstructed images when using a high-resolution mesh.

5.2 Introduction

The most common basis functions used for SPECT reconstruction are 3-D rect-functions or voxels. A voxel is a cubic volume element in which the expected activity is uniform within. Although this voxel-based representation has many attractive features in terms of computation,

non-constant basis functions have been shown to have advantages, as well. In 1992, Lewitt [5] introduced Bessel-Kaiser base functions (Blobs), which were later shown to reduce noise and increase accuracy in reconstructed images [49]. Recently, mesh-based image representation has been studied in the context of emission tomography reconstruction [50,51]. This approach might offer significant advantages over voxel-based approaches. One benefit is that fewer mesh nodes are required to accurately characterize an image, as compared to the number of pixels or voxels that are required for the same task. Consequently, the ill-posed inverse problem of reconstruction from a limited number of projections becomes better regularized. Also, the mesh framework allows for natural motion compensation. Before its application to emission tomography, mesh modeling had been applied to various areas of image processing, including image compression, motion tracking and compensation, and medical image analysis [52]. The mesh-based representation partitions the reconstruction space into non-overlapping triangular (2-D) and tetrahedral (3-D) patches called mesh elements. Each mesh element is defined by either three (2-D) or four (3-D) nodes.

5.3 Methods

5.3.1 Mesh

In this study, the MESD2D MATLAB toolbox by Darren Engwirda [53] was used to generate the mesh structure. Element size was adapted to ensure that the geometry was adequately resolved. Exact anatomical prior information was used to define the geometry and attenuation coefficients at nodal locations. This prior information was based on the NURBS-based cardiac-torso XCAT phantom version 2.07 [54]. An example of a mesh along with the

corresponding digital atlas is shown in Fig.5.1. This mesh consists of 7060 nodes connecting 14086 triangles. The smallest element size was 0.085 pixels and the largest was 145.5 pixels.

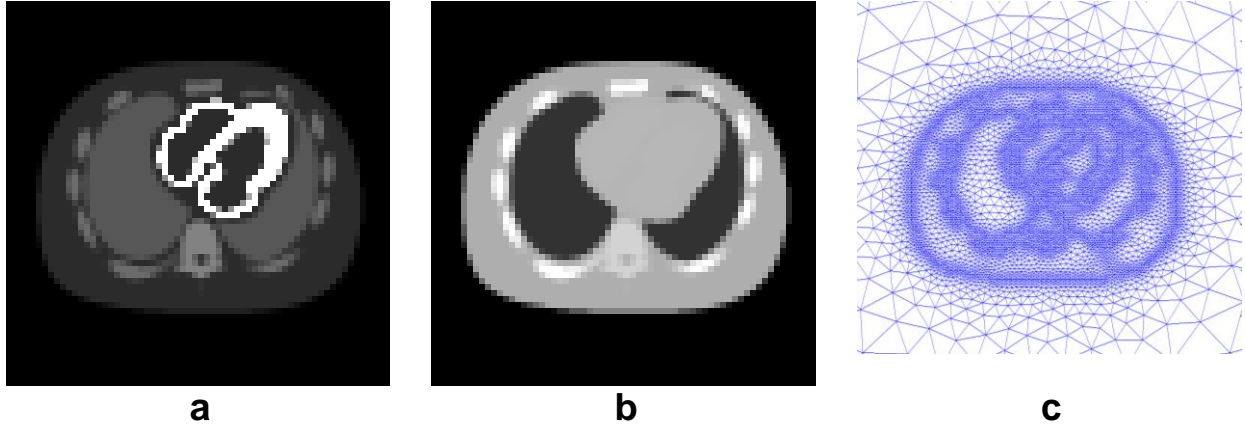


Figure 5.1. (a) NCAT activity map. (b) NCAT attenuation map. (c) Mesh consisting of 7060 nodes and 14,086 triangles. For clarity only center region of mesh is shown (80×80 pixels out of 128×128 pixels).

5.3.2 System Matrix

The deterministic portion of the imaging equation relating the continuous activity distribution to the discrete detection of gamma photons is

$$\bar{g}_m = \int_{\Omega} h_m(\mathbf{r}) f(\mathbf{r}) d^2r, \quad (5.1)$$

where $h_m(x)$ $h_i(\mathbf{x})$ is the system response function relating the detector response at bin m to an impulse at location x . The emission distribution $f(x)$ is over object domain Ω . Expanding $f(x)$ in terms of irregular mesh elements defined by N nodes can be expressed as

$$f(\mathbf{r}) \approx \sum_n^N f_n b_n(\mathbf{r}), \quad (5.2)$$

where f_n is the emission distribution defined at the location of the n^{th} node and $b_n(\mathbf{r})$ is the sum of the basis functions attached to node n . Here, we assume a piecewise linear correspondence between nodes. The imaging equation can now be written as

$$\bar{g}_m \approx \sum_n^N f_n \int_{\Omega} h_m(\mathbf{r}) b_n(\mathbf{r}) d^3 r . \quad (5.3)$$

The system matrix is defined as

$$a_{mn} = \int_{\Omega} h_m(\mathbf{r}) b_n(\mathbf{r}) d^3 r . \quad (5.4)$$

The aim of this study was to approximate this integral using numerical integration. This approximation was carried out by first partitioning the object domain into strips parallel to the detector face and with width not exceeding the size of a detector unit. The more divisions per detector bin, the more accurate the numerical integration. Of course, there is a trade-off between accuracy and computation speed.

For the purpose of this study, the response function for an ideal parallel-beam collimator/detector system was considered. Only attenuation using narrow-beam geometry was modeled. The other image degrading phenomena including spatially varying resolution, Compton scattering, and partial-volume effects were not considered. Let the width of a detector bin be w and the number of divisions per bin be denoted as d . Also, let the intersection length of a mesh element e and a ray associated with bin i running down the center of division r be denoted l_{mer} (Fig. 2c). Then, an approximation to Eq. (5.4) can be expressed as

$$a_{mm} \approx \sigma \sum_r^R \sum_e^{\text{elements attached to node } j} b_n(\tilde{l}_{mer}) l_{mer} \frac{w}{R} \exp \left\{ -\frac{1}{2} \mu(\tilde{l}_{mer}) l_{mer} - \sum_{k \neq e}^{\text{elements downstream of } e} \mu(\tilde{l}_{mkr}) l_{mkr} \right\} \quad (5.5)$$

Where $b_n(\tilde{l}_{mer})$ is the linear basis function associated with the n^{th} node (with the n^{th} node set to a value of 1 and all other nodes set to 0) evaluated at the midpoint of the intersection length \tilde{l}_{mer} .

For the attenuation portion within the exponential, $\mu(\tilde{l}_{mer})$ represents the attenuation coefficient evaluated at \tilde{l}_{mer} . The constant parallel-beam sensitivity factor is σ .

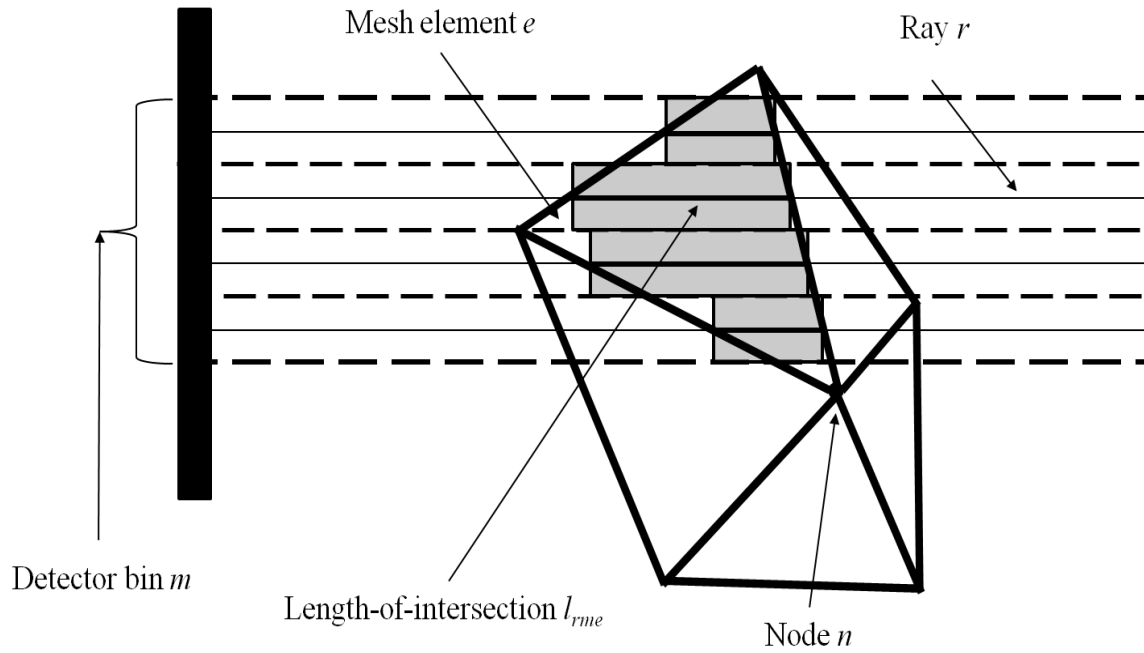


Figure 5.2. Intersection of mesh element and detector bin using 4 divisions per bin.

5.3.3 Projection Set

The activity-distribution and attenuation-coefficient maps were generated using the NURBS-based cardiac-torso XCAT phantom version 2.0 [54]. These maps correspond to gamma emission of Tc-99^m with mean energy of 140 keV, and are shown in Fig. 5.1. The Monte Carlo simulation code, SIMIND, was used to simulate a simplified SPECT imaging system [25]. The detector consisted of a one-dimensional array of 128 elements with a pixel size of 0.625 cm. Compton scattering was not modeled. The collimator and detector were modeled as being ideal. This included a) accepting only photons normal to the detector face, b) no collimator penetration, and c) perfect detector resolution. Poisson noise was added to the projection sets. Two different noise levels were considered: high noise (10%) and low noise (1%). These data sets are shown in Fig. 5.3.

5.3.4 Reconstructions

Reconstructions were achieved using the standard Ordered Subsets Expectation Maximization (OSEM) algorithm with OS = 5 [19]. Regularization techniques were not used. Up to 100 iterations were employed. Examples of reconstructed images are shown in Fig. 5.3.

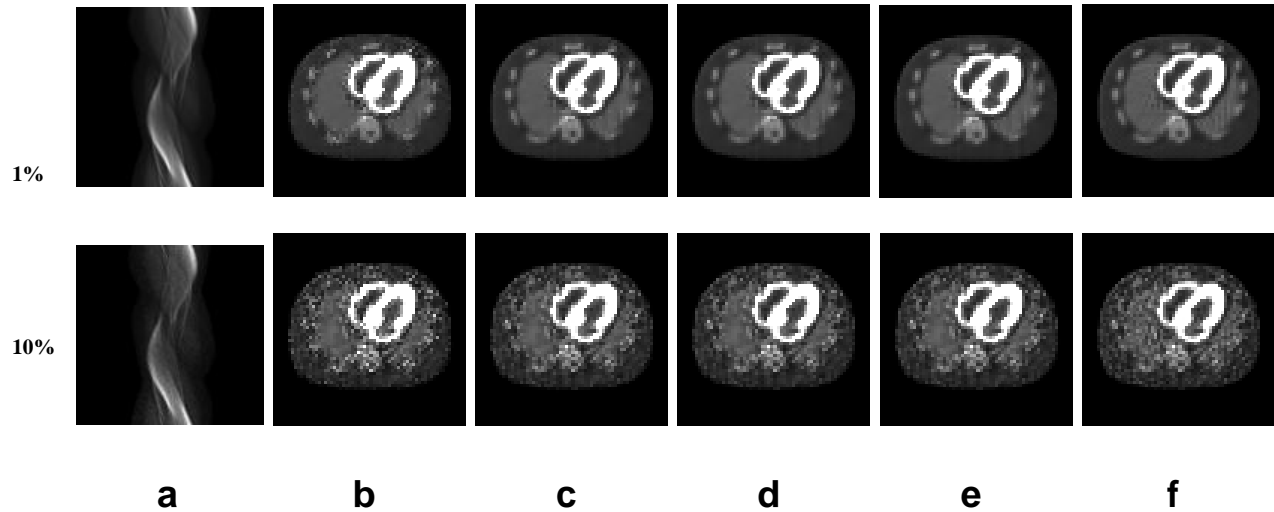


Figure 5.3. Data sets and reconstructed images. First row corresponds to low noise dataset and second row to high noise dataset. (a) Sinograms with varying levels of noise of the NCAT chest phantom generated using SIMIND SPECT simulation software. (b) Mesh-based reconstruction using 1 division per bin. (c) Mesh-based reconstruction using 2 divisions per bin. (d) Mesh-based reconstruction using 3 divisions per bin. (e) Mesh-based reconstruction using 10 divisions per bin. (f) Voxel-based reconstruction using 10 divisions per bin.

5.3.5 Evaluation

We evaluated reconstructed image quality based on the normalized mean square error (NMSE) and signal-to-noise ratio (SNR) versus iteration. Three different regions of interest were examined; the entire chest phantom, right lung, and inside the heart wall. In addition to the image quality measures listed above, line-profiles through the heart and left lung were used to investigate resolution and accuracy of the reconstructed images.

5.4 Results

Plots of NMSE vs. iteration using 1, 2, 3, 5, and 10 divisions per bin for three different regions of interest are shown in Fig. 5.4. We observe that at least 2 divisions per bin are needed for both low and high noise levels. The extent of improvement increases with increasing noise in data.

Plots of SNR vs. iteration using 1, 2, 3, 5, and 10 divisions per bin for regions within the right lung and heart are shown in Fig. 5.5. Within the right lung, we observe only slight improvements when using more than 1 division per bin for both noise levels. Within the heart we observe only slight improvements when using more than 2 division per bin for high noise levels.

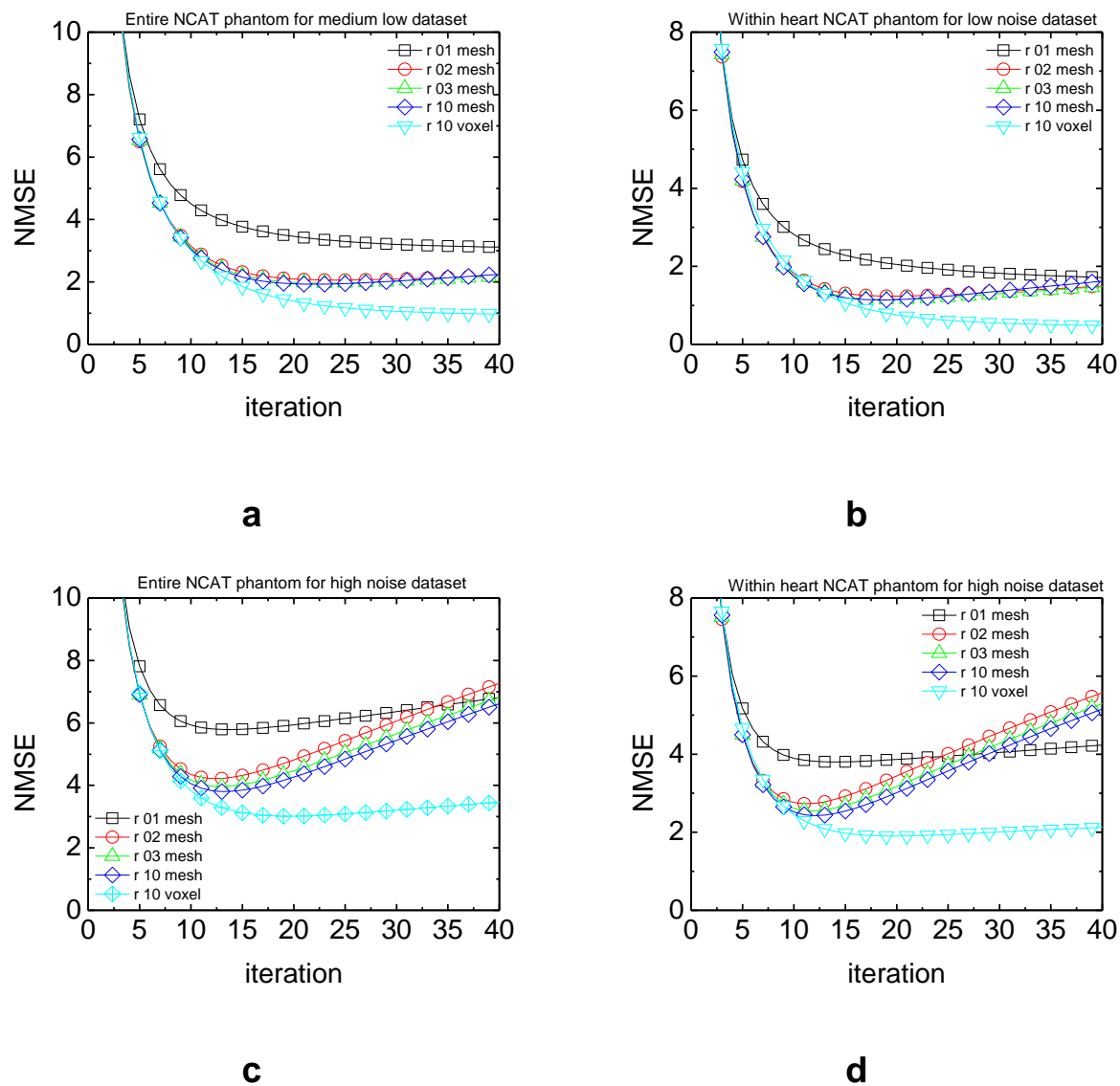


Figure 5.4. Analysis of reconstructed data sets. First, row corresponds to low noise dataset and second row to high noise data sets. Normalized mean square error (NMSE) vs. iteration within the entire chest phantom for high noise dataset (a) and low noise dataset (c). NMSE vs. iteration within the heart for high noise dataset (b) and low noise dataset (c).

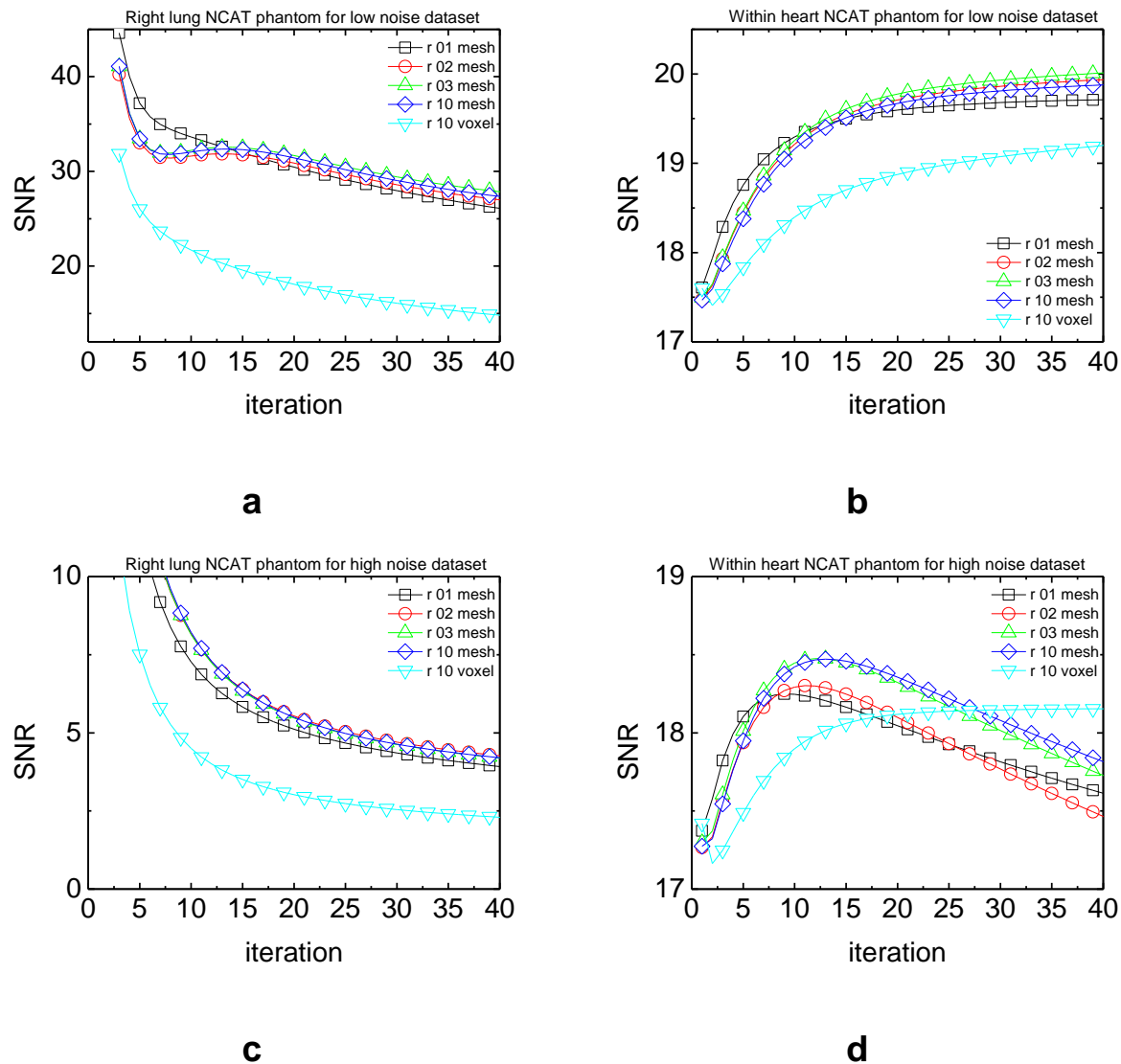
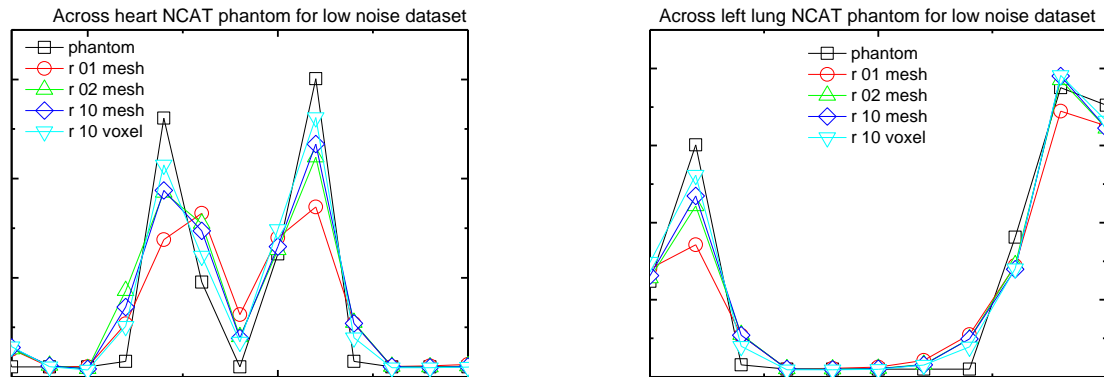


Figure 5.5. Analysis of reconstructed data sets. First, row corresponds to low noise dataset and second row to high noise data sets. Signal-to-noise ratio (SNR) vs. iteration within the right lung for low noise dataset (a) and high noise dataset (c). SNR vs. iteration within the heart for low noise dataset (b) and high noise dataset (c).

Horizontal line profiles through the heart and left lung are shown in Fig. 5.6. We observe that resolution and accuracy are limited when using one division per bin. At least two divisions are needed to produce images with quality comparable to voxel-based reconstruction.



a

b

Figure 5.6. Line profiles through the reconstructed (a) heart and (b) left lung at iteration 20.

5.5 Conclusions

In this chapter we proposed a simple method for estimation of the system matrix for the mesh-domain SPECT reconstruction using a high resolution mesh representation. We found that that no more than two divisions per detector bin width are needed for satisfactory reconstruction. Also, using more than two divisions per detector bin does not significantly improve reconstructed images.

The computational simplicity of our method does come at a price. Since we model the energy flux as being within a region the width of a detector bin and perpendicular to the detector face, resolution modeling might be less accurate than in a cone-of-rays approach [55]. An

adequate way to compensate for this effect might be application of a Gaussian kernel to model realistic point-spread function. Although less computationally expensive, it is also less accurate.

Chapter 6. Volumetric Micro-CT Iterative Reconstruction

6.1 Objective

We have developed a fully volumetric system model for high resolution cone-beam micro-computed tomography (micro-CT) iterative reconstruction. The method consists of partitioning the reconstruction space into slabs that contain the de-magnified detector bin grid and are oriented parallel to the detector face. Results for a reconstructed dead mouse are given.

6.2 Introduction

In this chapter we switch focus from emission tomography to transmission micro-CT. The attenuation coefficient μ for a material quantifies the amount of x-ray photons diverted from the initial direction of propagation within a narrow beam when traversing a thin slice of material. The larger μ is for a material, the more x-ray photons are diverted per unit length of material traversed. The properties of the material that μ depends on are density and effective atomic number. The x-ray property that μ depends on is the energy E , and so we can write $\mu(\mathbf{r}, E)$. For x-ray energies ranging from 10 to 80 keV, the two main mechanisms responsible for attenuation in soft tissue and water are the photoelectric and Compton effects. Refer to Chapter 1.1.5 for μ dependence on material density, atomic number, and x-ray energy.

Computed tomography estimates the object's properties from a series of digital radiographs obtained from different views. Fundamentally, this is a continuous-to-discrete nonlinear mapping [56]. X-rays suffer from Poisson noise and detectors suffer from non-Poisson (Gaussian) noise. This calls for a stochastic treatment. The Boltzmann transport equation can be used to rigorously describe image formation [56].

The goal of polyenergetic transmission tomography with photon-counting detectors is to reconstruct the attenuation coefficient map $\mu(\mathbf{r}, \bar{E})$ at some effective energy \bar{E} . With monoenergetic transmission tomography, the goal is to reconstruct the attenuation coefficient map $\mu(\mathbf{r})$. For this we use a monoenergetic approximation.

Image quality is directly linked to radiation dose. The Poisson noise can be reduced by increasing the intensity of the x-ray source. This leads to a potentially harmful increase in dose administered to the animal.

6.3 Methods

6.3.1 Micro-CT Scanner

The scanner used is the MicroCAT II (Siemens Preclinical Solutions, Knoxville, TN), which provides high resolution (50 μm) imaging designed specifically for small animals. The x-ray source consists of a tungsten anode with a maximum power of 40 W, a voltage range of 35-80 kVp, and maximum anode current of 500 μA . The focal spot size is quoted to be less than 50 μm and the quoted maximum achievable spatial resolution is 27 μm . The x-ray detector consists of 2048 \times 3096 CCD array coupled to a high-resolution phosphor screen designed for high-speed, low-noise, whole mouse imaging. The maximum allowable field of view is 5.4 cm (vertical) \times 8 cm (horizontal). An example of the scanner and detector-object coordinate systems is shown in Fig. 6.1.

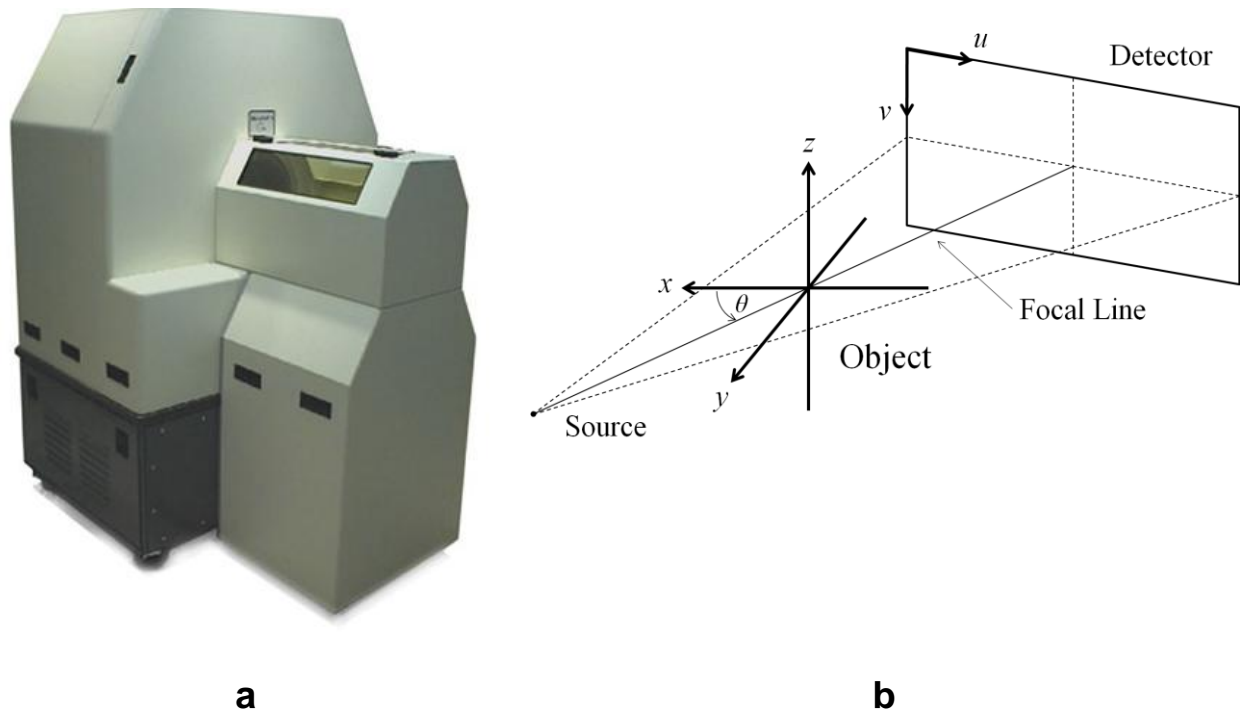


Figure 6.1. (a) MicroCAT II scanner (Siemens) in use at SUNY Upstate Medical University (courtesy of SUNY Upstate Medical University). (b) Detector and object coordinate systems.

For this study, we used an x-ray voltage of 60 kVp, an anode current of 500 μA , and 2 mm of aluminum filtration. The total scan time was 778 s over 360 views, focal length was 426.66 mm, and radius-of-rotation (ROR) was 78.70 mm. The original dataset was at the full resolution of the detector and was then down-sampled by a factor of 8 for reconstruction.

6.3.2 Transmission Imaging Equation

We parameterize the object space according to Chapter 1.1.2; however, the object of interest is now the distribution of the linear attenuation coefficients μ . The expansion of $\mu(\mathbf{r})$ has the form

$$\mu(\mathbf{r}) \approx \sum_n^N \mu_n b_n(\mathbf{r}) . \quad (6.1)$$

We choose piecewise constant rect-functions as the basis functions, for to their symmetry relations and computational simplicity.

The imaging model for transmission tomography has the form given by Eq. (1.5). The approximate monoenergetic transmission continuous-to-discrete transformation can be written [4] as

$$\bar{g}_m = b_m \exp - \int_{\Gamma_m} \mu(\mathbf{r}) dl \quad (6.2)$$

where b_m is the blank scan of m^{th} detector bin and we define Γ_m as the polyhedron formed by the m^{th} detector bin as the base and the focal point as the apex.

Inserting the expansion into Eq. (6.2) leads to

$$\bar{g}_m = b_m \exp \left(- \sum_n^N \mu_n a_{mn} \right), \quad (6.3)$$

where the system matrix is defined as

$$a_{mn} = \int_{\Gamma_m} b_n(\mathbf{r}) dl. \quad (6.4)$$

Different system models have been studied by various groups. Considerations include detector characteristics, scan geometry, interactions between x-rays and matter, and the manner in which each voxel contributes to a given detector element. Improvements to the system model can lead to improved reconstructed image quality in terms of accuracy, spatial resolution, contrast, and detectability to name a few. Here is an overview of current system models:

- *Line based system models:* This model defines a system matrix element a_{mn} as the length-of-intersection of the projection ray associated with the m^{th} bin with n^{th} voxel. The ray is projected from the source to the center of a subdivision of the detector element. In the

context of circular orbit cone-beam geometry, this method creates ring artifacts in noncentral slices along the transaxial direction due to unequal weighting [57].

- *Trilinear interpolation* [1,57,58]: As with line-based system models, this one is also ray-driven. A projection ray is sampled at equidistant points and each sample point is interpolated to the eight nearest voxel centers. This method is relatively fast and widely used and has been shown to be a good approximation [59].
- *Exact volumetric intersection model*: A volumetric-intersection model interprets a projection ray as convex polyhedron with source at apex and detector bin at the base [31]. An exact volumetric system model determines the exact volume from intersection vertices. This is accomplished by locating the vertices where the projection ray intersects the voxel. From these vertices, the surfaces are subdivided into triangles and the volumes of the resulting tetrahedrons are computed. These volumes are then summed to form the intersected volume.
- *Discrete volume intersection model*: Discrete volumetric models are an approximation to exact volumetric models. This type of model subdivides the voxel into subvoxels and defines the approximation as the ratio of subvoxel centers to the total number of subvoxels [32,33].
- *Slab volume system model*: This is our proposed method. We interpret integration over slabs within Γ_m and parallel to the detector face. It consists of partitioning the reconstruction space into slabs that contain the demagnified detector bin grid and are oriented parallel to the detector. Section 6.3.4 gives a detailed description.

6.3.3 Reconstruction Method

Although any reconstruction algorithm that uses a projection operator would suffice, we chose to use the maximum likelihood-gradient ascent for transmission tomography (ML-

TRANS) algorithm [60] to demonstrate performance. This is a gradient ascent approach for maximization the log-likelihood function (Eq. (1.20)) for transmission data with Poisson noise.

The update formula can be written as

$$\mu_n^{k+1} = \mu_n^k + \frac{\sum_m^M \bar{g}_m^k - g_m a_{mn}}{\sum_m^M \bar{g}_m^k a_{mn} \sum_p^N a_{mp}} \quad (6.5)$$

where g_m is the raw projection data associated with the m^{th} detector bin. The simulated projection of the m^{th} detector bin for k^{th} iteration is

$$\bar{g}_m^k = b_m \exp\left(-\sum_n^N a_{mn} \mu_n^k\right) \quad (6.6)$$

where b_m is the blank scan of m^{th} detector bin.

6.3.4 Slab Formulism of System Matrix

The method consists of partitioning the reconstruction space into slabs. The slabs are oriented parallel to the detector face. Each slab is partitioned into a grid composed of a demagnified version of the detector bin grid. The grid size for slab s that is located a distance d_s from the detector face is

$$\delta_s = P \left(\frac{F - d_s}{F} \right) \quad (6.7)$$

where P is the detector grid size and F is the focal length. A slab bin corresponding to slab s and the m^{th} detector bin is denoted sm . For each slab, the area-of-intersection between a system matrix element a_{sm} is the sum of the individual slab contributions and is given by

$$a_{mi} = \sum_s^S a_{smi} \quad (6.8)$$

where S is the total number of slabs. An example of a slab that is located a distance d from the detector is shown in Fig. 6.2a. An individual slab contribution is

$$a_{smi} = \left(\frac{t}{\cos \phi_m} \right) \left(\frac{x_{smi} y_{smi}}{\delta_s \delta_s} \right) \quad (6.9)$$

where x_{smi} and y_{smi} are the width and height, respectively, of the area-of-intersection between sm^{th} slab-bin and n^{th} voxel. The factor ϕ_m is the angle between the cone-beam iso-ray and a ray from the focal point to the center of the m^{th} detector bin. The slab thickness is t . Illustrations of a voxel-slab-intersection are shown in Fig. 6.2b,c.

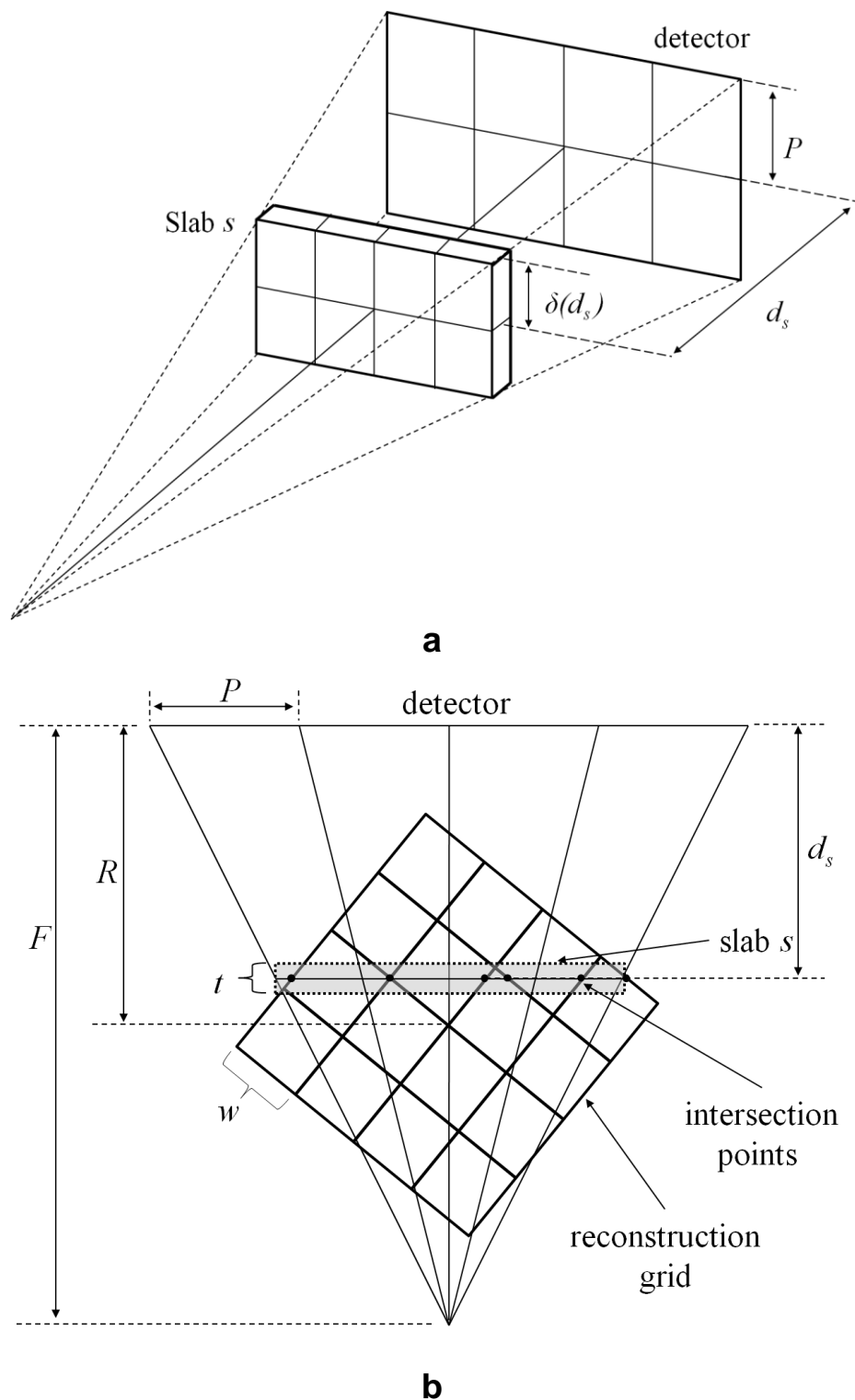


Figure 6.2. Geometry of cone-beam CT. (a) Slab with a grid size δ that is equal to the de-magnified detector bin grid size P at a distance d from the detector face to the center of the slab. (b) View of a voxel-slab-intersection along the transaxial direction. The intersection points between the center of the slab and the voxel grid are shown.

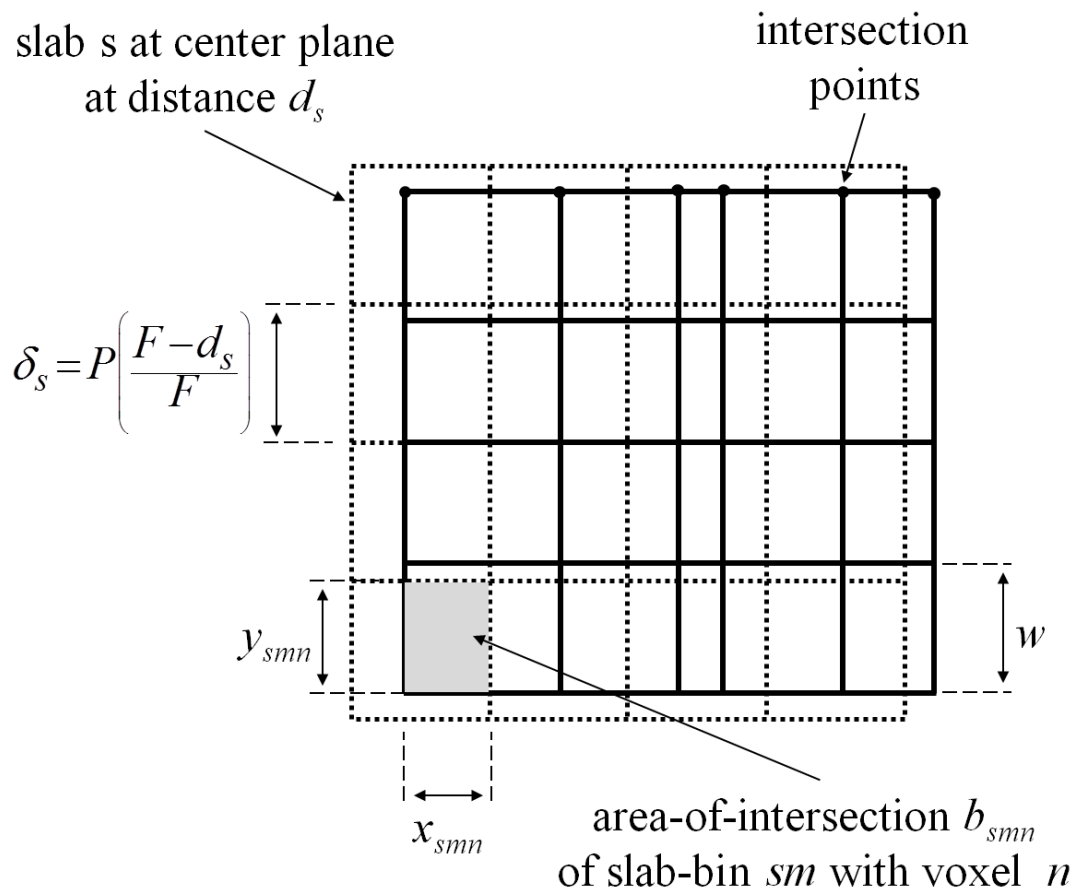


Figure 6.3. Detector plane view of the voxel-slab-intersection. The shaded region shows the area-of-intersection between a slab-bin and a voxel.

6.4 Results

The following figures show reconstructions of a dead mouse imaged using the MicroCAT II at Upstate Medical University. For comparison, we also included reconstructions done using the commercial FBP-based software, Cobra (Exxim Computing Corporation), without the application of post smoothing. A slice through the transaxial plane displaying the sinus is shown in Fig. 6.4 and a slice through the coronal plane is shown in Fig. 6.5.

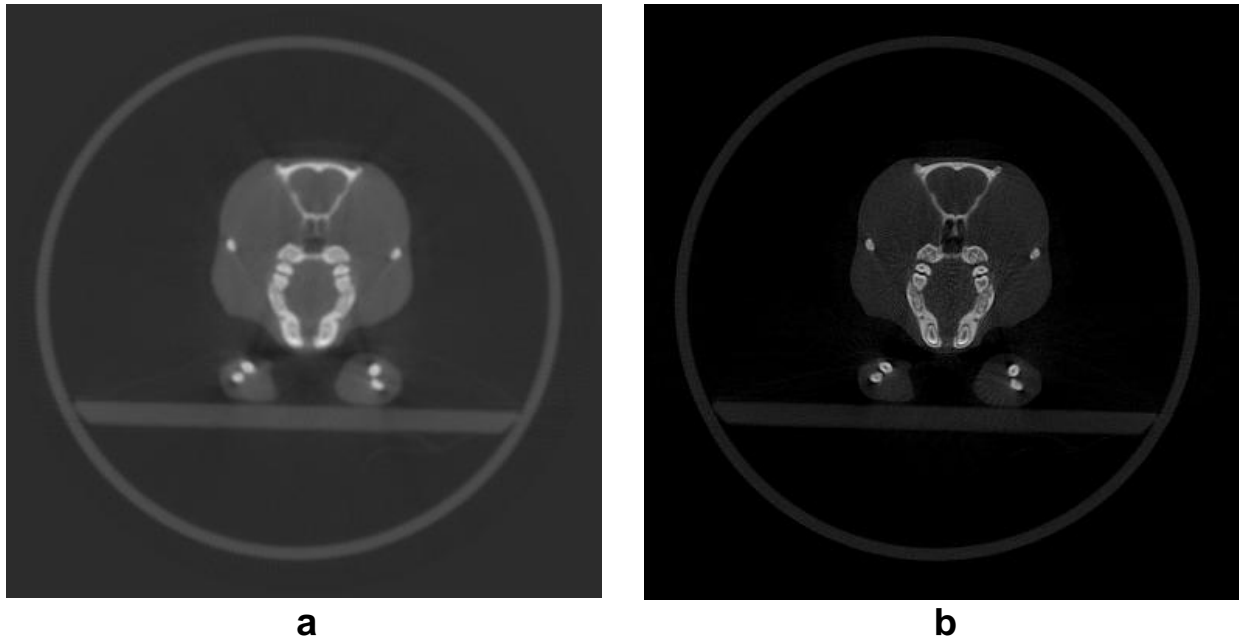


Figure 6.4. Reconstructions of micro CT data set consisting of projections of the head of a rat. (a) reconstruction using commercial FBP-based software, Cobra (Exxim Computing Corporation), without any post smoothing applied. (b) Iterative reconstruction using slab formulism.

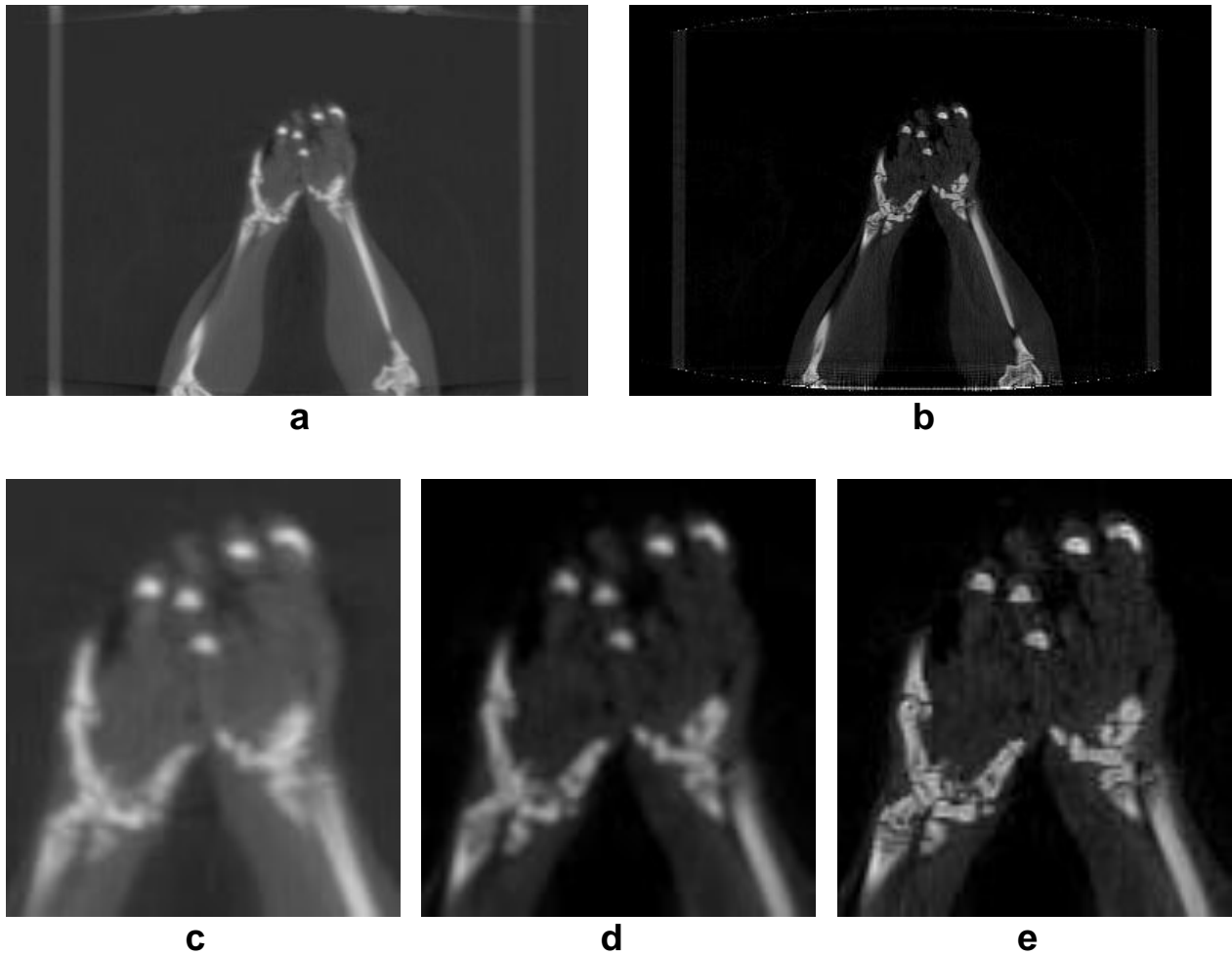


Figure 6.5. Coronal view of the paws. (a) Reconstructed using FBP. (b) Iterative reconstruction using slab formulism. (c) Close-up of (a). (d) and (e) Close-ups of (b). (d) Result after applying a post 3×3 neighborhood averaging filter to (b).

6.5 Conclusions

Our contribution to micro-CT reconstruction is the formulation and implementation of a cone-beam system matrix that reduces ring artifacts associated with sampling of the reconstruction space. This new approach reduces the common 3-D ray-tracing technique into 2-D, making it very efficient. The images obtained using our approach were compared to images reconstructed by means of analytical techniques. We observed significant improvement in the image quality for the images reconstructed using our iterative method. Though initial results are

promising, further work is required. Beam hardening artifacts are clearly visible and methods for their reduction should be developed and applied. Computational speed is slow. Quantitative analysis will need to be conducted to determine accuracy.

Appendix

A.1 Detector and Collimator Parameters

Table A.1 shows the detector and collimator parameters of the imaging systems used in the Division of Nuclear Medicine at SUNY Upstate Medical University. Table A.2 shows the detector parameters of the simulated datasets used in this dissertation. These datasets were created using the SIMIND Monte Carlo simulation software [25].

Table A.1. Parameters of detectors and collimators used in the Division of Nuclear Medicine at SUNY Upstate Medical University.

	Siemens LEHR parallel- beam	Siemens LEHR cone-beam	Trionix LEUR parallel-beam	Trionix LEHR fan-beam	Trionix cone-beam
Detector width (pixels)	128	128	128	128	128
Detector height (pixels)	128	128	64	64	64
pixel size (cm)	0.4795	0.4795	0.362	0.356	0.362
Collimator thickness (cm)	2.405	2.8	3.4925	4.13	4.3
Septal wall thickness (cm)	0.016	0.025	0.01778	0.015	0.025
Hole diameter (cm)	0.111	0.19	0.1397	0.12	0.19
Focal length (cm)	NA	70	NA	43.1	100

Table A.2. Parameters of the simulated gamma ray detection systems used for this study.

	LEUR parallel-beam	LEUR fan-beam	LEUR cone-beam
Detector width (pixels)	128	128	128
Detector height (pixels)	64	64	64
Pixel size (cm)	0.362	0.356	0.356
Collimator thickness (cm)	3.49	4.13	4.13
Septal wall thickness (cm)	0.0178	0.015	0.015
Hole diameter (cm)	0.14	0.12	0.12
Focal length (cm)	NA	43.1	43.1

A.2 Resolution and Sensitivity Parameters for Simulated Parallel-Beam

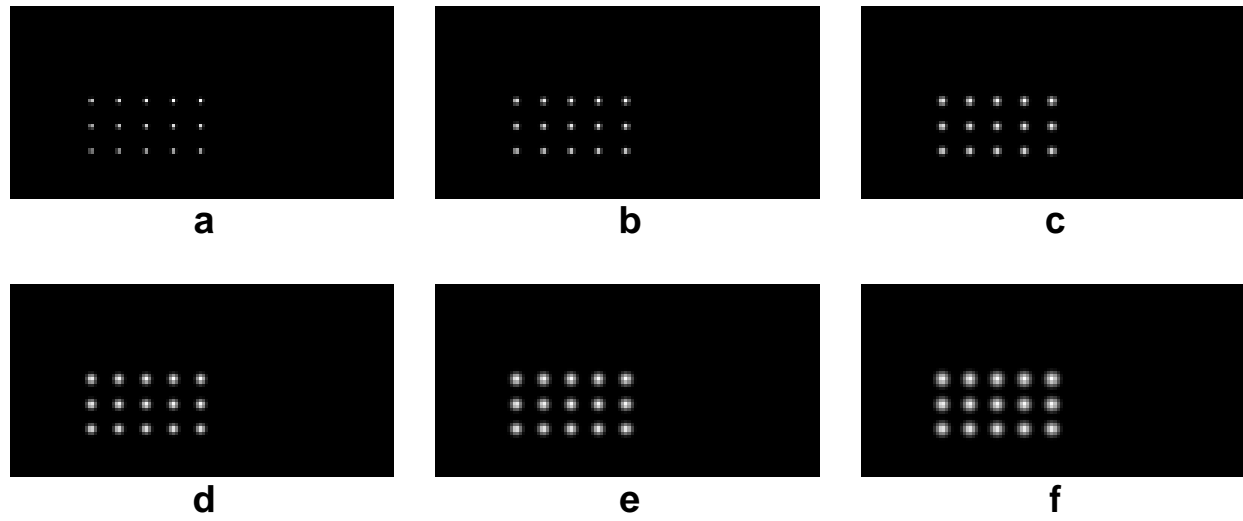


Figure A.1. SIMIND simulation of point sources imaged with parallel-beam collimator. Distance of point source from collimator face; (a) 4.4 cm, (b) 8.8 cm, (c) 13.2 cm, (d) 17.6 cm, (e) 22.0 cm, and (f) 26.4 cm.

Table A.3. Parameters when line-profiles through the parallel-beam collimator projected point-sources shown in fig. 8.1 are fit to an amplitude-Gaussian function Eq. (1.15).

distance to collimator (cm)	w (pixels)	w std error (pixels)	FWHM (pixels)	A (counts/MBq)	A std error (counts/MBq)	R^2
0.00	3.22×10^{-1}	7.71×10^{-4}	7.59×10^{-1}	7.27×10^{-1}	5.71×10^{-2}	1
4.40	4.70×10^{-1}	2.75×10^{-4}	1.11	5.14×10^{-1}	1.89×10^{-2}	1
8.80	6.52×10^{-1}	3.37×10^{-3}	1.53	2.96×10^{-1}	1.39×10^{-1}	0.99983
1.32×10^{-1}	8.33×10^{-1}	1.25×10^{-2}	1.96	1.85×10^{-1}	2.33×10^{-1}	0.99884
1.76×10^{-1}	1.01	8.36×10^{-3}	2.38	1.24×10^{-1}	7.94×10^{-2}	0.99969
2.20×10^{-1}	1.22	3.12×10^{-2}	2.86	8.87	1.65×10^{-1}	0.99726
2.64×10^{-1}	1.40	3.16×10^{-2}	3.31	6.61	1.10×10^{-1}	0.99728

Table A.4. Coefficients for the Gaussian spread w (Eq. (1.17)) of the resolution function for parallel-beam collimator.

coefficient	value	std error
b_0	2.98×10^{-1}	1.17×10^{-2}
b_1	4.14×10^{-2}	7.34×10^{-4}
b_2	0	0
b_3	0	0

Table A.5. Coefficients for the amplitude A (Eq. (1.16)) of the resolution function for parallel-beam collimator.

coefficient	value	std error
a_0	7.35×10^{-1}	1.81
a_1	-6.43	6.51×10^{-1}
a_2	2.03×10^{-1}	6.05×10^{-2}
a_3	-2.08×10^{-3}	1.50×10^{-3}

A.3 Resolution and Sensitivity Parameters for Simulated Fan-Beam SPECT

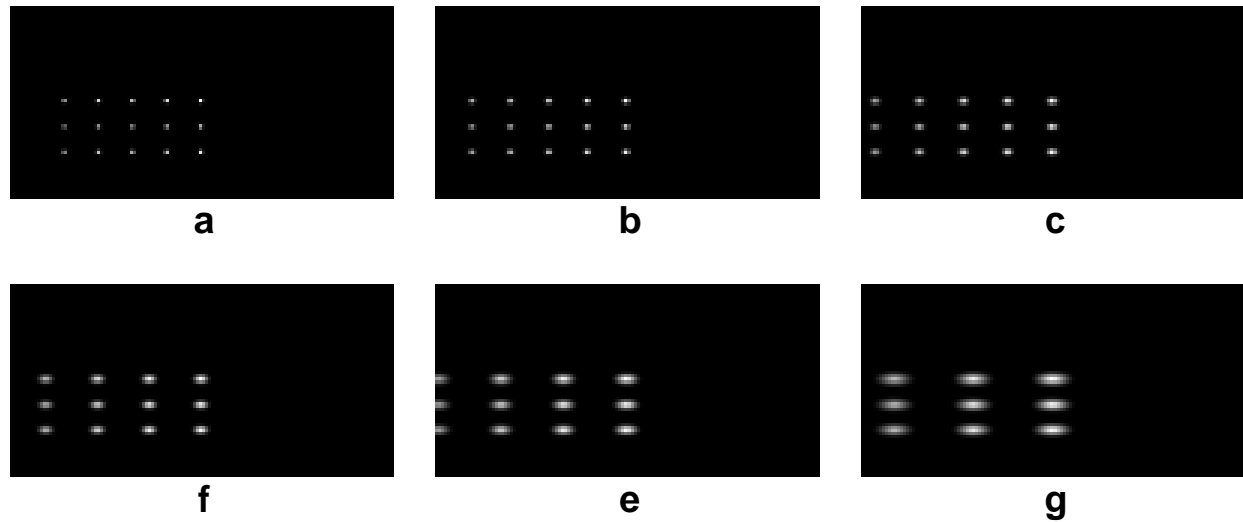


Figure A.2. SIMIND simulation of point sources imaged with fan-beam collimator. Distance of point source from collimator face; (a) 4.4 cm, (b) 8.8 cm, (c) 13.2 cm, (d) 17.6 cm, (e) 22.0 cm, and (f) 26.4 cm.

Table A.6. Parameters when line-profiles through the fan-beam collimator projected point-sources shown in fig. 8.2 are fit to an amplitude-Gaussian function Eq. (1.15).

distance to collimator (cm)	w (pixels)	w std error (pixels)	FWHM (pixels)	A (counts/MBq)	A std error (counts/MBq)	R^2
0.00	3.19×10^{-1}	5.96×10^{-4}	7.51×10^{-1}	6.82×10^{-1}	3.49×10^{-4}	1
4.40	3.99×10^{-1}	3.54×10^{-4}	9.40×10^{-1}	5.91×10^{-1}	3.23×10^{-4}	1
8.80	5.36×10^{-1}	1.16×10^{-4}	1.26	4.67×10^{-1}	8.11×10^{-5}	1
1.32×10^{-1}	6.69×10^{-1}	3.03×10^{-3}	1.58	3.01×10^{-1}	1.25×10^{-3}	0.9998
1.76×10^{-1}	8.02×10^{-1}	7.63×10^{-3}	1.89	2.65×10^{-1}	2.22×10^{-3}	0.99918
2.20×10^{-1}	9.24×10^{-1}	4.90×10^{-3}	2.18	2.20×10^{-1}	9.78×10^{-4}	0.99977
2.64×10^{-1}	1.06	1.10×10^{-2}	2.48	2.49×10^{-1}	2.13×10^{-3}	0.99915

Table A.7. Coefficients for the Gaussian spread functions along the horizontal w_u and vertical w_v (Eq. (1.17)) of the resolution function for fan-beam collimator.

w_u			w_v		
coefficient	value	std error	coefficient	value	std error
b_0	1.65×10^{-1}	6.21×10^{-2}	b_0	2.71×10^{-1}	3.97×10^{-3}
b_1	7.44×10^{-2}	1.61×10^{-2}	b_1	2.99×10^{-2}	2.32×10^{-4}
b_2	-3.09×10^{-3}	1.17×10^{-3}	b_2	0	0
b_3	1.62×10^{-4}	2.51×10^{-5}	b_3	0	0

Table A.8. Coefficients for the amplitude A (Eq. (1.16)) of the resolution function for fan-beam collimator.

coefficient	value	std error
a_0	9.75×10^{-1}	6.66×10^{-3}
a_1	-7.20×10^{-2}	1.72×10^{-3}
a_2	2.45×10^{-3}	1.25×10^{-5}
a_3	-2.82×10^{-5}	2.69×10^{-6}

A.4 Resolution and Sensitivity Parameters for Simulated Cone-Beam

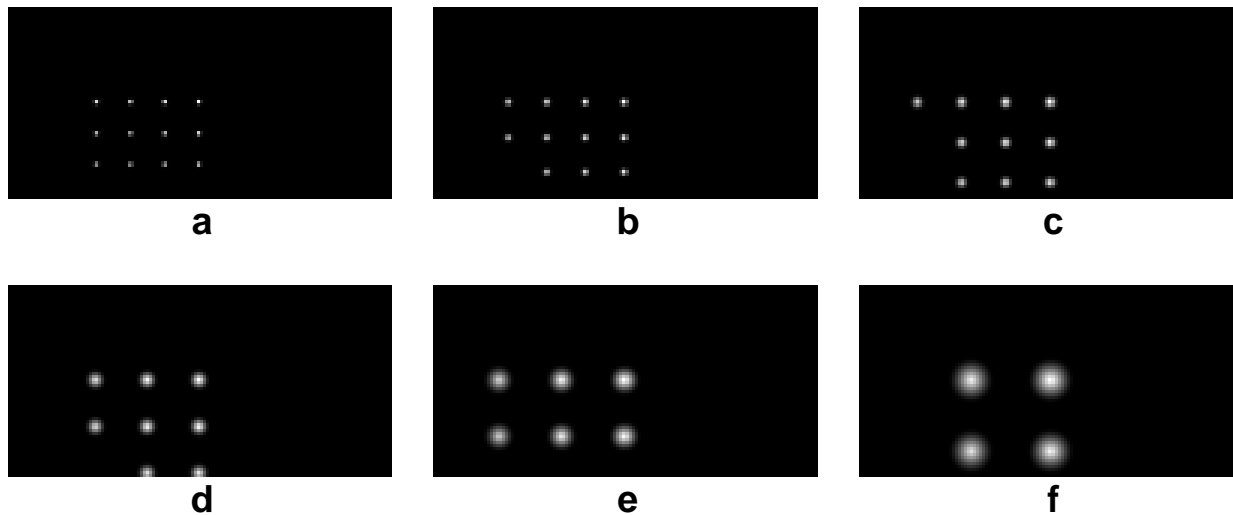


Figure A.3. SIMIND simulation of point sources imaged with cone-beam collimator. Distance of point source from collimator face; (a) 4.4 cm, (b) 8.8 cm, (c) 13.2 cm, (d) 17.6 cm, (e) 22.0 cm, and (f) 26.4 cm.

Table A.9. Parameters when line-profiles through the cone-beam collimator projected point-sources shown in fig. 8.3 are fit to an amplitude-Gaussian function Eq. (1.15).

distance to collimator (cm)	w (pixels)	w std error (pixels)	FWHM (pixels)	A (counts/MBq)	A std error (counts/MBq)	R^2
0.00	3.22×10^{-1}	5.12×10^{-4}	7.59×10^{-1}	7.73×10^{-1}	4.43×10^{-4}	1
4.40	4.59×10^{-1}	2.13×10^{-4}	1.08	7.77×10^{-1}	2.39×10^{-4}	1
8.80	6.87×10^{-1}	3.42×10^{-3}	1.62	5.58×10^{-1}	2.52×10^{-3}	0.99969
1.32×10^{-1}	9.71×10^{-1}	5.24×10^{-3}	2.29	4.19×10^{-1}	1.90×10^{-3}	0.99971
1.76×10^{-1}	1.39	1.80×10^{-2}	3.27	3.36×10^{-1}	3.55×10^{-3}	0.99832
2.20×10^{-1}	1.99	3.27×10^{-2}	4.69	2.93×10^{-1}	3.73×10^{-3}	0.99729
2.64×10^{-1}	1.99	3.27×10^{-2}	4.69	2.93×10^{-1}	3.73×10^{-3}	0.99729

Table A.10. Coefficients for the Gaussian spread w (Eq. (1.17)) of the resolution function for cone-beam collimator.

coefficient	value	std error
b_0	3.13×10^{-1}	2.11×10^{-2}
b_1	4.01×10^{-2}	7.57×10^{-3}
b_2	-8.54×10^{-4}	7.03×10^{-3}
b_3	1.15×10^{-4}	1.75×10^{-5}

Table A.11. Coefficients for the amplitude A (Eq. (1.16)) of the resolution function for cone-beam collimator.

coefficient	value	std error
a_0	1.01×10^{-6}	2.42×10^{-8}
a_1	-6.17×10^{-8}	3.59×10^{-9}
a_2	1.29×10^{-9}	1.14×10^{-10}
a_3	0	0

Bibliography

- [1] C. Kak and M. Slaney, *Principles of Computerized Tomographic Imaging*. New York, New York: IEEE Press, 1987.
- [2] M. N. Wernick and J. N. Aarsvold, *Emission Tomography: The Fundamentals of PET and SPECT*. San Diego: Elsevier Academic Press, 2004.
- [3] Y. Censor, "Finite series-expansion reconstruction methods," in *Proc. IEEE*, 1983, pp. 409-19.
- [4] J. A. Fessler. (2008) [Online]. <http://www.eecs.umich.edu/~fessler/papers/talks.html>
- [5] R. M. Lewitt, "Alternatives to voxels for image representation in iterative reconstruction algorithms," *Phys. Med. Biol.*, vol. 37, pp. 705-16, 1992.
- [6] B. Wolbarst, *Physics of Radiology*. Madison, Wisconsin: Medical Physics Publishing, 2000.
- [7] J. H. Hubbell and S. M. Seltzer, Ionizing Radiation Division, Physics Laboratory, NIST.
- [8] S. R. Cherry, J. A. Sorenson, and M. E. Phelps, *Physics in nuclear medicine*, 3rd ed. Philadelphia, PA: Elsevier Science, 2003.
- [9] P. Khurd, "On Reconstruction Methods and Image Quality in Emission Tomography," SUNY Stony Brook University, Stony Brook, Ph.D. thesis 2005.
- [10] R. Noumeir, G. E. Mailloux, and R. Lemieux, "Three-dimensional correction of experimentally determined gamma camera response," in *1994 IEEE Conference Record, Nuclear Science Symposium and Medical Imaging Conference*, vol. 4, 1995, pp. 1720-4.
- [11] B. M. W. Tsui and G. T. Gullberg, "The geometric transfer function for cone and fan beam collimators," *Phys. Med. Biol.*, vol. 35, pp. 81-93, 1990.
- [12] E. C. Frey, B. M. W. Tsui, and G. T. Gullberg, "Improved estimation of the detector response function for converging beam collimators," *Phys. Med. Biol.*, vol. 43, pp. 941-50, 1998.
- [13] C. E. Metz, F. B. Atkins, and R. N. Beck, "The geometric transfer function component for scintillation camera collimators with straight parallel holes," *Phys. Med. Biol.*, vol. 25, pp. 1059-70, 1980.
- [14] P. P. Bruyant, "Analytic and Iterative Reconstruction Algorithms in SPECT," *J. Nucl. Med.*, vol. 43, pp. 1343-58, 2002.
- [15] T. Hebert and R. Leahy, "A generalized EM algorithm for 3-D bayesian reconstruction form Poisson data using Gibbs priors," *IEEE Trans. Medical Imaging*, vol. 8, no. 2, pp. 194-202, 1989.

- [16] P. J. Green, "On use of the EM algorithm for penalized likelihood estimation," *Journal of the Royal Statistical Society. Series B (Methodological)*, vol. 52, no. 3, pp. 443-52, 1990.
- [17] L. A. Shepp and Y. Vardi, "Maximum likelihood reconstruction for emission tomography," *IEEE Trans. Med. Imagong*, vol. MI-1, pp. 113-22, 1982.
- [18] K. Lange and R. Carson, "EM reconstruction algorithms for emission and transmission tomography," *J. Comput. Assist. Tomogr.*, vol. 8, pp. 306-16, 1984.
- [19] H. Hudson and R. Larkin, "Accelerated image reconstruction using ordered subsets of projection data," *IEEE Trans. Nucl. Sci.*, vol. 13, pp. 601-09, 1994.
- [20] A. Krol et al., "Application of Ordered-Subsets Expectation-Maximization (OSEM) algorithm to cone-beam SPECT for accelerated 3D reconstruction," in *IEEE Nuclear Science Symp. and Medical Imaging Conf.*, vol. 6, 2004, pp. 3971-73.
- [21] J. Llacer, E. Veklerov, K. J. Coakley, E. J. Hoffman, and J. Nunez, "Statistical analysis of maximum likelihood estimator images of human brain FDG PET studies," *IEEE Trans. Med. Imaging*, vol. 12, pp. 215-32, 1993.
- [22] B. M. Silverman, M. C. Jones, J. D. Wilson, and D. W. Nychka, "A smoothed EM approach to indirect estimation problems, with particular reference to stereology and emission tomography," *J. Roy. Stat. Soc.*, vol. 52, pp. 271-324, 1990.
- [23] F. J. Beekman, E. T. P. Slijpen, and W. J. Niessen, "Selection of task-dependent diffusion filters for the post-processing of SPECT images," *Phys. Med. Biol.*, vol. 43, no. 1998, pp. 1713-30, 1998.
- [24] P. J. Green, "Bayesian reconstructions from emission tomography data using a modified EM algorithm," *IEEE Trans. Med. Imaging*, vol. 9, pp. 84-93, 1990.
- [25] M. Ljungberg and S. E. Strand, "Monte Carlo program for the simulation of scintillation camera characteristics," *Comput. Methods Programs Biomed.*, vol. 29, pp. 257-72, 1989.
- [26] A. R. De Pierro and M. E. B. Yamagishi, "Fast EM-like methods for maximum "a posteriori" estimates in emission tomography," *IEEE Trans. Med.*, vol. 20, pp. 280-8, 2001.
- [27] A. Yendiki and J. A. Fessler, "Analysis of observer performance in known-location tasks for tomographic image reconstruction," *IEEE Trans. Med. Imaging*, vol. 2006, pp. 28-41, 2006.
- [28] E. C. Frey, B. M. Tsui, and M. Ljungberg, "A comparison of scatter compensation methods in SPECT: subtraction-based techniques versus iterative reconstruction with accurate modeling of the scatter response," *1992 IEEE Nuclear Science Symp. and Medical Imaging Conf.*, pp. 1035-8, 1992.

- [29] Y. K. Dewaraja, M. Ljungberg, and J. A. Fessler, "3-D Monte Carlo-based scatter compensation in quantitative I-131 SPECT reconstruction," *IEEE Trans. Nucl. Sci.*, vol. 53, pp. 181-8, 2006.
- [30] S. B. Lo, "Strip and line path integrals with a square pixel matrix: A unified theory for computational CT projections," *IEEE Trans. Med. Imaging*, vol. 7, pp. 355-63, 1988.
- [31] J. Scheins, F. Boschen, and H. Herzog, "Analytical calculation of volumes-of-intersection for iterative 3-D PET reconstruction," *IEEE Trans. on Med. Imaging*, vol. 25, no. 10, pp. 1363-1369, 2006.
- [32] J. Gregor et al., "Approximate volumetric system models for microSPECT," *IEEE Trans. Nucl. Sci.*, vol. 53, pp. 2646-52, 2006.
- [33] H. Ye, "Development and implementation of fully 3D iterative reconstruction approaches in SPECT with parallel-, fan-, and cone-beam collimators," Syracuse University, Dissertation 2008.
- [34] H. Ye, A. Krol, D. H. Feiglin, and E. D. Lipson, "Implementation of strip-area system model for fan-beam collimator SPECT reconstruction," in *Proc. SPIE 6142, Medical Imaging 2006*, 2006, p. 40.
- [35] Y. Hongwei, "Development and implementation of fully 3d iterative reconstruction approaches in SPECT with parallel-, fan-, and cone-beam collimator, 2008, Dissertation.
- [36] R. L. Siddon, "Fast calculations of the exact radiological path for a three-dimensional CT array," *Med. Phys.*, vol. 12, pp. 252-5, 1985.
- [37] G. Han, Z. Liang, and J. You, "A fast ray-tracing technique for TCT and ECT studies," in *IEEE Nucl. Sci. Conf. Rec.*, 1999, pp. M10-75.
- [38] Z. Liang, J. Cheng, and J. Ye, "Validation of the central-ray approximation for attenuated depth-dependent convolution in quantitative SPECT reconstruction," *Phys. Med. Biol.*, vol. 42, pp. 433-439, 1997.
- [39] R. J. Jaszczak, L. T. Chang, N. A. Stein, and F. E. Moore, "Whole-body single-photon emission computed tomography using dual, large field-of-view scintillation cameras," *Phys Med Biol*, vol. 24, pp. 1123-43, 1979.
- [40] A. Krol et al., "An EM algorithm for estimating SPECT emission and transmission parameters from emission data only," *IEEE Trans Med Imaging*, vol. 20, pp. 218-32, 2001.
- [41] R. J. Jaszczak, C. E. Floyd, S. H. Manglos, K. L. Greer, and R. E. Coleman, "Cone beam collimation for single photon emission computed tomography: Analysis, simulation and image reconstruction using filtered backprojection," *Med Phys*, vol. 13, no. 4, pp. 484-489, 1986.

- [42] J. Li et al., "An evaluation of lesion detectability with cone-beam, fanbeam and parallel-beam collimation in SPECT by continuous ROC study," *The Journal of Nuclear Medicine*, vol. 35, no. 1, pp. 135-40, 1993.
- [43] B. D. Smith, "Image reconstruction from cone-beam projections: necessary and sufficient conditions and reconstruction methods," *IEEE Trans. Med. Imaging*, vol. MI-4, pp. 14-25, 1985.
- [44] H. K. Tuy, "An inversion formula for cone-beam reconstruction," *SIAM J. Appl. Math.*, vol. 43, pp. 546-52, 1983.
- [45] B. D. Smith, "Cone-beam tomography: recent advances and a tutorial review," *Opt. Eng.*, vol. 29, pp. 524-34, 1990.
- [46] M. V. Narayanan, M. A. King, and C. L. Byrne, "Combined fan/parallel beam reconstruction in cardiac SPECT imaging," in *Conference Record. 1999 Nuclear Science Symp. and Medical Imaging Conf.*, vol. 3, 1999, pp. 1142-46.
- [47] R. J. Jaszczak, J. Li, J. Wang, and R. E. Coleman, "Three dimension SPECT reconstruction of combined cone beam and parallel beam data," *Phys Med Biol*, vol. 37, pp. 535-548, 1992.
- [48] J. Li, R. J. Jaszczak, T. G. Turkington, K. L. Greer, and R. E. Coleman, "SPECT reconstruction of combined cone beam and parallel hole collimation with experimental data," *IEEE Trans Nucl Sci*, vol. 40, pp. 300-306, 1993.
- [49] S. Matej et al., "Evaluation of task-oriented performance of several fully 3D PET reconstruction algorithms," *Phys. Med. Biol.*, vol. 39, no. 3, pp. 355-67, Mar 1994.
- [50] J. G. Brankov, Y. Yang, and M. N. Wernick, "Tomographic image reconstruction based on a content adaptive mesh model," *IEEE Trans. Med. Imaging*, vol. 12, pp. 202-12, 2004.
- [51] A. Sitek, R. H. Huesman, and G. T. Gullberg, "Tomographic reconstruction using an adaptive tetrahedral mesh defined by a point cloud," *IEEE Trans. Med. Imaging*, vol. 25, pp. 1172-79, 2006.
- [52] J. G. Brankov, Y. Yang, and M. N. Wernick, "Content-adaptive 3D mesh modeling for representation of volumetric images," in *IEEE Intl. Conf. on Image Processing*, 2002, pp. 849-52.
- [53] D. Engwirda. (2009, Oct) MESH2D - Automatic Mesh Generation. [Online].
<http://www.mathworks.com/matlabcentral/fileexchange/25555-mesh2d-automatic-mesh-generation>
- [54] W. P. Segars, "Development of a new dynamic NURBS-based cardiac-torso (NCAT) phantom," The University of North Carolina, Ph.D. thesis 2001.
- [55] R. G. Delgado and J. G. Brankov, "Mesh model based projection operator for emission tomography," in *IEEE Nuclear Science Symposium Conference Record*, 2007, pp. 2760-3.

- [56] H. H. Barrett and K. J. Myers, *Foundations of Image Science*. New York, New York: Wiley, 2003.
- [57] G. L. Zeng and G. T. Gullberg, "A study of reconstruction artifacts in cone beam tomography using filtered backprojection and iterative EM algorithms," *IEEE Trans. Nucl. Sci.*, vol. 37, no. 2, pp. 759-67, 1990.
- [58] G. Wang, M. W. Vannier, and P-C Cheng, "Iterative X-ray Cone-Beam Tomography for Metal Artifact Reduction and Local Region Reconstruction," *Microscopy and Microanalysis*, vol. 5, pp. 58-65, 1999.
- [59] T. M. Benson and J. Gregor, "Framework for iterative cone-beam micro-CT reconstruction," *IEEE Trans. Nucl. Sci.*, vol. 52, no. 5, pp. 1335-40, 2005.
- [60] J. Nuyts et al., "Iterative reconstruction for helical CT: a simulation study," *Phys. Med. Biol.*, vol. 43, no. 4, pp. 729-37, 1998.

VITA

NAME OF AUTHOR: Levon Vogelsang

PLACE OF BIRTH: Palm Springs, California

DATE OF BIRTH: September 26, 1975

GRADUATE AND UNDERGRADUATE SCHOOL ATTENDED:

Syracuse University, Syracuse, New York

DEGREES AWARDED:

Masters of Science in Physics, 2007

Bachelor of Science in Physics, 2005

AWARDS AND HONORS:

Henry Levinstein Fellowship, 2008, 2009

Future Educators Scholarship, 2008

Sigma Pi Sigma, 2005

Chancellor's Scholarship, 2004, 2005

PROFESSIONAL EXPERIENCE:

Imaging Scientist, Virtualscopics, 2010-Present

Assistant Coordinator, In Vivo micro CT Project, 2006-2010

Research and Teaching Assistant, Syracuse University, 2005-2010